POLYELECTROLYTE MULTILAYER TEMPLATE ASSISTED IN-SITU SYNTHESIS OF INORGANIC NANOSTRUCTURES

Doctoral Dissertation
Jožef Stefan International Postgraduate School
Ljubljana, Slovenia, July,2009

Supervisor: *Prof. Dr. Danilo Suvorov*

Co-supervisor: *Assis. Prof. Dr. Boštjan Jančar*

Evaluation Board:

Prof. Dr. Paolo Nanni, Inst. Energetics & Interphases, C.N.R., via De Marini 6, I-16149 Genoa, Italy

Assis. Prof. Dr. Miran Čeh, Nanostructured Materials Department, Jozef Stefan Institute, Jamova 39, 1000 Ljubljana

Assis. Prof. Dr. Aleksander Rečnik, Nanostructured Materials Department, Jozef Stefan Institute, Jamova 39, 1000 Ljubljana

Manca Logar

POLYELECTROLYTE MULTILAYER TEMPLATE ASSISTED IN-SITU SYNTHESIS OF INORGANIC NANOSTRUCTURES

Doctoral Dissertation

IN-SITU SINTEZA ANORGANSKIH NANOSTRUKTUR V VEČPLASTNI POLIELEKTROLITNI MATRICI

Doktorska disertacija

Supervisor: Prof. Dr. Danilo Suvorov

Co-Supervisor: Assist. Prof. Dr. Boštjan Jančar

July 2009

MEDNARODNA PODIPLOMSKA ŠOLA JOŽEFA STEFANA
JOŽEF STEFAN INTERNATIONAL POSTGRADUATE SCHOOL
Ljubljana, Slovenia

Table of contents

Abbreviations

SPR	=	Surface plasmon resonance
LSPR	=	Localized surface plasmon resonance
DDA	=	Discrete dipole approximation
SAMs	=	Self assembled monolayer
LB	=	Langmuir-Blodget
LbL	=	Layer by Layer
PE	=	Polyelectrolyte
PEM	=	Polyelectrolyte multilayer
PAH	=	Poly(allylamine)hydrochloride
PDADMAC	=	Poly(diallyldimethylammonium) chloride
PEI	=	Poly(ethylenimine)
PSS	=	Poly(sodium 4-styrenesulfanate)
PAA	=	Polyacrylic acid
STEM-HAADF	=	Scanning transmission electron microscopy - high angle annular dark field
HRTEM	=	high resolution transmission microscopy
STEM-BF	=	Scanning transmission electron microscopy - bright field
AFM	=	Atomic force microscopy
UV-vis	=	Ultaviolet - visible

Abstract

Thin film nanocomposites consisting of inorganic matter embedded within a soft polymeric matrix on the nanometer scale have attracted much interest lately due to their unique properties with potential application in optoelectronics and photonics.
Polyelectrolyte multilayers formed by the layer-by-layer electrostatic assembly of oppositively charged polyions can be utilized as nanoreactors for the in-situ nanoparticle synthesis, where the surrounding polymer prevents their aggregation and thus enables a control over the inorganic-organic composite properties.
Multilayers formed from weak polyions of polyallylamine (PAH) and polyacrylic acid (PAA), possessing ion-exchangeable carboxylic groups were used to bind metal cations within the film. By subsequent wet chemical reaction process of the incorporated metal ions, pure zinc sulfide (ZnS), manganese doped zinc sulfide and silver (Ag) nanoparticles with a narrow size distribution were formed within the PEMs. The size and concentration of the inorganic nanoparticles in polyion matrix were controlled by the concentration of metal – binding carboxylic acid groups as determined by the multilayer assembly pH. Furthermore, the metal cation loading and reaction methodology could be repeatedly cycled to increase the size and volume density of the nanoparticles.
Furthermore, the polyelectrolyte multilayer films were used as templates for the ceramic (TiO_2) thin film fabrication with a modified sol-gel reaction. Since the multilayer assembly is performed from polyion aqous solutions, the multilayers contain some water that after infiltration of the organometallic precursor enables in-situ reaction of hydrolysis and condensation. After calcination, nanocrystalline TiO_2 thin films with thickness controllable by the number of the polyion layers in the matrix were formed.
With the in-situ synthesis approach of inorganic nanstructures in polyelectrolyte multilayer matrix, the ability of obtaining the control over the film thickness and size of the inorganic particles enabled tuning of the optical properties of as fabricated inorganic-organic composite films as well as nanocrystalline ceramic films.

Povzetek

Raziskave na področju priprave nano-kompozitnih tankih plasti organske komponente v polimerni matrici so v zadnjem času pritegnile veliko pozornosti zaradi posebnih lastnosti nanostrukturnih kompozitov in možnosti aplikacije le-teh na področju optoelektronike in fotonike. Večplastna polielektrolitna matrica pripravljena z metodo « Layer-by-Layer self assembly« lahko deluje kot nanoreaktor za in-situ sintezo anorganskih nanodelcev pri čemer organska matrica omogoča sterično stabilizacijo nanodelcev, ki preprečuje njihovo aglomeracijo in s tem omogoča kontrolo lastnosti tako pripravljenih kompozitnih plasti.

Organsko matrico v obliki večplastnega polielektrolitnega nanosa na substratu smo pripravili izmeničnim nanašanjem šibkega poli-kationa polialilamina (PAH) in poli-aniona poliakrilne kisline (PAA) na osnovi elektrostatskega privlaka. Pri nanašanju polielektrolitnih plasti iz raztopin v določenem pH-območju so v večplastni matrici prisotne nedisocirane funkcionalne skupine. Le-te delujejo kot vezna mesta za kovinske ione, ki se z reakcijo redukcije ali sulfidikacije pretvorijo v kovinske npr. Ag, polprevodne npr. ZnS ali dopirane polprevodne npr. (Mn-ZnS) nanodelce. S spreminjanjem pH-vrednosti polielektrolitnih raztopin smo kontrolirali delež nedisociranih skupin ter molekulsko organizacijo polielektrolitnih verig v večplastni matrici, kar vpliva na velikost in koncentracijo nanodelcev v polielektrolitni matrici. Velikost in volumski delež delcev v matrici lahko povečamo s ponavljanjem reakcijskega procesa.

Polielektrolitne nanose smo uporabili za pripravo keramičnih (TiO_2) tankih plasti z modificirano sol-gel reakcijo. Glede na to, da priprava večplastne matrice poteka iz vodnih raztopin polielektrolitov, večplastni polielektrolitni nanos vsebuje vodo, ki pri infiltraciji organokovinskega prekurzorja omogoča in-situ reakciji hidrolize in kondenzacije. Sledi termična obdelava, ki omogoča nastanek nanokristaliničnih (TiO_2) tankih plasti, katerih debelino lahko natančno kontroliramo s številom polielektrolitnih plasti organske matrice.

Pri in-situ sintezi anorganskih nanostruktur v večplastni polielektrolitni matrici, kontrolirana debelina tankih plasti in velikosti delcev omogočata vpliv na optične lastnosti anorgansko-organskih kompozitnih kot tudi nanokristaliničnih keramičnih tankih plasti.

1 Introduction

1.1 Inorganic nanocrystals

Nanoparticles synthesis is currently an area of intense scientific research, due to a wide variety of potential applications of the nanoparticles in biomedical, optical, and electronic fields. The transition of inorganic material dimensions from bulk towards nanometer scale leads to a number of changes in their physical properties such as quantum confinement in semiconductor particles, surface plasmon resonance in some metal particles and superparamagnetism in magnetic materials that are induced by the increase in the surface-to-volume ratio and by their reduced dimensions in the area where the quantum effects predominate.[1]

By decreasing the size of the particle, a gradual increase in the surface-to–volume ratio leads to an increasing dominance of the surface atoms over the atoms in the interior of the particles that affect the properties of isolated particles and their interaction with other materials. Consequently, enhanced surface phenomena and physical confinement due to the particle boundaries induces strongly size-dependent properties. High surface area is a key factor in the performance of the heterogeneous catalysis processes where catalytic activity and selectivity are enhanced through high surface-to-volume ratio and controlled surface features of the nanoparticles. Furthermore, large surface induced enhanced interactions between intermixed materials may result in novel properties of nanocomposite materials.

Less gradual is the transition from classical to quantum mechanics. As the particles reach certain size limit they start to exhibit quantum confinement behavior. For semiconductors, nanoparticles in this size regime have electronic structures between that of the individual atoms and bulk materials. These nanoparticles, also called quantum dots exhibit spectroscopic features as a result of an incomplete band structures caused by limited number of atoms. Although metal can also exhibit quantum confinement effect, it is observed at smaller sizes than in the case of semiconductor nanoparticles. The density of states in metals is reduced to an extent that no longer form a continuous band structure as the size of the metal nanoparticles is well below 2 nm. By reducing the size of metallic nanoparticles, surface optical features are exhibited; in particular the surface plasmon resonance (SPR) absorption band becomes dominant, whereas the bandwidth and width of the absorption band is size dependent.

1.2 Quantum features of the inorganic nanostructures

1.2.1 Surface plasmon resonance

The light absorption by metallic nanoparticles is described by a coherent oscillation of the free electrons within the conduction band that is induced by interaction with the electromagnetic field which leads to an in-phase oscillation.

The electric field of the incoming radiation induces a polarization of the free electrons relative to the cationic lattice.[1] The net charge difference at the nanoparticle surface leads to the formation of a dipole in the nanoparticle which acts as a restoring force. A restoring force creates a dipolar oscillation within the entire particle between the negatively charged free electrons and positively charged lattice resulting in a resonance phenomenon- the surface plasmon resonance (SPR). Surface denotes the polarization of surface charges resulting from the collective electron oscillations whereas plasmon is in analogy to the collective electron oscillations within gaseous plasma as shown in Figure 1.

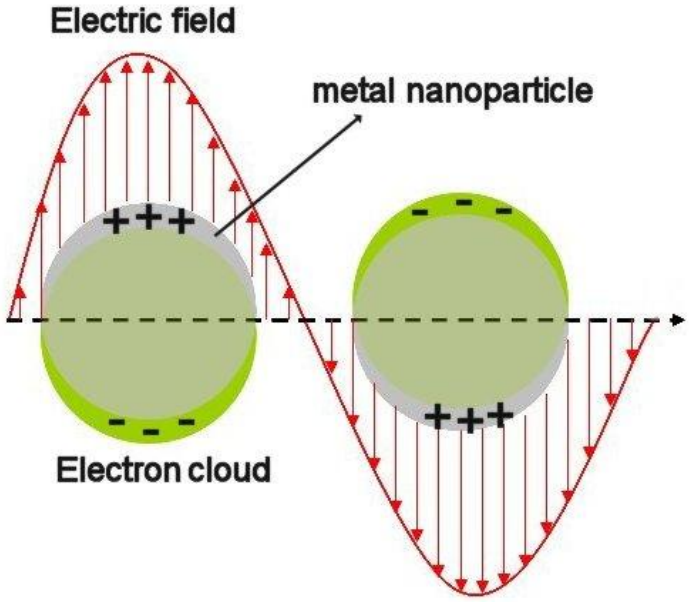

Figure 1. *Excitation of a dipolar surface plasmon in a metal nanoparticle by the electric field of an incident visible light (wavelength, λ).*

A dipolar excitation of the particle between the negatively charged free electrons and it's positively charged lattice induce oscillations within a certain frequency. When the size of a metal nanocrystal is smaller than the wavelength of incident radiation the specific wavelengths of light are absorbed that generate the surface plasmon bands.

The excitation of surface plasmons by light are characterized into two types;[1] as a surface plasmon resonance (SPR) for metal planar surfaces and as a localized surface plasmon resonance (LSPR) for nanometer-sized metallic structures. In the case of localized plasmon resonance incident light is absorbed or scattered by the oscillating electric dipoles within a metal nanoparticle whereas in the case of surface plasmon resonance the polaritons propagate along the surface of a metal in a wave-like fashion until released at some distance from their point of origin.

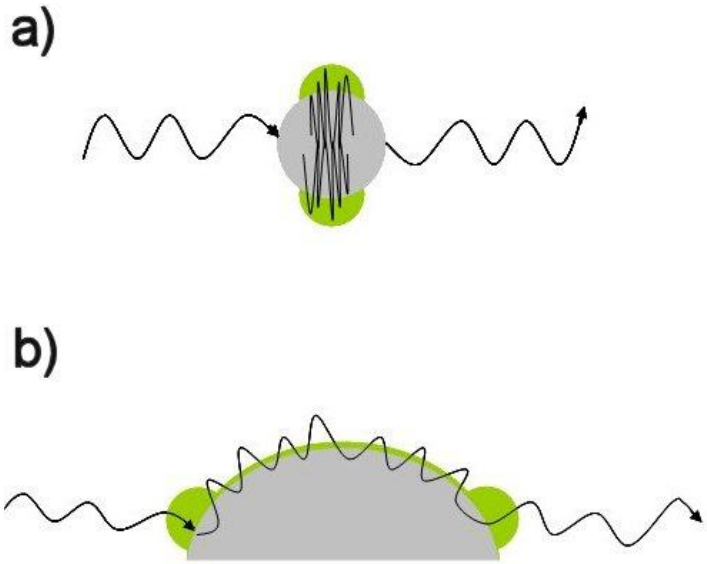

Figure 2. *Excitation of conduction electrons lead to local electromagnetic field (green) near the metal surfaces; a) localized plasmon resonance and b) surface plasmon waves induced by incident light on nanostructured metal surfaces.*

The spectral properties of the SPR have been extensively studied and compared to the Maxwell relations. The energy of the SPR bands of the metallic particle depends on both the free electron density and the surrounding dielectric medium. In the extrinsic size regime, for the particle size above 20 nm, the solution of the Maxwell equation for the electrodynamic calculations leads to the multi-pole oscillation higher order modes which mean that the light can no longer

homogeneously polarize the particle. Consequently, for the extrinsic size effects the plasmon resonance depends solely on the particle size.[2] The peak of higher-order modes is shifted to lower energies. As a result, the plasmon band red shifts and plasmon bandwidthh increases with increasing particle size as shown in Figure 3.

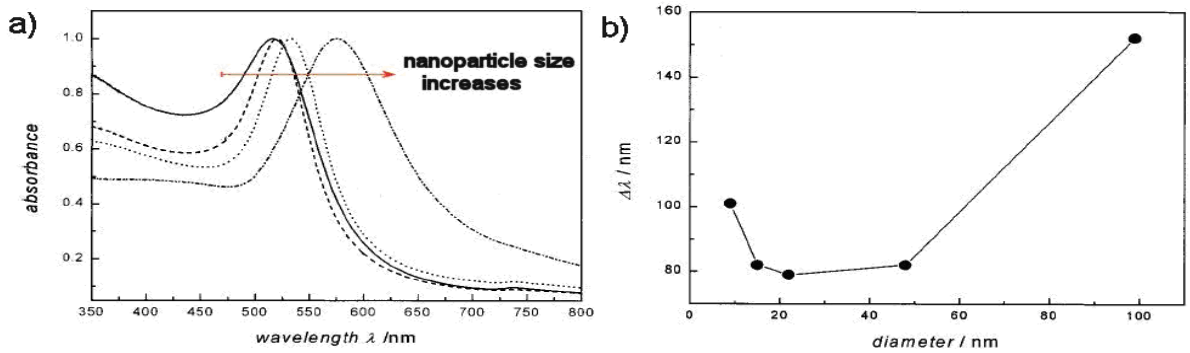

Figure 3. *Extrinsic region; direct dependence of the SPR on the particle size. a) UV-vis absorption spectra of gold nanoparticles in the size regime from 9 to 99 nm, b) the plasmon bandwidthh as a function of particle diameter.*

For metallic nanoparticles significantly smaller than the wavelength of light, light absorption is within a narrow wavelength range. As the metal particle size approaches to the electron mean path the existence of intrinsic-size effect occurs in the optical response of the nanoparticles. When particles are much smaller than the incident wavelength of light ($2r << \lambda$) the particles experience a constant electric field within interior of the particle (the quasi-static limit) and feel the electric field that is spatially constant with a time dependent phase.[1,3] As a response to a characteristic electromagnetic frequency strong optical extinctions (extinction = absorption + scattering) of conductive metal nanoparticles arise.

Mie was the first to solve Maxwell's equation for light interacting with small spheres. Assuming that nanoparticles behave as frequency-dependent dielectric media, Mie's solution yields the particle extinction cross-section, C_{ext}.

Since in the intrinsic size region only the dipole oscillations contributes to the extinction cross section, analytical solution of the Maxwell equation is simplified to the relationship of dipole approximation according to the Mie theory.[4]

$$\sigma_{ext}(\omega) = \frac{9\omega\varepsilon_m^{3/2} V\varepsilon_2(\omega)}{c\left[\varepsilon_1(\omega) + 2\varepsilon_m\right]^2 + \varepsilon_2(\omega)^2} \qquad \text{(Eq.1)}$$

Where V is the particle volume, ω is the angular frequency of the exciting light and ε_m and $\varepsilon(\omega)=\varepsilon_1(\omega)+i\varepsilon_2(\omega)$ are the bulk dielectric constant of the matrix material and the particle, respectively. The resonance is obtained as $\varepsilon_1(\omega)= -2\ \varepsilon_m$, if ε_2 is small or weakly dependent on ω. The extinction coefficient does not depend on the particle sizes as it is observed experimentally. This discrepancy is ascribed to the assumption in the Mie theory, that electronic structure and dielectric constant of the particles are equal to those in their bulk form, which is no longer valid as the particle size is decreased. Furthermore, in small particles, when the mean free path of the conduction electrons is larger than the dimension of the particles electron surface scattering becomes significant. The electron mean free path describes the quasi-elastic scattering of conduction electrons. In the case of silver electron mean free path is about 50 nm. As the size of the nanoparticles is reduced, the electrons faster reach the surface, scatter and lose their coherence. As a result, the plasmon bandwidthh increases with decreasing particle size. In the case of silver, intrinsic peak broadening occurs as the diameter of the particle is below 10 nm. The reduction of the effective electron mean free and enhanced electron scattering at the particle surface can explain the size dependence of the plasmon absorption.
Phenomenological damping constant (γ) is found to be a function of particle size

$$\gamma = \frac{\gamma_0 + A\nu_F}{r} \qquad \text{(Eq.2)}$$

where γ_0 is the bulk damping constant dependent on the electron scattering frequency, A is a scattering process constant, ν_F is the velocity of electrons at the Fermi energy and *r* is the radius of the particle. In the intrinsic size region where the dielectric function is material size dependent the absorption wavelength increases while the peak width decreases with increasing particle size.[5,6]

The most important factor in determining the frequency and intensity of plasmon resonance for a certain metal is the charge separation since it provides the main restoring force for electron oscillation. However, exact equations of Maxwell's equation are geometry limited. Therefore, for various other particle shapes, the discrete dipole approximation (DDA) is required for solving the Maxwell's equation.[7]

In a DDA approximation nanoparticle is discretized into a cubic array of N polarizable points, where each point represents the polarizability of a discrete volume of the material. Based on discrete dipole approximation calculations (DDA)[6] silver nanosphere primarily absorb blue light, where the SPR spectrum shows the presence of two resonance peak; the main at 410 nm and a smaller peak at 370 nm present as a shoulder. The dipole resonance arises from one side of a sphere surface being positively charged while the opposite is negatively charged which induces a dipole moment in the particle. For non-spherical particles, the resonance wavelength depends also on the orientation of the electric field. As the shape deviates from the spherical the optical spectrum exhibits more peaks than that of the sphere due to several distinct symmetries for dipole resonance compared with only one for the sphere. The number of resonance frequencies that a nanostructure exhibits increases with the increasing number of ways that it can be polarized. Furthermore, in nanostructures with sharp edges surface charges accumulate at sharp corners, which increases charge separation and thereby reduce the restoring force for the electron oscillation. Due to weaker restoring force the most intense peak of the SPR is red shifted in compare to spherical SPR.
Two dimensional nanostructures (2D) allow increased charge separation if polarized along their long axis and therefore the SPR peak is red shifted from more isotropic structures. Furthermore, the intensity of the resonance peak increases with an increase in the effective dipole moment of the particle that is larger if charges separate with mirror symmetry.

In Figure 4, DDA calculations are presented that illustrate several ways in which the shape of the nanostructure affects the frequency and intensity of nanostructure scattering and absorption of light.

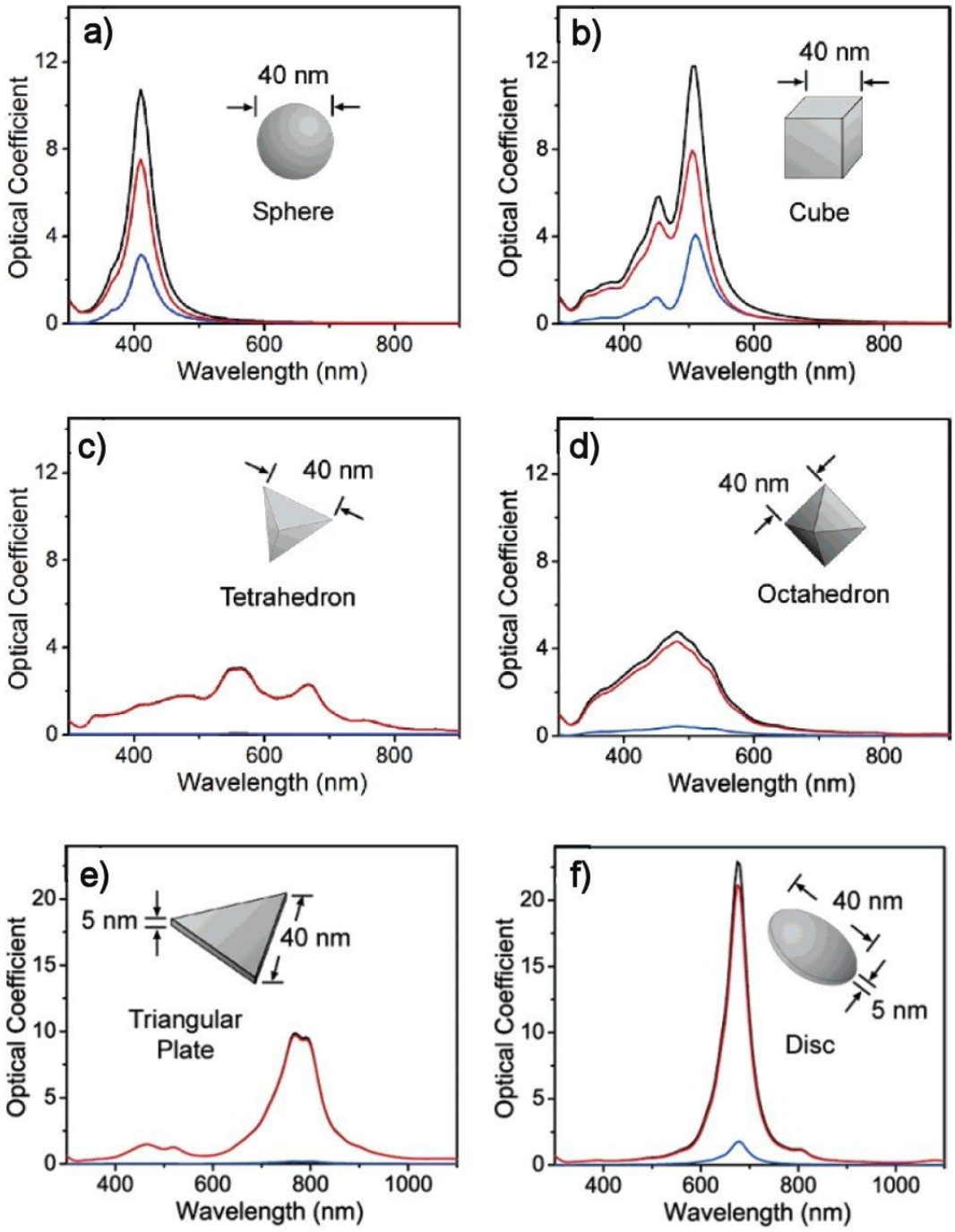

Figure 4. *The calculated UV-vis extinction (black), absorption (red), and scattering (blue) spectra of silver nanostructures, illustrating the effect of a nanostructure's shape on its spectral characteristics. An isotropic sphere (a) exhibit spectra with a single resonance peak. Anisotropic cubes, (b) tetrahedra (c) and octahedral, (d) exhibit spectra with multiple, red-shifted resonance peaks. The spectra of a triangular plate (e) and circular disc (f) illustrate how resonance peaks red-shift for particles with 2D anisotropy.*[6]

1.2.2 Quantum confinement effect

By reducing the size of the semiconductors to the nanometer regime the nanoparticles exhibit the properties due to quantum confinement. The quantum confinement effect can be observed once the diameter of the particle is smaller than the average distance between electron and hole, known as the bulk exciton Bohr radius. These materials, also referred to as nanocrystals or quantum dots, exhibit spectroscopic features that result from an incomplete band structure caused by the limited number of atoms.

When the confining dimension of the particle is large compared to the wavelength of the incident light the bandgap remains at its original energy. As semiconductor nanoparticles become smaller than the Bohr radius, electrons feel the presence of the particle boundaries and respond to the changes in particle size by adjusting their energy. As a result to the decrease in the confining dimension to the nanoscale, the continuous energy bands of a bulk material turns to discrete, atomic-like energy levels.[8-11]

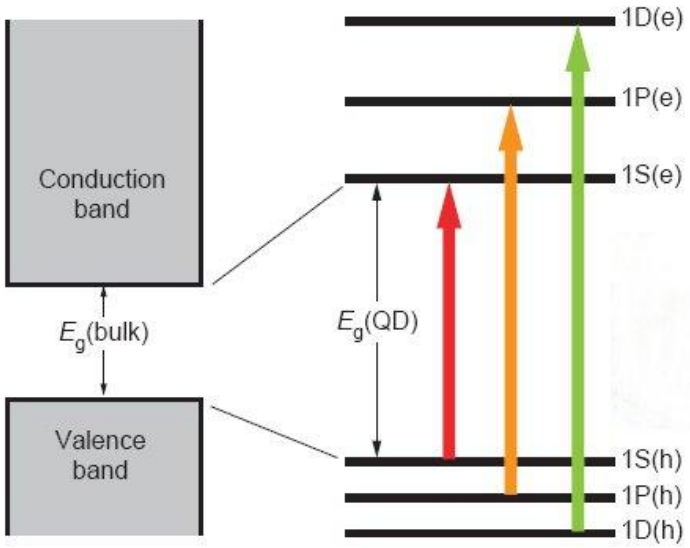

Figure 5. *The scheme of a bulk semiconductor with continuous conduction and valence energy bands separated by a "fixed" energy gap, Eg (bulk). Electrons normally occupy all states up to the edge of the valence band, whereas states in the conduction band are empty. (left) A QD is characterized by discrete atomic-like states with energies that are determined by the QD radius R. These well-separated QD states can be labeled with atomic-like notations, such as 1S, 1P, and 1D.(right)*

In the first approximation, the quantum confinement effect can be described by a quantum box model, in which the electron motion is restricted in all tree dimensions;

$$E_g(QD) \approx E_{g0} + \frac{\hbar^2 \pi^2}{2 m_{eh} R^2} \qquad \text{(Eq.3)}$$

where effective mass is defined as

$$m_{eh} = \frac{m_e m_h}{m_e + m_h} \qquad \text{(Eq.4)}$$

For a spherical nanoparticle with radius R, the model predicts that a size dependent contribution to the energy gap is simply proportional to $1/R^2$, which implies that the bandgap becomes size dependent, such that as the nanocrystal size decreases the gap increases. Consequently, both the optical absorption and emission of quantum dots shift to the blue (higher energies) as the size of the nanocrystal gets smaller. Hence by changing the size of the nanocrystal, its absorption and emission characteristics can be tuned.[11-12]

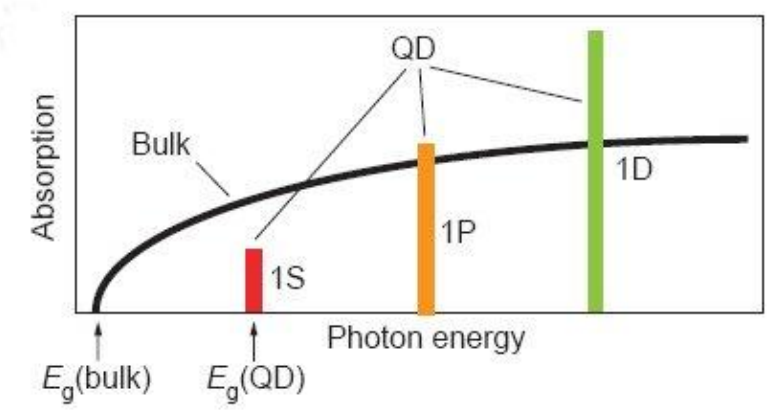

Figure 6. *The schematic represents the continuous absorption spectrum of a bulk semiconductor (black line) compared with a discrete absorption spectrum of a QD (colored bars).*

By reducing the size of the nanoparticles to nanometer regime, due to large surface to volume ratio a significant number of atoms in the particle is located at the

surface. Thus the control over the crystal structure and surface defects is necessary in order to obtain desirable properties.

In the case of non-linear optical properties surface defects are desirable due to the optical processes such as intraband and excited-state relaxation,[4] whereas in luminescence properties defects are undesirable. The defects lead to the electronic states within the material energy gap into which the electrons can relax. From those states the electrons typically undergo non-radiative or radiative in gap deep trap emission to the ground state yielding carrier losses. Carrier losses attributed to the surface defects or dandling bonds may inhibit the optical gain. For luminescence properties, unpassivated surfaces enhance surface trapping and recombination that result in weak luminescence efficiency. Thus, modification of the nanoparticle surface that involves the controlled electronic passivation of the surface is necessary in order to control nanoparticle optical properties. Capping of the nanoparticle surface with higher band gap materials, another semiconductor or a layer of organic molecules, has been shown to improve the photoluminescence quantum efficiency by passivating surface nonradiative recombination sites.[13]
Furthermore, optical properties of the semiconducting nanocrystals can be tuned by doping the semiconducting nanocrystal with the impurity atoms. The impurity states localize the excitation before nonradiative processes of the defect states can occur and hence improve the fluorescence quantum yield. Interaction of the impurity atom with the host matrix induces the competition between radioactive and nonradiative pathways that is manly affected by the concentration of the impurity atoms in the host matrix and the state of the nanocrystal surface. By introducing the impurities into pure semiconducting nanocrystals new energy levels appear within the band gap that enable tuning of the semiconducting nanocrystal emission wavelength. Hence, by controlling the size and surface characteristics of the inorganic nanoparticles with appropriate choice of the synthesis approach and conditions final characteristics of the nanostructured materials can be tuned and changed.

1.3 Inorganic Nanoparticle synthesis

For the nanoscale structure and device fabrication both, top-down and bottom-up approaches have been established, whereas bottom up approach has resulted in better control over the properties of the synthesized nanoparticles. In the top down approach, large objects are modified to give smaller features by various mechanical (ball milling),[14] thermal (gas atomization),[15] chemical (etching),[16] and high energy methods such as laser ablation of solid targets.[17] With these techniques, it is difficult to design and control the process to produce desired particle shape that is limited by an inherent size limit that exceeds the limit of the bottom up approach.

Conversely, bottom up approach provide access to extremely fine features and state of the art structures with control over extend of defects and impurities. With the bottom up mechanism, the chemical synthesis methods (molecular self assembly, supramolecular chemistry)[18] stand in contrast to the physical methods (ion implantation, electrolytic deposition, molecular beam epitaxy) that can produce nanoparticles with well defined shape, sizes and crystallinity but often requires extreme conditions such as ultra high vacuum and high temperatures. With these techniques fabricated nanomaterials are difficult to manipulate on different solid supports. Thus, chemical methods have developed in order to synthesize uniform and well defined particles of variety of compositons and manipulative form.

In the nanoparticle fabrication beside size control, uniform size distribution, morphology, crystallinity and chemical composition are required for any potential practical applications. The most prevalent chemical synthetic methods that enable obtaining these preperties are the solution synthesis of inorganic nanostructures employing organic species that can coordinate to the surface of the inorganic nanostructures and the preparation of inorganic species in a coordinating matrix.[19] In general, in chemical synthesis methods the nanoparticle formation follows thermo dynamical equilibrium and kinetic growth mechanism. The thermodynamic approach consists of generation of the supersaturation, nucleation and subsequent growth of inorganic species. While both reaction regimes are present in any synthesis, the formation of nanoparticles can be controlled by kinetic mechanism as the amount of precursors available for the growth is limited or the process is confined in a limited space such as solid templates, aerosols or micelles.[20]

1.3.1 Nanoparticle growth by homogeneous nucleation

In various medium (solution, gas or solid) nanoparticles are formed by homogeneous nucleation as supersaturation is created. A supersaturation is obtained by reduction in temperature of an equilibrium solution or through in-situ chemical transformation of highly soluble chemicals into less soluble by chemical reaction.

As the concentration of the solute exceeds its equilibrium solubility, due to high Gibss free energy of solution segregation of the solute from solution occur in order to reduce the energy of the system. The reduction of the overall Gibbs energy (ΔG) of the solution is the driving force for the nucleation and growth of the solid phase.

The change of free energy per unit volume of the solid phase is solute concentration dependent

$$\Delta G_v = -\frac{kT}{\Omega}\ln(1+\sigma) \qquad \text{(Eq.5)}$$

where K is the Boltzmann constant, T is the temperature ,Ω is the atomic volume and σ supersaturation defined by $(C-C_0)/C$, where C is the concentration of the solute and C_0 its solubility. As the equilibrium concentration is exceeded negative change in the free energy causes the spontaneous nucleation of the solid phase. If the super-saturation is not obtained, ΔG is zero and nucleation does not occur. For the spherical nucleus of radius r, the change in molar free Gibbs energy ascribed to the formation of solid phase is defined by

$$\Delta\mu_v = \frac{4}{3}\pi r^3 \Delta G_v \qquad \text{(Eq.6)}$$

On the other hand, this energy reduction is balanced by introduction of the surface energy due to the formation of new phase. The surface energy of the system is increased according to the equation

$$\Delta\mu_s = 4\pi r^2 \gamma \qquad \text{(Eq.7)}$$

where γ is the surface energy per unit area.

Therefore, as a result of nucleus formation the total change of the chemical potential is given by:[21]

$$\Delta G = \Delta\mu_v + \Delta\mu_s = \frac{4}{3}\pi r^3 \Delta G_v + 4\pi r^2 \gamma \qquad \text{(Eq.8)}$$

In Figure 7 the change of volume free energy, surface free energy and total free energy as a function of nucleus radius is schematically illustrated.

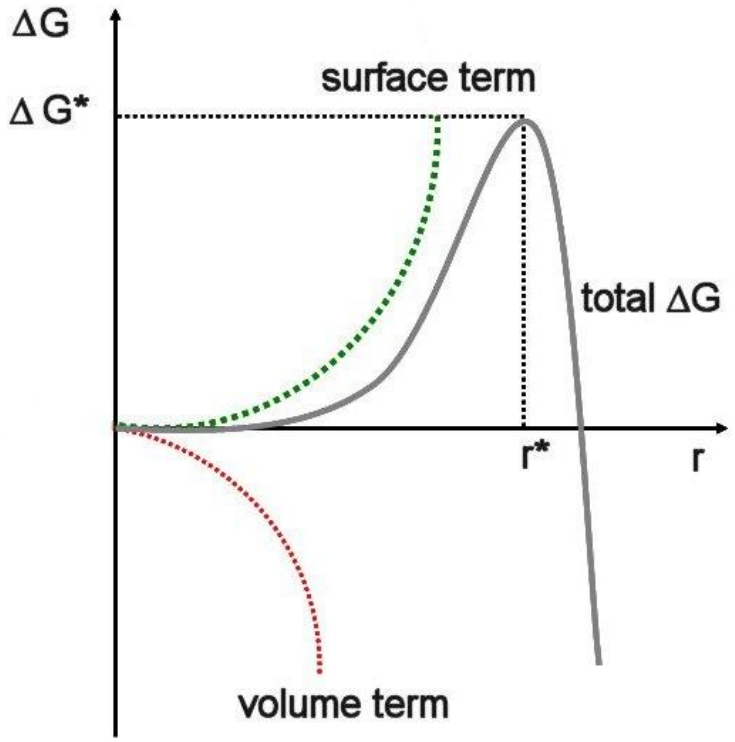

Figure 7. *The schematic diagram illustrating the change of volume free energy, surface free energy and total Gibbs free energy (ΔG) as a function of particle radius.*

In the nanoparticle synthesis from the supersaturated solution the critical radius (dG/dr=0) present the lower limit of the particle size.[22] Below the critical radius a nucleus dissolves into the solution to reduce the total Gibbs energy while the nucleus beyond the critical size limit is stable and continue to grow until the concentration of growth species reaches the equilibrium concentration. Therefore, to reduce the limit of particle size in the synthesis process, the increase in volume free energy and a decrease in surface free energy of a new phase are necessary

which can be obtained by controlling super-saturation, temperature and by varying the type of solvents in the process. Uniform distribution of the nanoparticles in the synthesis process is obtained if all nuclei are formed simultaneously.[23] A sharp nucleation is achieved by abrupt increase in the concentration of the growth species beyond the minimum saturation required to overcome the critical energy barrier followed by a quick fall in the supersaturation. As a result nuclei are likely to have similar size and the same subsequent growth which yield monodispersed particles.
In Figure 8 the processes of nucleation and growth for the synthesis of monodispersed nanoparticles is schematically illustrated.

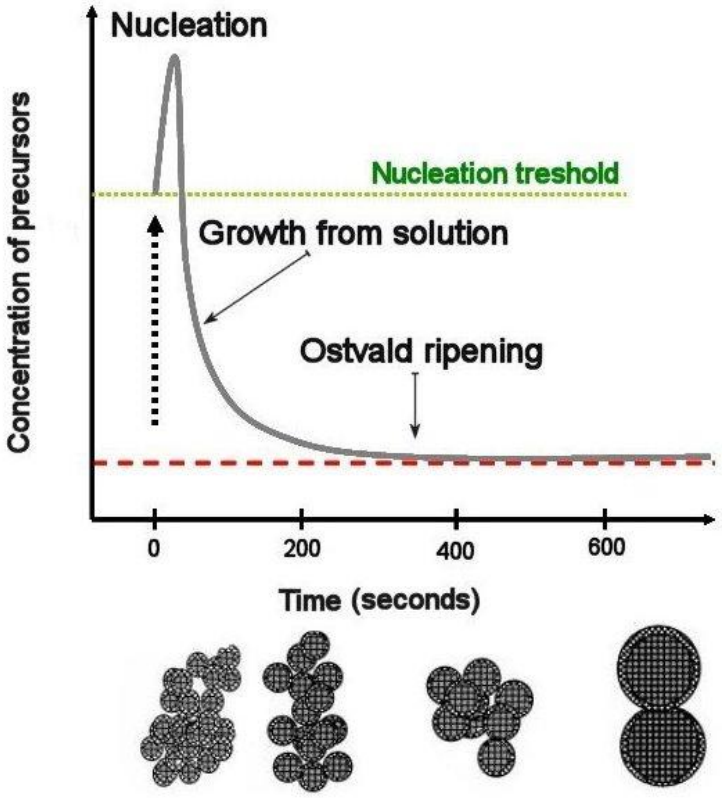

Figure 8. *The schematic illustration of the nucleation and growth processes.*

However, the subsequent growth of the initial nuclei may result in the change of the particle size distribution. The growth process involves the diffusion of the growth species from the bulk solution to the particle surface which is followed by incorporation of the species adsorbed on the surface into a solid structure.
As the concentration of the growth species is reduced below the nucleation threshold, nucleation stops and the growth of the nanoparticles is controlled by

diffusion. In the growth process where the diffusion to the surface is sufficiently rapid the growth rate is controlled by surface process. In the diffusion controlled growth mechanism, the growth rate is inversely proportional to the radius of the initial nucleus, whereas in the surface reaction controlled growth the growth rate is proportional to the surface area of the nucleus. Thus, the diffusion controlled growth process promotes the formation of monosized nanoparticles, while polydispersity is favored with prolonged time as the surface growth process prevails.[24]

Solution chemical synthesis methods normally involve the dissolution of the precursor in a solvent with appropriate coordinating agents. The precursors like metal ions or organometallics are precipitated in the presence of coordinating agents that mediate particle growth. With the solution synthesis, due to the sterical or electrostatic stabilization of the inorganic nanostructures the organic ligand environments establish the solution properties of the nanoparticles and maintain their nanoscale integrity by preventing their agglomeration.

For the metal nanoparticle synthesis a dilute solution of metal complexes accompanied with the variety of methods to initiate and control the reduction reactions have been developed. Monodipersity of metallic nanoparticles in colloidal solutions is obtained by combining two key parameters that hinders the diffusion of growth species to the nanoparticle surface, the concentration of the solute and polymer monolayer adhered to the nanoparticle surface. These parameters enable the diffusion process to be the rate limiting step in the growth of initial nuclei which yield monodispersed nanoparticles. Furthermore, the size distribution of metallic nanoparticles in the synthesis process is strongly influenced by the type of the reduction reagents used in the synthesis.[25] While strong reduction reactions normally enable a fast reaction rate and hence favors the formation of smaller particles, weak reduction process due to the slow reaction rates favors the formation of larger particles. Furthermore, in the reduction process with slow reaction rate the continuous formation of nuclei may result in a wide size distribution. On the other hand, in the process where no further nucleation occurs, a slow reaction rate would result in diffusion limited growth of the primary nuclei yielding narrow size distribution of the synthesized particles.

While polymer stabilizers are primarily introduced into the solution to form a monolayer at the particle surface and hence prevent the particle agglomeration, they on the other hand affect the particle growth process during the particle formation. The control over the reduction reaction rate is obtained by controlling the amount of polymer in solution. By increasing polymer concentration which act

as a diffusion barrier, the growth of the initial nuclei is diffusion controlled which favors the formation of monosized particles.[26]

For the production II-VI semiconductor nanoparticles, one of the most successful solution synthesis methods involves precipitation from a solution of organometallic precursor in a hot coordinating solvent with the presence of surfactants.[27] The key factor of these methods that provides the monodispersity of the synthesized nanoparticles is the separation of the nucleation and growth steps.[28]

Fast nanocrystal nucleation due to an abrupt supersaturation fallowed by uniform growth of the formed nuclei leads to fairly narrow size distribution, whereas the surfactant electronically passivate the nanocrystal surface and preventing nanocrystal aggregation as well as providing solubility of nanoparticle in an organic media. The Ostwald ripening during aging at increased temperatures promotes the growth of large particles at the expense of smaller ones, narrowing the size distribution. Although organometallic preparations enable the production of high quality nanocrystals with high quantum yields, the pyrophoricity and toxicity of the precursor has to some extent limited their accessibility. Recently less toxic precursors have been used for the preparation of II-VI semiconducting quantum dots and new procedures have been developed that enable the high quantum yield monodispersed nanocrystal formation.

Conversely to metallic and non-oxide semiconductor nanoparticles, for the synthesis of oxide colloids, oxide hybrids and surface engineering of nanostructures sol-gel process is generally utilized.[29] Typical sol-gel processing consists of hydrolysis and condensation of either metal alkoxide or inorganic and organic salts. By controlling the hydrolysis and condensation reaction the size of the nanoscale clusters, morphology and microstructure of the product can be tailored. The sol-gel process enables incorporation of the organic components in the metal oxide network for the formation of organic-inorganic hybrids. One possible way in the formation of inorganic-organic hybrid is simultaneous hydrolysis and condensation of the inorganic and organic precursor resulting a single phase material in which the organic and inorganic component is linked through chemical bonds.[30] By linking the organic component to the inorganic precursor the rate of the hydrolysis and condensation reaction can be modified which enables the control over the final properties of the hybrid material. The variations in the concentration of the precursor and aging time lead to the formation of oxide particle size in the size range between 1 to 100 nm. Another possible approach of hybrids formation is physical trapping of the organic component in the inorganic oxide network, where

the key parameters to control particle size is to promote temporal nucleation accompanied with subsequent diffusion-controlled growth.[31] The organic ligand environment used to passivate the surface of inorganic nanoparticles maintains their nanoscale size by preventing particle aggregation and enables the nanoparticles to retain their physical properties by controlling the surface state of the nanostructures. One of the most promising approaches in organic-inorganic hybrid materials fabrication is found in attempts to integrate inorganic nanocrystals and polymers. The unique properties of polymers including their processability and ability to assemble polymer in ordered structures offer the key challenges in producing nanocomposites that combine the desirable properties of nanoparticles and polymers. Since nanoscale particles in general possess a strong tendency to aggregate, the critical challenge in designing inorganic-organic nanostructures is based on the ability to control the spatial distribution of inorganic objects in the host organic matrix.

Two synthesis approaches, the ex-situ[32] and in-situ[33-34] incorporation of the inorganic objects into a polymer matrix, have been followed for the formation of inorganic-organic nanocomposites. Of these, the ex-situ synthesis methodology, based on the simple mixing of two different phases, usually yields heterogeneous structures as a result of the formation of strongly connected aggregates, induced by the high specific surface energy of the nanoparticles. On the other hand, the tendency for particle aggregation can be reduced by in-situ inorganic nanoparticle synthesis within the polymer matrix or by the in-situ polymerization of an organic matrix around the inorganic particles dispersed in a solvent. Since the inorganic nanoparticles are confined within the polymer matrix, this limits their aggregation and results in the formation of a homogeneous inorganic-organic nanocomposite. With the ability to control the interactions between the polymer matrix and the nanocrystal surfaces a uniform distribution of the inorganic nanoparticles in the polymers can be obtained.[35]

1.3.2 Kinetically confined growth of inorganic nanoparticles

The nanoparticle growth is also kinetically controlled as the nanoparticle synthesis is performed by the limited amount of precursor or in a limited space, such as solid matrices. The synthesis of inorganic nanoparticles in solid matrices has similar requirements as solution synthesis approach; dissolution of nanoparticle precursor s in the matrix and binding of the precursor to the appropriate matrix functionality, while the particle size control is also affected by physical interactions between the particles and surrounding matrix. Different template synthesis approaches such as reverse micelles,[36] vesicles,[37] zeolites[38] and block copolymer domains[39] have been involved for inorganic nanoparticles syntheses.

Among them, micro-phase separated diblock copolymers were successfully utilized in controlling inorganic nanoparticle size and distribution by attaching metal complexes to one of the block prior domain formation or by sequestering of metals into preformed domains of block copolymers.[40-45] Various post binding chemical treatments on a metal-containing domain yield inorganic nanoparticle formation. Sequestering of inorganic precursors within confined domains, followed by uncontrolled growth leads to one inorganic crystal per domain. If domains contain the same amount of precursors, this synthesis strategy can lead to the formation of monodisperse nanoclusters.

Various semiconductor and metal nanoparticles syntheses have been reported using the block copolymer approach.[46-50] The primary drawback of the block copolymer synthesis scheme is a difficult control over the extend of the metal ion loading within domains, which usually result in more than one primary particle per block copolymer microdomain. Furthermore, uniformity of the microdomains sizes also yield relatively large size distribution of the synthesized nanoparticles.[51-52] However by controlling the synthesis processing parameters the nunocluster size can be manipulated. In the case of metal sulfide nanocluster formation from metal carboxylate precursor, higher temperature of the reaction with H_2S (gas) or the presence of coordinating solvents result in larger nanocluster formation.[43, 47]

The nanoparticle growth within the matrix is initiated from a homogeneous nucleation followed by subsequent growth. However, the increase in nanoparticle size in polymer domain can be explained by diffusion of small primary inorganic nanoparticles which in turn aggregate to form larger agglomerates of crystallites.[43] By controlling the synthesis parameters that affect nanocluster growth process nanoparticles with controlled size and size uniformity in solid matrices can be synthesized. Normally, the aggregative growth result in the formation of dendritic

structures with characteristic fractal dimensions, where the structure of the agglomerate formed is balanced by a diffusion process which involves the competition between the rate of collision and coalescence.[52] While fast collision rates result in the formation of fractal structures, high coalescence rate produce larger spherical agglomerates.[53]

The diffusivity D of a sphere is described by the Stokes-Einstein relation [54-57]

$$D = \frac{kT}{6\pi\eta R} \qquad \text{(Eq.9)}$$

where T is the temperature, R is the sphere radius and η is the effective viscosity experienced by the particle. The variation of the polymer viscosity with temperature is described by the Williams-Landel-Ferry (WLF) equation [58]

$$\log\frac{\eta(T)}{\eta(T_g)} = -\frac{C_1(T - T_g)}{c_2 + T - T_g} \qquad \text{(Eq.10)}$$

Where C_1 and C_2 are the constants and Tg is the glass transition temperature of the polymer. Particles in polymers undergo Brownian motion that involves segmental motion of the polymer. As a result particles in the surrounding polymer medium experience the viscous forces associated with the polymer. The combination of the eq. 9 and eq. 10 determines the diffusivity of the particle as the temperature is varied.

In various polymer matrices it is assumed that the particle is stabilized by the interactions between the surface of the nanocluster and polymer ligand. In diffusion-reaction growth mechanism particle growth stops as the particle is stabilized by the surrounding polymer. The interaction between the ligand (L) and the cluster surface (Cs) is assumed to be reversible, where (#LCs) present the number of cluster-ligand bonds.

$$L + C_s \leftrightarrow LC_s$$

The nanoparticle growth stops when (#LCs)r cluster –ligand bonds are formed which trap the nanocluster in the energy well $-(\#LCs)_r \Delta H >> kT$, where ΔH is the enthalpy change for the formation of a ligand –cluster bond. For nanoparticle of a certain size at certain temperature there is an equilibrium number of bonds formed between the ligand and the cluster surface, while the growth of the nanoparticles is terminated as the $(\#LCs)_r \leq (\#LCs)_{eq.}$

Within the confined solid matrices diffusion limited aggregative growth of the inorganic species stops as Damkobler number (Da) is

$$D_a = \frac{\sigma_d}{\sigma_r} >> 1 \qquad \text{(Eq.11)}$$

where σ_d is a diffusion time and $\sigma_{r\ is}$ a reaction time.

The diffusion time is defined as

$$\sigma_d \approx \frac{L^2}{D} \qquad \text{(Eq.12)}$$

with L as the distance between two particles and D as diffusity and reaction time as

$$\sigma_r = (\#LCs)_r / (d(\#LCs)/dt)_{t=0} \qquad \text{(Eq.13)}$$

However, under some conditions of nanoparticle growth in polymers Ostwald ripening mechanism must be considered. If the reaction of the nanoparticle formation in domain is performed under aqueous or acidic conditions under which the particles can dissolve into free ions, the activation energy for the Ostwald ripening is expected to be low and as a result Ostwald ripening may be the dominant mechanism for the particles growth.
However, the Ostwald ripening can not explain the growth of the nanoparticles and their size distribution as the reaction of nanoparticle formation is performed under gaseous conditions at high temperatures as free ions will not be solvated thus the activation energy for dissolution-precipitation growth is expected to be high.[59] In

this case, the nanocluster size is stable and no change in the size distribution is observed.

Since potential application of inorganic nanoparticles mostly requires their assembly in the form of thin films, several technologies to fabricate inorganic-organic composite structures have been utilized. Among others, the formation of nanocomposites, consisting of inorganic nanocrystals embedded in polymer matrices, yields materials that combine the convenient processing and structural flexibility of the polymers with the stability of inorganic objects that have a controlled size on the nanometer scale.[60] Embedding the inorganic nanoparticles within a suitable matrix, with control over the particles' surface states and the size distribution, provides control of their physical properties, thus making such inorganic-organic nanostructured materials more attractive for their potential applications in the areas of electroluminescence devices, lasers, light-emitting diodes, solar cells and flat-panel displays.[61-62]

Nanoparticulate thin films with an additional level of structuring and control over the film thickness can be obtained by the electrostatically driven self-assembly of preformed inorganic nanoparticles on charged surfaces. The nanoparticles can be electrostatically assembled in the form of thin films as monolayer or multilayer superlattices, using self-assembled monolayers (SAMs) or the Langmuir-Blodgett (LB) technique.[63] While the LB technique requires special equipment and has several limitation with respect to the topology of the substrate, SAMs based on covalent or coordination chemistry are limited to certain classes of organics where the steric hindrance of the covalent bonding lowers the reaction yield which is the key factor for the preservation of the layer functional group density. It was therefore desirable to develop a simple approach for the nanostructured thin film fabrication with precise control over individual layers and deposition process independent of the nature of the substrate. Among these the Layer- by- Layer processing has distinct advantages since PEMs films can be prepared on a wide range of surface materials and geometries with precise control over the thickness and molecular structure in nanometer scale.[6]

1.4 Polyelectrolyte Layer-by-Layer self assembly

Polyelectrolytes present a group of polymers with ionizable groups on each monomer repeat unit. They are categorized as strong as their degree of ionization is solution pH independent and as weak if their degree of ionization is pH dependent. The LbL self-assembly technique, first developed by Decher,[64] has been described as the alternating deposition of oppositely charged polyelectrolytes on substrates where the electrostatic interaction between the two components is the driving force for the multilayers build up. Upon the adsorption of a polycation onto the negatively charged substrates, the negative charges of the substrate are reversed to positive, favoring the subsequent adsorption of polyanions. The Layer by layer process is shown schematically in Figure 9.

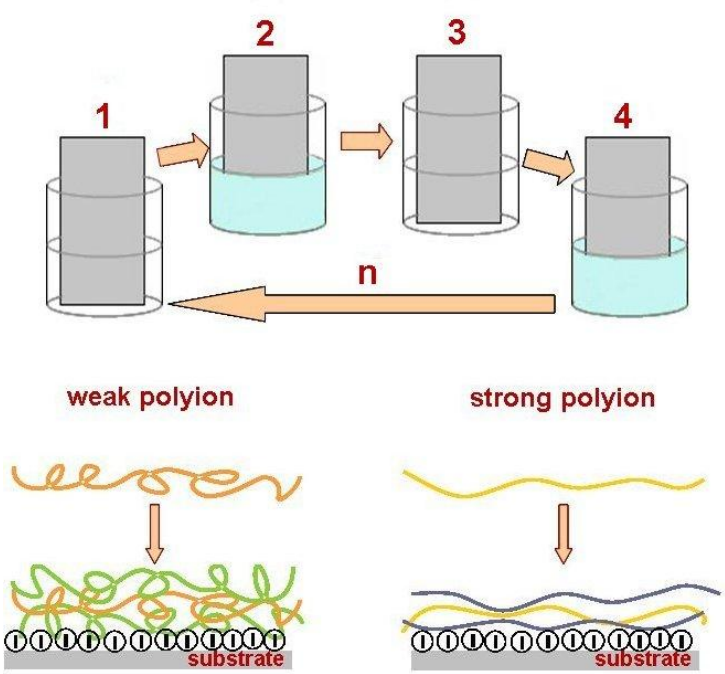

Figure 9. *The schematic of the film deposition process using slides and beakers. Steps 1 and 3 represent the adsorption of a polyanion and polycation, respectively, and steps 2 and 4 are rinsing steps. The polyion conformation and layer interpenetration for the assembly of weak and strong polyions is shown.*

A build up of multilayers is normally performed by cycling a substrate between two aqueous solutions of polyelectrolytes of opposite charge, with a rinse step in pure water following each immersion. A layer of polymer adds, via electrostatic forces, to the oppositely charged surface, reversing the surface charge and thus priming the film for the addition of the next layer. After drying, a mechanically and thermally stable polyelectrolyte multilayer structure is obtained.

The thickness of the polyelectrolyte multilayer film depends on the type of polyelectrolyte used in the assembly and is linearly increased with the increasing number of polyelectrolyte layers. In the assembly of strong polyelectrolytes, due to the fully ionized groups the polyion chains normally adsorbing in a thin, distended conformation (Figure 9). For the multilayer films composed of strong polyelectrolytes, the thickness and structure of the multilayer film can be controlled by the addition of salt to the polyelectrolyte solution.[65] By increasing the ionic strength of the solution, the charges on the polyelectrolyte chains are shielded which reduces the screening length between the charged groups and thus allow the polyelectrolyte chains to adopt more randomly coiled conformation which results in a thicker layer. For the assembly of strong polyions of poly(sodium 4-styrenesulfanate) (PSS) and poly(diallyldimethylammonium) chloride (PDDA) polyion the layer thickness can be varied in the range from 1 nm to 4 nm, depending on the concentration of the salt in the solution.[66]

In the assembly of weak polyelectrolytes, better control over the physical state of the assembled polymers, such as linear density, thickness, molecular conformation and degree of interchain ionic bonding is obtained.[67] Due to the variation in the degree of weak polyion chain ionization induced by the change in the solution pH the structure and thickness of multilayers can be manipulated. Comparing to strong polyelectrolytes, where the molecular conformation can be controlled by the ionic strength of polyion solutions, the variations in the assembly pH in the case of weak polyions presents a more flexible parameter for controlling the molecular architecture of the assembled multilayer films. Moreover, while the ionic strength affects all parts of the polyion chain equally and limits the solubility of the high molecular weight polyelectrolytes, the pH enables ionization of controllable fraction of the functional groups of the weak polyion chains.[68]

In Figure 10 the most common polyelectrolites used in the LbL self assembly process are shown.

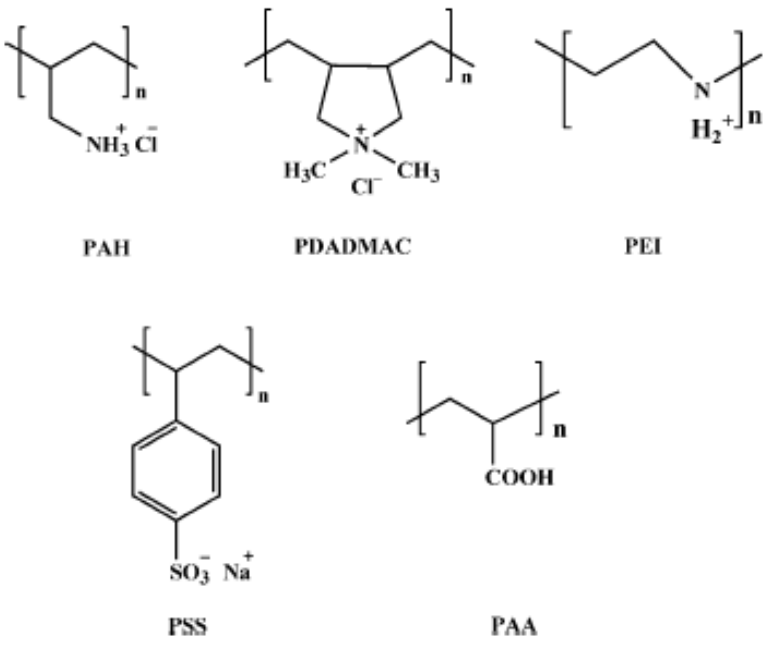

Figure 10. *Molecular structures of most commonly used strong and weak polyions; PAH- poly(allylamine)hydrochloride,PDADMAC- poly(diallyldimethylammonium) chloride, PEI- poly(ethylenimine), PSS- poly(sodium 4-styrenesulfanate) and PAA- polyacrylic acid.*

The molecular organization of multilayer films composed of weak polyelectrolytes of polyacrylic acid (PAA) and polyalyllamine (PAH) assembled on various substrates have been investigated as a function of the assembly pH.[68-69] In the pH region near the weak polyion pKa the degree of polyion chain ionization is varied by changing the pH of the polyion solution. The degree of ionization influences the molecular organization and determines the surface charge density of the adsorbed layer on which the appositively charged polyion electrostatically binds with each sequential deposition. While at high pH values relative to its pKa (between 5 and 6 depending on the ionic strength) the polyanion (PAA) becomes almost completely ionized it is more neutral as the pH value decreases relative to the pKa. Conversely, polycation (PAH) exhibit opposite ionization behavior. As the pH value decreases relative to its pKa value (pKa is between 8 and 9 depending on the ionic strength) the chains approaches to their full ionization.

The influence of the assembly pH on the thickness and molecular structure of the PAA/PAH multilayer films was characterized in the ph range between 2.5 and 9 by Rubner and coworkers.[68] By controlling the assembly pH the PAA/PAH bilayer thickness can be manipulated in the range between 1 nm to 12 nm.

At pH 2.5 the degree of PAA ionization is about 30% and increases with the increasing pH to its full ionization at pH 6, while the PAH chains remain fully ionized in this entire pH range.

Due to the increase in the charge density of PAA chains with increasing pH to 4.5, the incremental thickness of PAA layer is decreased due to flatter molecular organization of more highly charged PAA chains, whereas the thickness of PAH is increased. The increase in the charge density of the adsorbed PAA layer due to neutralization of the surface results in increased layer thickness of PAH.

As the pH value is increased beyond the value of 4.5 the incremental thicknesses of the adsorbed PAA and PAH layers increases abruptly to 4.5 nm and 8 nm per layer, respectively. In this pH range the PAA exhibit nearly full ionization while PAH are fully ionized and as a result alternating deposition yield unusually thick bilayers, whereas layer thickness in this range scales approximately as thickness of the layer ~ $M^{0.3.}$ By approaching the pH range where both polyanion and polycation are fully ionized the polyion chains exhibit flat molecular conformation that lead to the extremely thin multilayer films (0.6 nm to 1 nm per PAA/PAH bilayer) of interpenetrated polyion chains similar like in the assembly of strong polyelectrolytes.

In the assembly of weak polyions, the thickness increment per bilayer depends primarily on the relative charge density of the adsorbing and previously adsorbed layer in the entire pH range of polyion assembly. The charge density of the adsorbed polyion layer determines the amount of the polyelectrolyte that should adsorbed in order to neutralize the surface charge. The adsorbed layer hence establishes the electrostatic barrier that hinders further adsorption and therefore determines the thickness of the polyion bilayer of the multilayer film. Since the changes in the assembly pH affect the molecular conformational arrangement of polyion chains it consequently also affect the surface roughness of the assembled multilayer films. Flatter molecular conformation of weak polyion chains in the assembly pH region where full ionization is established exhibit very low surface roughness, less that 1 nm, which is comparable to the assembly of two fully charged polyions with no added salt in the multilayer formation.[65] However the surface roughness increases significantly, when the films are fabricated in the pH range that induces loopy conformational arrangement of the polyion chains. In the assembly of the PAA/PAH the surface properties of the multilayer film have been strongly controlled by the outermost adsorbed layer.[68-69]

Although the polyelectrolytes are adsorbed sequentially in LbL assembly, the internal structure of the assembled multilayer can be highly penetrated. Advancing contact angle measurements and methylene blue absorption studies suggest that a layer thickness play an important role in layer interpenetration. A greater penetration of thicker layer into the thinner layers was observed.

By controlling the thickness of the individual layer water contact angle can alternate between 10° and 40° when the outher-most layer alternates between PAA and PAH, respectively.[47] Thus, by varying the assembly pH it is possible to control the surface properties of the weak polyion multilayer films.

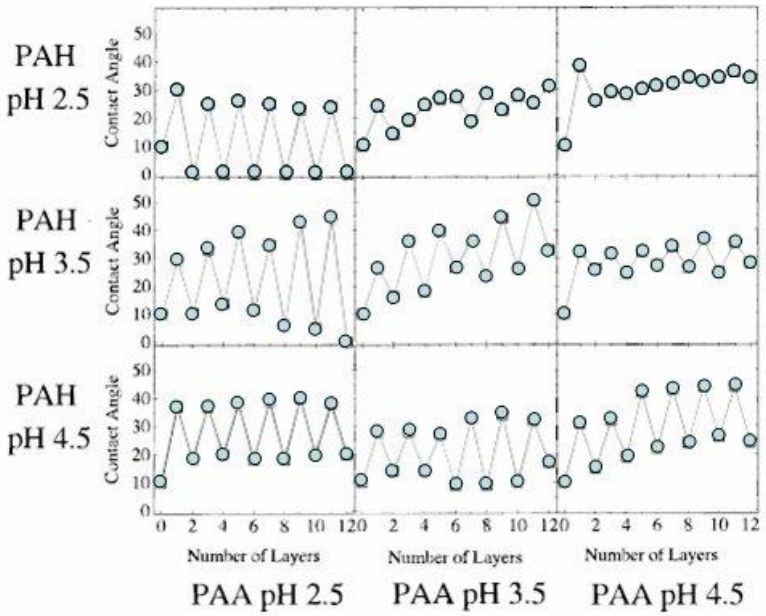

Figure 11. *Contact angles measured from films containing a different number of adsorbed layers of PAH/PAA as a function of variations in the pH of the polyion dipping solutions. Even numbers represent films with PAA as the outermost layer whereas odd number films have PAH as the outermost layer.*[47]

The extend of the layer interpenetration has been characterized by methylene absorption studies based on the fact that the amount of the methylene blue adsorbed on the surface layer is directly related to the availability of non ionized carboxylic groups within the surface layer. Based on the infrared spectroscopy measurements obtained from a film fabricated with a PAH and PAA about 30% dissociation of carboxylic groups is obtained at the assembly pH 2.5 which gradually increases with the increasing pH until full ionization is exhibited at the

pH 5.5. The results are consistent with the contact angle measurements and establish the layer interpenetration on the order of individual layer thickness.[69]

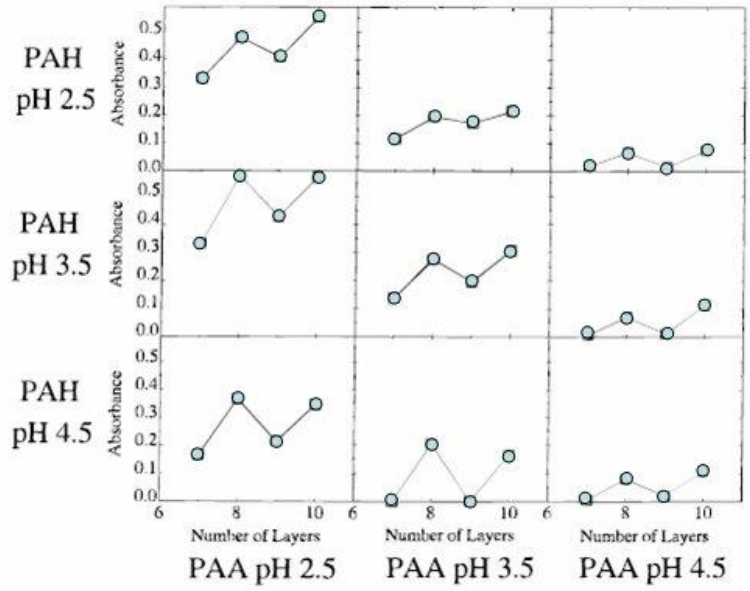

Figure 12. *Methylene blue absorption (measured at 600 nm)of films containing a different number of adsorbed layers of PAH/PAA as a function of variations in the pH of the polyion dipping solutions. Even numbers represent films with PAA as the outermost layer whereas odd number films have PAH as the outermost layer.*[69]

In the assembly of PAA and PAH, at pH 2.5 PAA layer present larger contribution to the total bilayer thickness. As the assembly pH is increased to 3.5 the thickness of the PAH layer prevails over the PAA thickness. With the thinnest layer as the surface layer, a large extent of underlying thickest layers penetrates into the outermost layer. When the thickest layer is the outermost layer, the surface properties are dominated by the outermost layer, whereas by increasing thickness of the underlying layers more chain segments penetrate into the surface layer. In the assembly pH regime where both adsorbed layers are thin, a high level of interpenetration is obtained regardless the type of outer-most layer. For intermediate thickness combinations, interpenetration is also obtained in both surface layers, while the amount of interpenetrated segments is determined by the relative thicknesses of the two layers.[68]

The LbL processing of weak polyelectrolytes has been shown to be a versatile approach for the formation of multilayer films. Due to their high sensitivity to the assembly pH, by controlling the adsorption condition the film structure, thickness and availability of non-ionized groups in multilayer film is systematically varied. Furthermore, the ability to control the chemical functionality of polyelectrolytes, and degree of ionization gives the opportunity to assemble inorganic species within the polyion multilayer film and enable further chemistry by utilization of polyelectrolyte multilayer films as nanoreactor for various inorganic syntheses.

1.4.1 Inorganic nanoparticle- polyelectrolyte multilayer composite films

The LbL of polyelectrolyte self assembly process have been utilized for the formation of nanocomposite thin films. The ability to combine polyions with other charged species lead to the formation of new ordered systems, dimensional polymer structures and variety organic and organic-inorganic hybrid composite thin films. In order to obtain ordered and homogeneous nanoparticulate films with controlled thickness the LbL technique has been employed to assemble a variety of inorganic shapes (nanoparticles, nanowires and nanosheets) of semiconductor, metallic and magnetic nanocrystals.[70-72]

1.4.1.1 Layer by Layer assembly of polyelectrolytes and inorganic nanoparticles

The ability of simultaneous introduction of various nano-components with high loading, control over the layer composition and film thickness control in nanometer scale yield novel inorganic-organic nanocomposite material with controlled interfaces. The common feature of the assembly of preformed inorganic nanocrystals into the polyelectrolyte multilayer films is that the nanoparticles with appropriate surface modification in stabilized media must be prepared before film formation. Due to higher charged polyion chains mostly strong polyelectrolyte pairs were used in the polyion –nanocrystal structure assembly.

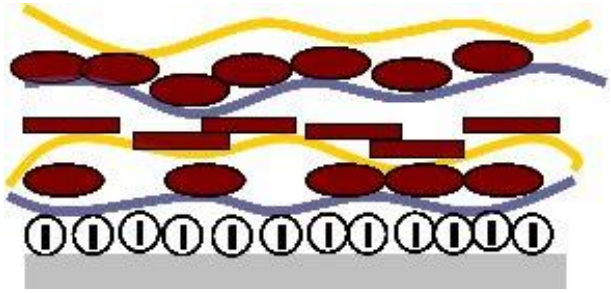

Figure 13. *Layer by layer self assembly of nanostructures and polyelectrolytes.*

Metal oxide colloids of silica (SiO_2)[73] and titania (TiO_2)[74] at high pH were assembled with PDDA and PEI whereas at low pH their assembly was performed with the PSS. In contrast to metal oxide nanoparticles, the charged surface of metallic and semiconductor nanoparticles is created with surface capping with appropriate stabilizing or coordinating agents. Negatively charged cadmium (CdS)[75] and lead sulfide (PbS)[76] nanoparticles at high pH synthesized in the presence of thiolactic acid were assembled with PDDA, whereas gold (Au)[77] nanoparticles synthesized by citrate reduction were assembled with PAH. Although control over the thickness is obtained by varying the deposition cycles, it is difficult to manipulate the size and concentration of the nanocrystals in the composite film during and after the assembly.

To overcome the draw backs of the layer-by-layer deposition method Strove and coworkers[78-80] developed a nanoreactor scheme, where pre-assembled polyelectrolyte multilayers (PEMs) composed of strong polyelectrolytes are used as a template for the in-situ synthesis of the inorganic nanoparticles.

1.4.1.2 Self assembled polyelectrolyte multilayer nanoreactors for the inorganic synthesis

The in-situ synthetic methodology of preassembled polyelectrolyte multilayer as a nanoreactor for the inorganic synthesis enables the selective nanoparticle synthesis.

By changing the pH value (weak polyions) and the ionic strength (strong polyions) of the polyion solution the free groups are present within the multilayer film which enable metal ion binding for the subsequent in-situ nanoparticle synthesis.

Various chemical reactions and the physical treatments of the incorporated ions lead to the formation of diverse nano-crystallites (semiconductor, metal) with different functionalities and properties. With the in-situ synthesis of the inorganic nanoparticles the surrounding polymer chains limit the particle aggregation, thus yielding uniform, small particles. Moreover, by repeating the reaction cycle, the size and shape of the crystallites in the multilayer film can be controlled. The main drawback with the use of strong polyions is the absence of the ability to control the volume density and size distribution of the inorganic species within the polyelectrolyte multilayers (PEMs). It has been demonstrated that the porous supramolecular structure of the PEMs enables the penetration of the metallic ions from an aqueous solution into the multilayer film for subsequent nanoreactor chemistry.[81-83]

Multilayers of strong polyelectrolytes of PSS and PDDA or PAH were used as a templates to prepare $Co(OH)_2$,[83] Iron oxyhydroxide (FeOOH)[82] and lead sulfide (PbS)[81] /PEM nanostructures. In the strong polyion matrix assembly, due to the full ionization of the PSS sulfonate groups all the acid groups of the strong polyion are electrostatically coupled to the cationic groups of the surrounding layers. Since there are no available active sites in the assembly for the controlled metal-ion binding it is unclear where the metal cation could bind. The ions binding on non-paired charged groups of the surface layers would result in the formation of nanoclusters on the surface of the polyion film. Within the polyion film, the nucleation of the inorganic particles could only be initiated by the adsorption of ions within the voids of the PEM film, which results in a non-spatially selective growth of the inorganic particles.[83] Due to the flatter molecular organization of the strong polyion chains that is induced by the fully ionized charged groups of the polyions, voids with a large size distribution are obtained in the PEM. The specific constrained geometry of the void spaces in the PEM induces preferential growth of larger particles of elongated morphology. As a result, inorganic particles with uncontrolled morphologies and large size dispersion are normally formed in strong polyion assemblies. Increasing the number of the ion exchange and reduction steps lead to the formation of larger microcrystallites.[83]

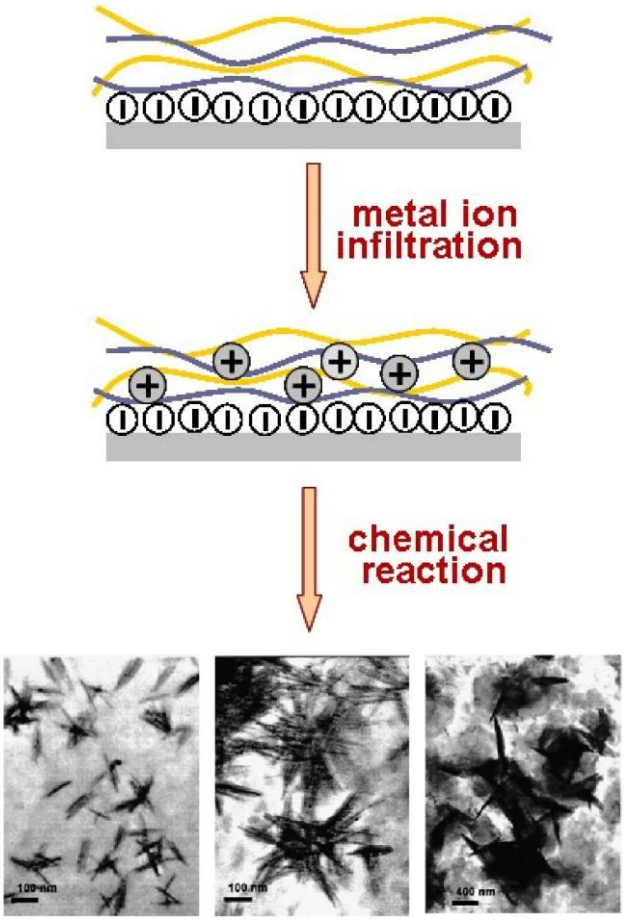

Figure 14. *The scheme of the in-situ strong polyelectrolyte matrix for the inorganic nanoparticle synthesis. TEM micrographs of 3.5 layer pairs of PDADMAC-PSS films at different stages of the $CoCl_2$ absorption-hydrolysis process in a nitrogen-enriched microenvironment with 2, 4, and 8 cycles.*[83]

Recently, Rubner and coworkers[84-85] extended this nanoreactor scheme to multilayer films composed of weak polyelctrolytes. In the assembly of weak polyacids, the number of non-ionized carboxylic groups in the multilayer film can be controlled by varying the pH value of the polyelectrolyte (PE) dipping solutions. Metallic cations are able to bind to the free carboxylic groups by ion exchange with the acid protons, where with the post-binding reaction of the incorporated metal cations the inorganic nanoparticles are formed.

Silver (Ag)[84] and lead sulfide (PbS)[85] nanoparticles were synthesized in PEMs assembled from weak polyacids. Both Ag^+ and Pb^{2+} ions are known to bind with the carboxylic acid groups, and the post-binding reaction of the incorporated ions was performed in a gas atmosphere: $H_2(g)$ for the reduction of the silver cations and H_2S (g) for the sulfidation of the lead cations.

However, during the synthesis, elevated temperatures and long reaction times were needed in order to complete the reduction and sulfidation processes. Comparing to the strong polyelectrolyte matrix, free acid groups in the weak polyion template enable larger extent of the metal ions incorporated to the matrix which result in larger loading of inorganic nanoparticles in the composite films after the reaction. It was shown that within the weak polyion matrix the control over the concentration of the metallic (Ag) and semiconducting (PbS) nanoparticles is possible by manipulating the multilayer processing conditions.

The LbL technique is not exclusively restricted to planar substrates but can also be effectively applied to highly curved surface such as micro- and nanospheres. Furthermore, colloidal templating has been demonstrated as an effective approach in the fabrication of various uniform composite core-shell particles and hollow spheres.[86-87] The combination of LbL self assembly and in-situ sol gel reaction could provide a possibility for the preparation of tailored, composite colloids with desirable functionality. Metal oxide precursors that are extremely sensitive to water readily hydrolyze and condense upon contact with water. Since the LbL templating is performed from the aqueous solution of polyelectrolytes as formed multilayer templates incorporates water where with controlled precipitation of the metal oxide precursor is possible by optimization of the reaction conditions.

Previously, polyelectrolyte multilayer coated spheres have been used as the templates for sol-gel reactions in the fabrication of composite, core-shell colloids and hollow spheres. Since the thickness of the PEM can be controlled on the nanometer scale by the number of adsorbed PE layers, the PEM template-assisted in-situ sol-gel reaction makes possible the formation of core-shell colloids with precise control over the shell thickness.[86] Wang et al. reported on the synthesis of polystyrene spheres $LiNbO_3$ core-shell particles and resulting hollow $LiNbO_3$ spheres after core removal. Later, the mechanism of coated colloidal spheres was extended for the synthesis of inorganic and inorganic/organic macroporous materials where the PEM-coated colloids were first assembled into macroscopic close-packed structures and then used as templates for the in-situ sol-gel reaction. The ability to control the porosity of the macroporous structure depend on the number of polyelectrolyte layers, concentration of the precursor infiltration process and demand a single precursor for the modified sol gel reaction.

The Ti-alkoxide solution was infiltrated in strong polyelectrolyte multilayers coated polystyrene colloids. During the precursor infiltration, both the interstitial

voids between coated colloids and the PE layers are filled. Various number of polyelectrolyte layers have been deposited to modulate the pore diameter and pore center to center distance. By removal of the PEM template and the organic core using a calcination process, macroporous inorganic material was obtained, where the control of the PEM shell-template thickness enabled tailoring of the pore morphology and control over the pore-wall thickness.[87]

2 Aim of the work

For the envisioned application of inorganic nanoparticles, various methods of the polymer based particle assembly in the form of thin film have been established. Among others, the Layer-by Layer self assembly technique has often been used to process the inorganic dispersions into high quality composite thin films with controlled nanoscale thickness. Moreover, due to its ability of precise thickness control the layer by layer polyelectrolyte self assembled nanostructured film has been applied as a matrix for the in-situ inorganic nanoparticle synthesis.

For the most part, polyion matrixes formed of strong polyions have been utilized as a template for the subsequent nanoreactor chemistry. With the nanoreactor chemistry approach obtaining the control over the size, size distribution, morphology and crystallinity of the inorganic species is crucial for the desired properties of the inorganic-organic composite materials. Due to the lack of ability to control the molecular arrangement of the strong polyions within the multilayer matrix and due to the absence of available binding sites for the metal ion incorporation, uncontrolled growth of the inorganic species within the multilayer matrix is obtained that often results in the formation of inorganic clusters of uncontrolled morphologies and large size distributions. On the other hand, better control over the characteristics of the inorganic species can be obtained with the in-situ synthesis approach in polyion matrix assembled of weak polyions. The architectural parameters of the weak polyion matrix can be controlled via polyion solution conditions and hence, weak polyion multilayer can be extremely versatile matrices for synthesizing inorganic nanoparticles.

The thesis focuses on weak polyelectrolyte multilayer films formed by the Layer-by –Layer self assembly technique as soft templates for the inorganic (metallic - Ag and semiconducting - ZnS) nanoparticle wet chemical synthesis. Furthermore, weak polyion multilayer was also utilized as a template for the nanocrystalline TiO_2 film fabrication.

The goals of this thesis were

- To develop the weak polyion multilayers as nanostructured templates for the inorganic-organic composite formation with in-situ wet chemical synthesis of inorganics
- To elucidate the influence of the internal molecular structure of the multilayer templates and the polyion assembly pH on the size, morphology and volume fraction of inorganic species (Ag, ZnS) grown within the weak polyion matrix
- To evaluate the growth characteristics of the metallic Ag and semiconducting ZnS nanoparticles formed within the weak multilayer templates by a wet chemical process
- To extend the nanoreactor scheme for the synthesis of doped semiconducting nanoparticles
- To establish the weak polyion films as a template for the in-situ sol gel reaction for the TiO_2 nanocrystalline ceramic film fabrication. Evaluation of the ability for the polyion template to control the thickness and morphology of the TiO_2 crystalline ceramic film.
- To control the optical properties of template assisted formed Ag/PEM and ZnS/PEM and $Zn_{1-x}Mn_xS$/PEM inorganic-organic nanocomposite films and inorganic TiO_2 crystalline films.

3 Materials and methods

3.1 Polyelectrolyte multilayer film assembly

The positively charged polyelectrolyte PAH-Mw=70000 (Sigma Aldrich) and the negatively charged polyelectrolyte PAA-Mw=90000 (Polysciences) were used for the fabrication of the multilayer film. Deionized water (ρ›18MΩcm) with a pH value of approximately 5.5 was used in all the aqueous solutions and rinsing procedures. Polyelectrolyte dipping solutions PAH and PAA were adjusted to the desired pH (±0.1) using either 1M HCl or 1M NaOH.

PEMs of PAH and PAA were assembled on polystyrene (PS) tissue-culture substrates (corona-treated Nalge Nunc International) and quartz wafers (Si-Mat) by alternating dipping of the substrate into oppositivelly charged solutions of polyelectrolytes. Prior to the PEMs' assembly, the quartz slides were cleaned in Piranha solution (H_2O_2/H_2SO_4=30:70 v/v) and subsequently washed thoroughly in deionized water. The Piranha-solution treatment removes all traces of organic materials sticking to the quartz surface in addition to making the surface hydrophilic (negatively charged), as described in detail elsewhere.[88] The PS substrates were used as received.

The polyelectrolyte multilayers (PEMs) were formed by first immersing the substrates into the PAH solution (10^{-2} M by repeat unit) for 10 min, followed by two 1-min immersions into water, as rinsing steps. The substrates were then immersed into the PAA solution (10^{-2} M) for 10 min, followed by identical rinsing steps. The adsorption and rinsing steps were repeated until the desired number of layers in the polyelectrolyte multilayer was obtained.

To determine the thickness of the PEMs, 5, 10 and 15 bilayered films were assembled at various pH values, where one bilayer of the PEMs is defined as a single adsorption of polycation (PAH) followed by an adsorption of polyanion (PAA). After the assembly, the PEMs were dried in a vacuum at 80°C for one hour and stored under ambient conditions.

The molecular structure of the PEM films was assessed with an AFM (Veeco DI 3100, Nanoscope 4) in tapping mode. The film thicknesses were measured using profilometry (Form Talysurf Series 2, Taylor-Hobson Ltd.). The films assembled on quartz substrates were scratched with a razor blade to form lines. By profiling the scored line, the depth of the scratch was measured. An average value of five measurements was chosen to represent the thickness of the film.

Optical spectra of the polyelectrolyte multilayer films on quartz substrates were measured using a UV-vis transmission spectrophotometer (Hewlett-Packard - 8453).

3.2 In-situ synthesis of Ag nanoparticles in (PAH / PAA)$_n$ multilayer film

For the in-situ Ag nanoparticle synthesis, PEMs with 7.5 bilayers of PAH/PAA, assembled at pH values of 2.5, 3, and 3.5, were immersed in an aqueous solution of silver acetate Ag(ac) (Sigma Aldrich) (5mM) at a nominally neutral pH for 12 hours, where the acid protons of the PAA are exchanged for silver cations.[89]
After the ion exchange the films were washed in pure water and dried in vacuum. The subsequent reduction of the Ag(I)-containing films with the 5mM $NaBH_4$ aqueous solution for 1 hour forms Ag(0) nanoparticles and regenerates the carboxylic acid groups. The volume fraction of silver (Ag) in the PEMs is increased by repeating the ion exchange and reduction process.

Transmission electron microscopy (TEM) imaging was performed on multilayer-film cross-section cuts using a ultramicrotome (Reichart Ultracut S) with a 45° diamond knife (Diatome) at room temperature. The cut sections, approximately 40-nm thick, were immediately picked up with Cu grids. The TEM was performed on carbon-sputtered samples using a 200-kV (JEM-2010F, Jeol Inc.). Based on the TEM images, the diameters of 200 particles for each sample were measured in order to determine their average size distribution.

For the high-resolution TEM and electron-diffraction studies the Ag nanoparticles were ultrasonically separated from the polymer matrix.

The film thicknesses were measured using profilometry (Form Talysurf Series 2, Taylor-Hobson Ltd.) as described for the polyion multilayer films.
The area fraction of the Ag nanoparticles in the PEM film was calculated from the cross-sectional TEM images.

Using stereology,[90] 3D-sample information can be obtained from measurements made on 2D microscope sections, where the extrapolation from the sample to the 3-D material depends on the assumption that the material is homogeneous.

Optical spectra of the composite films on quartz substrates were measured using a UV-vis transmission spectrophotometer (Hewlett-Packard -8453).

The in-situ synthesis process of Ag nanoparticle synthesis in PEM is shown schematically in Figure 15.

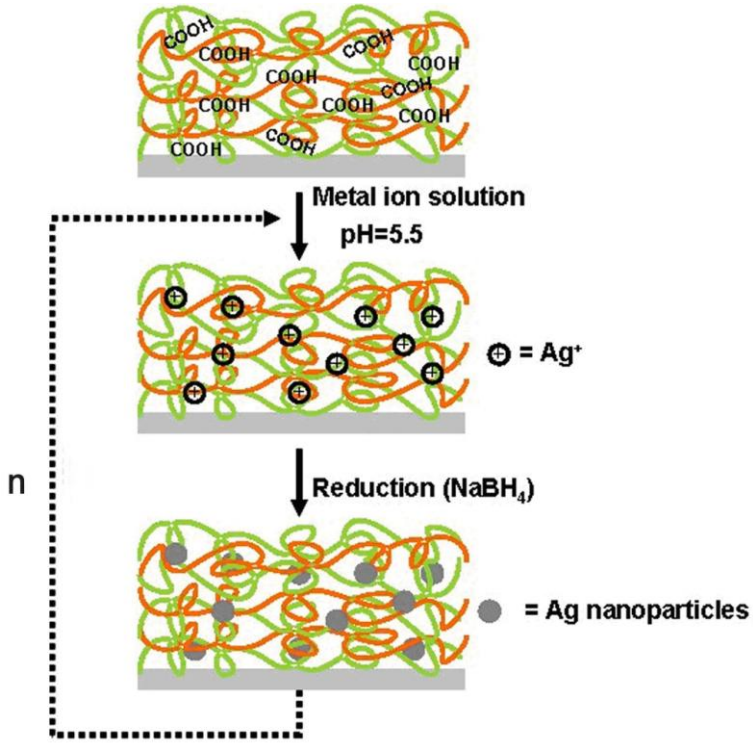

Figure 15. *Nanoreactor scheme for the in-situ synthesis of silver (Ag) nanoparticles in PEMs.*

3.3 In-situ synthesis of ZnS and Mn-doped ZnS nanoparticles in (PAH / PAA)$_n$ multilayer film

Zinc acetate ($Zn(Ac)_2$) and manganese acetate ($Mn(Ac)_2$) (Sigma Aldrich) were used as the sources of Zn and Mn for the nanoparticle synthesis.

The PEMs of PAH and PAA were assembled on polystyrene (PS) tissue-culture substrates (corona-treated Nalge Nunc International) and quartz wafers (Si-Mat) using a dipping procedure. The PS substrates were used as-received, whereas the PAH and PAA dipping solutions were adjusted to the desired pH (±0.1) using either 1-M HCl or 1-M NaOH.

The ZnS nanoparticles were synthesized in-situ in a 7.5 PAH/PAA bilayered polyion multilayer matrix fabricated by the LbL self-assembly of oppositely charged PAA and PAH weak polyions at pH values of 2.5 and 3.0, respectively. To increase the ion-binding efficiency in the polyion film, PEMs were first exposed to a 0.001-M NaCl solution, which converts the carboxylic acid groups to the sodium carboxylate form.[91] For the in-situ ZnS nanoparticle synthesis, PEMs with 7.5 bilayers of PAH/PAA, assembled at pH values of 2.5 and 3.0, were immersed in an aqueous solution of Zn-acetate (0.01 M) at the pH value of 5.5 for 24 hours. After the ion exchange the films were rinsed in deionized water and dried in vacuum. The subsequent precipitation of the ZnS nanoparticles in the PEM was performed by exposing the Zn-ion-containing films to the 0.02-M Na_2S aqueous solution for 1 hour. The number of reaction cycles (n) in the ZnS nanoparticle synthesis, composed of the metal cation binding to the ionized carboxylic groups of the PAA and subsequent sulfidation of the incorporated Zn^{2+} ions, was varied from n=1 to n=3.

For the Mn-doped ZnS nanoparticle synthesis, the multilayer film was first exposed to the mixture of the Zn ion (0.01 M) and the Mn ion (0.001 M, 0.0015M, 0.002M and 0.003 M) solutions followed by a subsequent sulfidation with Na_2S.

The film thicknesses were measured using profilometry (Form Talysurf Series 2, Taylor-Hobson Ltd.). The volume fractions of the ZnS nanoparticles in the PEM matrixes were evaluated from the increase in the film thickness after ZnS precipitation, assuming a constant film area.

The surface morphology of the ZnS/PEM composite film was assessed with an AFM (Veeco DI 3100, Nanoscope 4) in tapping mode. For the transmission electron microscopy (TEM) observations, the polyion films with ZnS nanoparticles on polystyrene (PS) tissue-culture substrates were cut using an ultramicrotome (Reichart Ultracut S, Leica) with a 45° diamond knife (Diatome). Approximately 50-nm-thick sample cross-sections were then deposited onto the lacey carbon TEM grid. The TEM studies were performed using a 200-kV TEM (JEM-2100 HR, Jeol Inc.) equipped with a high-resolution objective-lens pole-piece having a point-to-point resolution of 0.19 nm, which is sufficient to resolve the lattice images of the ZnS in the [110] and [112] zone axes.

For the high-resolution TEM and electron-diffraction studies the ZnS nanoparticles were ultrasonically separated from the polymer matrix. Both the selected-area electron diffraction (SAED) on multiple ZnS particles and the electron micro-diffraction on oriented single ZnS particles were used to determine the structural characteristics of the ZnS nanoparticles formed in the PEM matrix. From

the TEM images, the diameters of ~100 particles for each sample were measured in order to determine the average particle size.

The optical spectra of the composite films deposited on quartz substrates were measured using a UV-vis transmission spectrophotometer (Hewlett-Packard - 8453), while the emission properties of the composite films were measured with a fluorescence spectroscope (Hitachi, F-4500 FL spectrophotometer). The room-temperature photoluminescence emission spectra of the ZnS composite films were recorded with an excitation wavelength of 270 nm under identical conditions.

The scheme of in-situ synthesis approach for semiconducting (ZnS) and doped ZnS nanoparticles in PEM nanoreactor is shown in Figure 16.

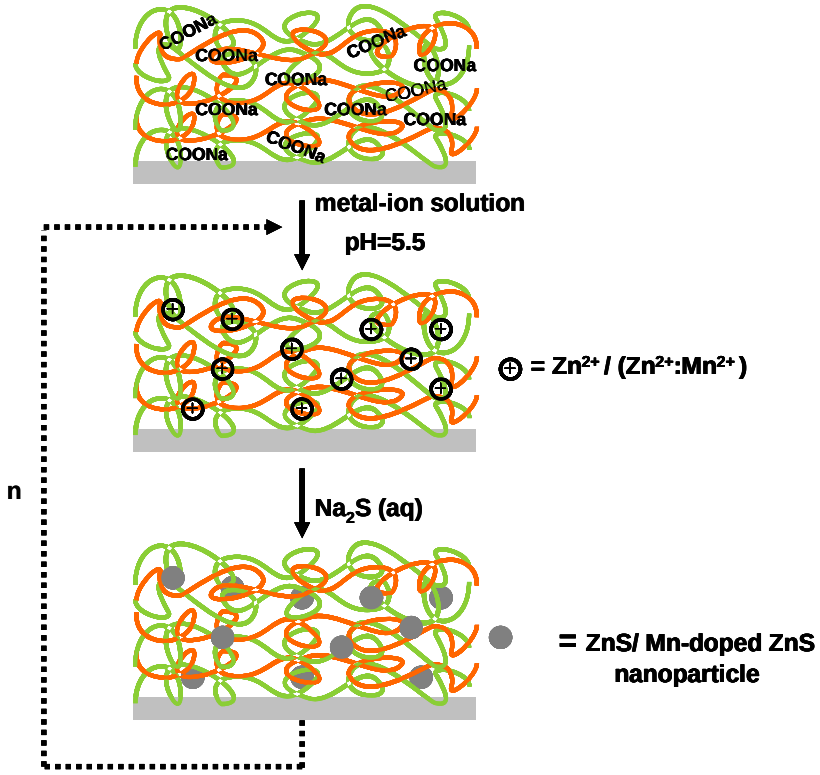

Figure 16. *Nanoreactor scheme for the in-situ synthesis of ZnS and Mn-doped ZnS nanoparticles in PEMs.*

3.4 TiO_2 thin film fabrication by an in-situ sol-gel method in $(PAH / PAA)_n$ multilayer film

Aqueous solution of the positively charged polyelectrolyte (PAH, Mw=70000-Sigma Aldrich) and the negatively charged polyelectrolyte (PAA, Mw=90000-Polysciences) were used for the fabrication of the multilayer film. Titanium iso-propoxide (99.99%-Sigma Aldrich) and iso-propanol (99.99 %) were used for the sol-gel precursor solution. Deionized water (ρ›18MΩcm) with a pH value of approximately 5.5 was used in all the aqueous solutions and rinsing procedures. The PEMs were assembled on Silicon and Quartz substrates (Si-Mat) using a dipping procedure.

The organic template for the TiO_2 thin-film fabrication in the form of a polyelectrolyte multilayer (PEM) was formed using the LbL self-assembly technique as described previously.

The pH-value of 3.0 was used in all aqueous solutions in the PEM assembly. In order to control the final thickness of the TiO_2 film, PEM templates with 7, 12 and 17 PE bilayers were formed, where one bilayer of the PEM is defined as a single adsorption of polycation (PAH) followed by an adsorption of polyanion (PAA).

For the fabrication of the TiO_2 film, an in-situ sol-gel reaction was performed in the PEM film. The sol-gel precursor solution was prepared using titanium iso-propoxide (Sigma-Aldrich) in iso-propanol, in the volume ratio 1:10. Prior to the exposure of the PEM template to the sol-gel precursor solution, the templates were dried under ambient conditions for 0.5h yielding a formation of a water gradient in the PEM template.[45]

The templates were then exposed to the anhydrous titanium iso-propoxide precursor solution in an inert atmosphere for 15 min, causing it to infiltrate the multilayer film. During the interaction of the precursor with the water absorbed within the multilayer template, the hydrolysis and condensation of the precursor occur, causing its gelation and the formation of a thin, inorganic/organic hybrid coating with a defined thickness. To achieve complete infiltration of the multilayer template the process of infiltration/solidification of the precursor was repeated five times, with washing in anhydrous iso-propanol between each step. Finally, the samples were dried under ambient conditions.

The crystalline TiO_2 film was obtained by subsequent removal of the organic template; this involved calcination of the samples at 500°C (2°C/min) for 1h in air.

The film thicknesses were measured using profilometry (Form Talysurf Series 2, Taylor-Hobson Ltd.). The shrinkage of the film after the annealing process was calculated from the thickness measurements.

The surface morphology of the TiO_2 films on the Silicon substrates was examined using a field-emission scanning electron microscope (FE-SEM) and an atomic force microscope (AFM – Veeco DI 3100, Nanoscope 4) in the tapping mode. The crystalline phase of the TiO_2 film was determined with an X-ray diffractometer (XRD).The spectroscopic analyses of the TiO_2 films on Quartz substrates were performed using a UV-vis transmission spectrophotometer (Hewlett-Packard 8453).

The scheme of in-situ sol-gel reaction for the nanocrystalline TiO_2 thin film fabrication is shown in Figure 17.

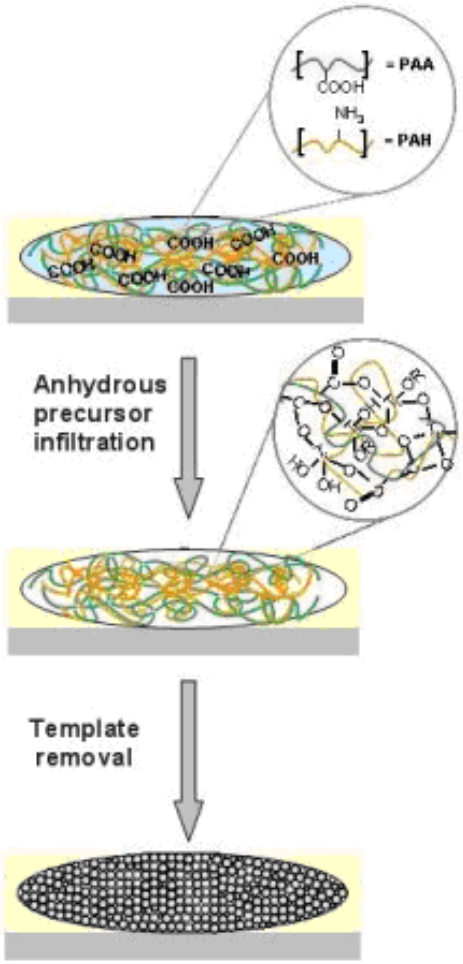

Figure 17*. The illustration scheme of the in-situ sol gel reaction in PEMs for the nanocrystalline TiO_2 film synthesis.*

4 Results and discussion

4.1 Polyelectrolyte multilayer matrix

The pH of the PAH and PAA dipping solutions and the number of the adsorbed polyion layers were systematically varied and in order to determine how these parameters influence the molecular organization and multilayer thickness.

Figure 18 show the UV-vis absorbance of multilayer films with alternating PAH and PAA layers assembly at pH value of 2.5.

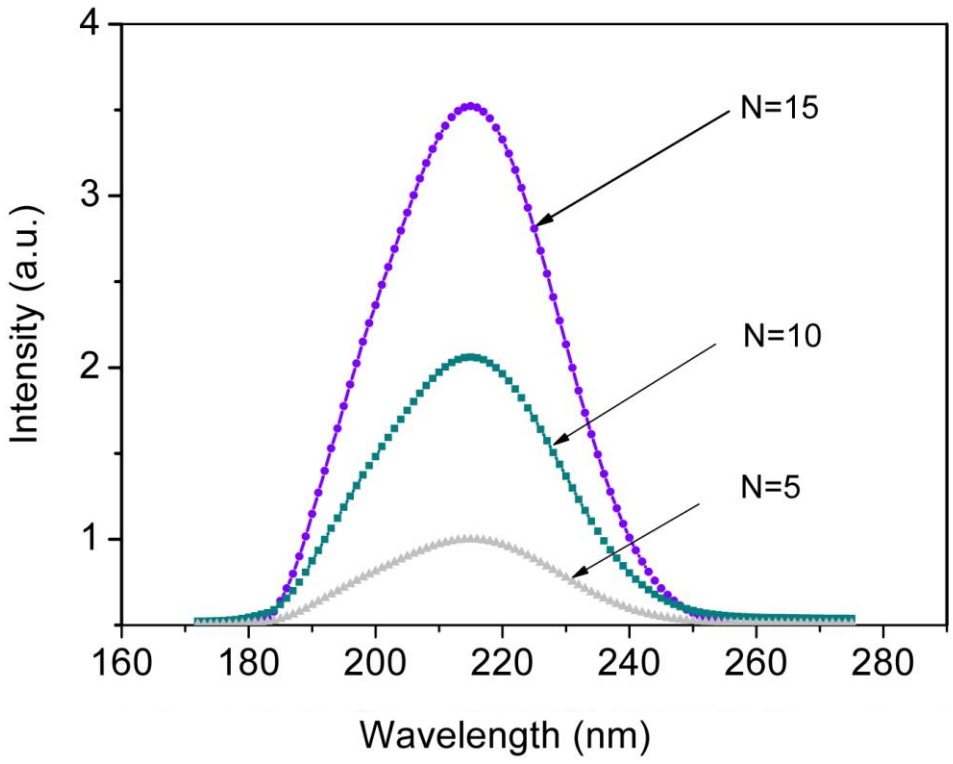

Figure 18. *The UV-vis absorbance spectrum of (PAH/PAA)n multilayer film.*

While the absorption maximum of PAH chains is at wavelength of 190 nm, the absorption at 216 nm is assigned to be the contribution from the adsorbed PAA chains. The intensity of the absorption maxima of PAA is increased with increasing number of polyelectrolyte layers in the multilayer film (Figure 18). In the LbL deposition each sequential electrostatic adsorption of the appositively charged polyion layer yields multilayer film formation. Higher amount of the PAA polyion

chains incorporated in the multilayer film as the number of PAH/PAA bilayers (N) is increased at certain pH value results in the increased absorption intensity of the PAA chains at 216 nm.

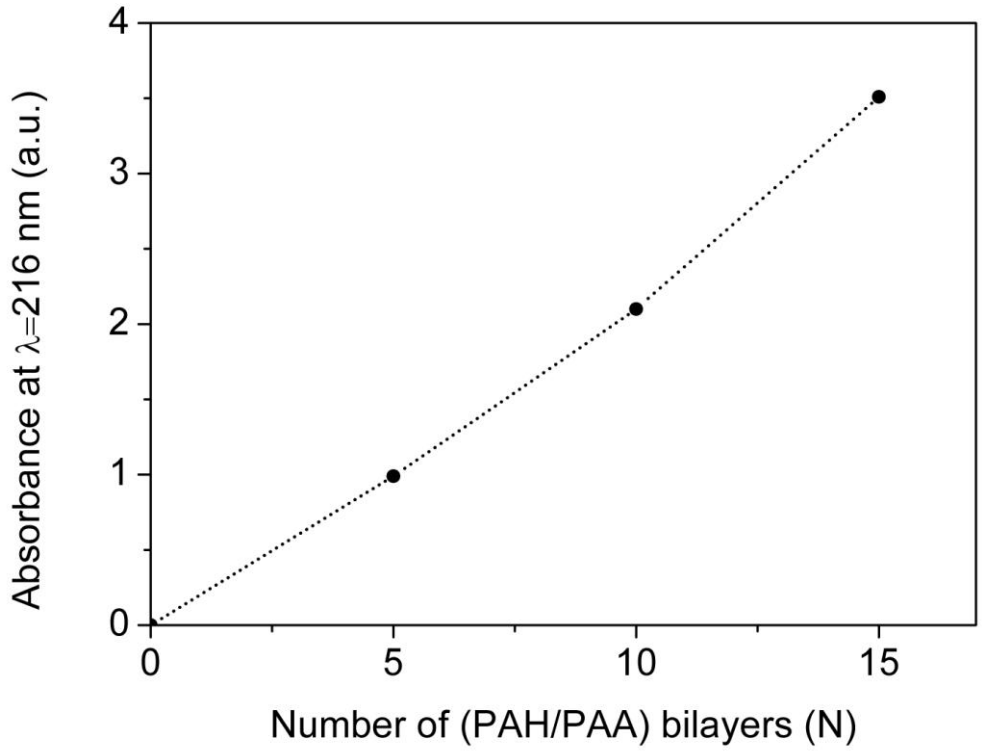

Figure 19. *The intensity of the PEM absorbance at 216 nm versus the number of PAH/PAA bilayers.*

At certain value of the assembly pH, an equal amount of each polyion is adsorbed in order to neutralize the appositive charge of the previously adsorbed layer due to constant charge density of the polyion chains. Since in each adsorption cycle an equal amount of the polyion chains is adsorbed an almost linear increase in the intensity of the absorption maxima is observed with the increasing number of assembled polyion layers (Figure 19).

The graph in Figure 20 shows how the multilayer film thickness varies depending on the number of bilayer building blocks (polycation plus polyanion) for PEMs assembled at pH values of 2.5, 3.0 and 3.5.

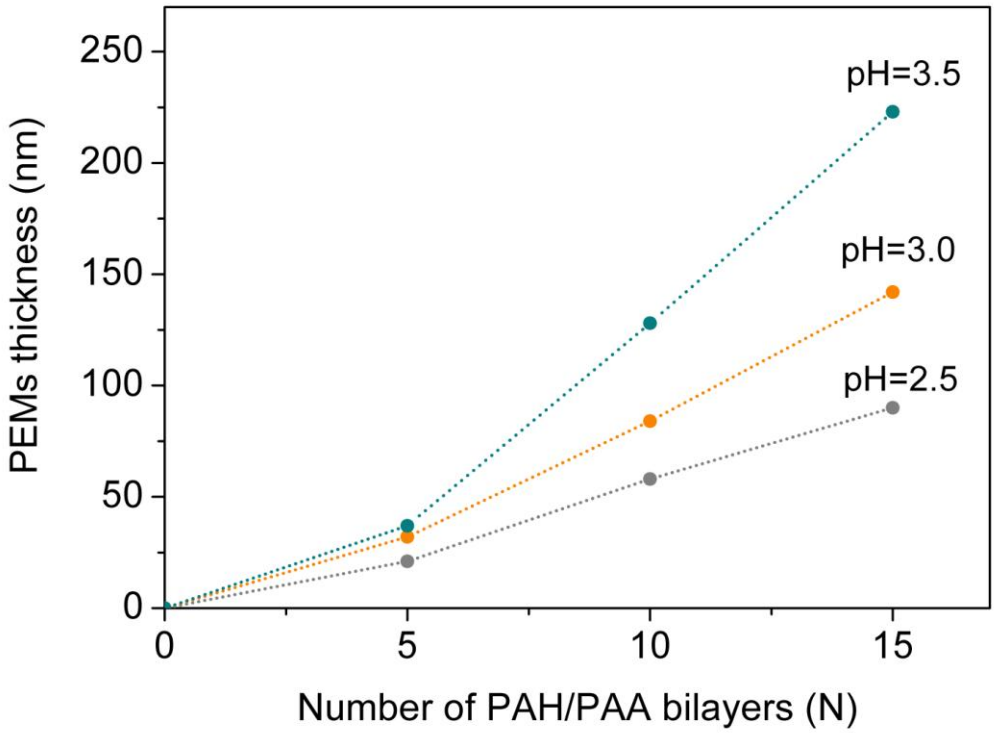

***Figure 20**. The multilayer film thickness versus the number of PAH/PAA bilayers in PEMs assembled at pH values of 2.5, 3.0 and 3.5 on silicon substrates.*

From Figure 20 it is clear that there is a significant influence of the pH value of the polyelectrolyte dipping solution on the PEM film's thickness. As the pH value of the PEMs' assembly is increased, thicker multilayer films are obtained. In addition, after five bilayers have been deposited there is a linear increase in the thickness of the PEMs assembled at all the pH values, whereas a different incremental thickness of the first five bilayers can be attributed to substrate effects.[88] From the slope of the lines, calculated from five bilayers and up, the average thickness per bilayer building block varies from 7 to 18 nm, as the pH value of the PE dipping solutions increases from 2.5 to 3.5. The average incremental thickness of the sequentially adsorbed PE layer is determined by the relative charge densities of the adsorbing and previously adsorbed polyelectrolyte.[42] Since the PAH polyelectrolyte chains are completely ionized across the entire pH range used for the PEMs' assembly, the larger incremental thickness of the PEM film with increasing pH value must be related to the change in the linear charge density of the PAA polyelectrolyte chains.

As the pH value is increased from 2.5 to 3.5 the PAA chains become more ionized, which increases the repulsion of their carboxylate groups and hence the organization of the PAA chains on the surface becomes flatter. As a result, the thickness of the PAA layer is decreased as the pH value is increased. On the other hand, more appositively charged PAH chains are needed to neutralize the higher surface charge of the previously adsorbed PAA layer and hence a larger incremental thickness of the PAH layer with the increasing pH value of the PEM assembly is obtained. Although the thickness of the adsorbed PAA layer decreases with the increasing pH value, the contribution of the PAH layer to the bilayer thickness is more pronounced and thus, a larger thickness of multilayer film is obtained as the pH increases from 2.5 to 3.5.

The evolution in the PEM surface characteristics of the 7.5 PAH/PAA bilayered films with the increasing pH value of the multilayer assembly is shown in Figure 21.

The root mean square roughness measured over an area of 1μm*1μm of PEM film assembled at pH 2.5, 3.0 and 3.5 is 1 nm, 1.9 nm and 3.2 nm, respectively. Since the molecular organization of the PE chains is controlled by the charge density of the polyelectrolyte chains, the final structure and surface characteristics of the PEMs also changes as the pH is varied.

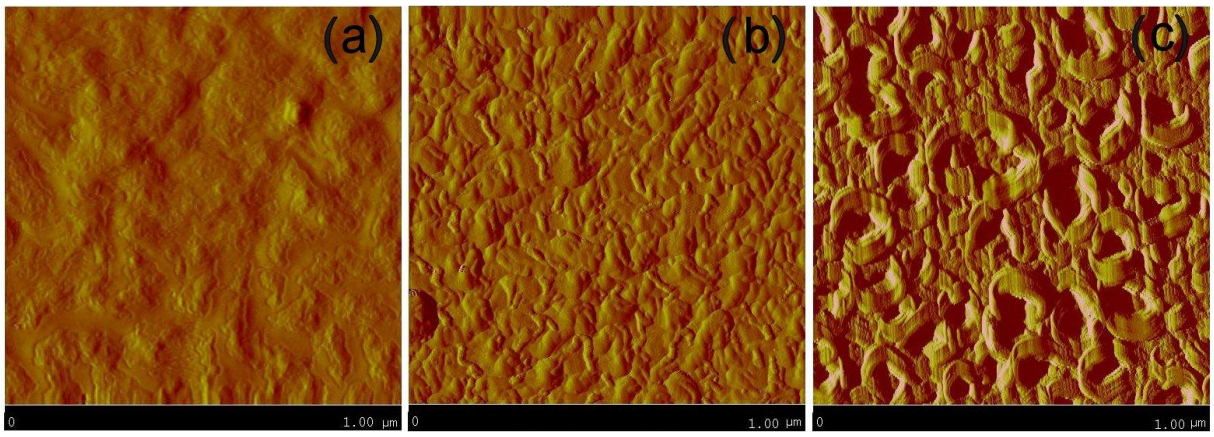

Figure 21. *AFM images of the of 7.5 bilayered polyelectrolyte films assembled at pH value of a) 2.5, b) 3.0 and c) 3.5.*

By increasing the pH value of the PEM assembly, flatter molecular arrangement of the PAA chains results in the formation of larger voids within the multilayer film. Hence more porous structure of the multilayer film is obtained as the pH value of

the polyion assembly is increased. Furthermore, due to larger ionization of the negatively charged polyion chains larger amount of appositively charged PAH is adsorbed in a subsequent layer. The simultaneous increase in the thickness of PAH and a decrease of PAA layer thickness with the increasing pH result in lower interpenetration of the underlying PAA layer into the outhermost PAH layer of the multilayer film. As a consequence, larger surface roughness is obtained with the as the assembly pH is increased from 2.5 to 3.5.

4.2 In-situ synthesis of metallic (Ag) nanoparticles in PEMs

To control the size and concentration of the in-situ synthesized Ag nanoparticles, PEMs with 7.5 bilayers of PAH/PAA assembled at pH values of 2.5, 3.0 and 3.5 were used to bind the silver cations (Ag+) for a subsequent nanoparticle synthesis. In all samples the ion exchange and the reduction of the incorporated ions were performed in solutions at pH 5.5.

Figure 22 shows a cross-sectional STEM-HAADF image of such a synthesized composite film.

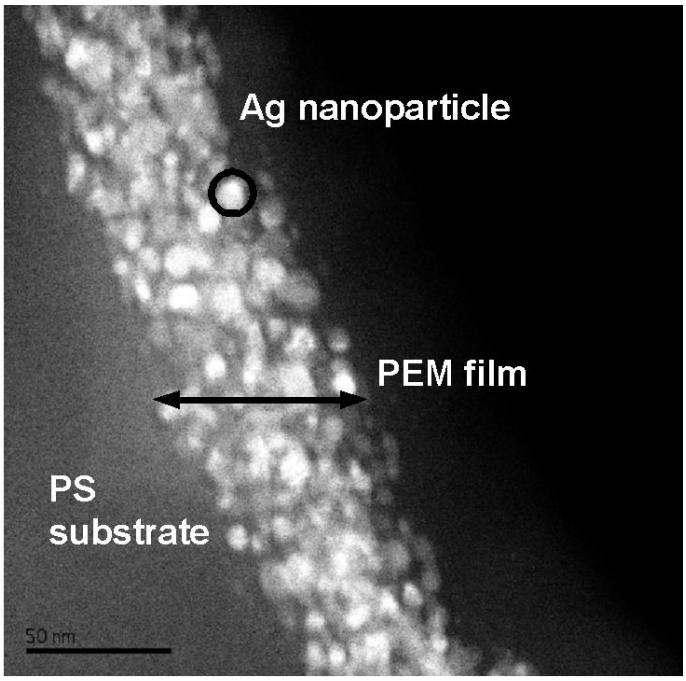

Figure 22. *STEM-HAADF image of Ag nanoparticles in PEMs assembled at pH 2.5 after three reaction cycles.*

4.2.1 Controlling metal (Ag) concentration and nanoparticle size by varying PEM assembly pH

In Figure 23, cross-sectional TEM images show that the in-situ synthesized spherical Ag nanoparticles in the PEMs, assembled under different pH conditions, are randomly and homogeneously distributed throughout the PEM film.

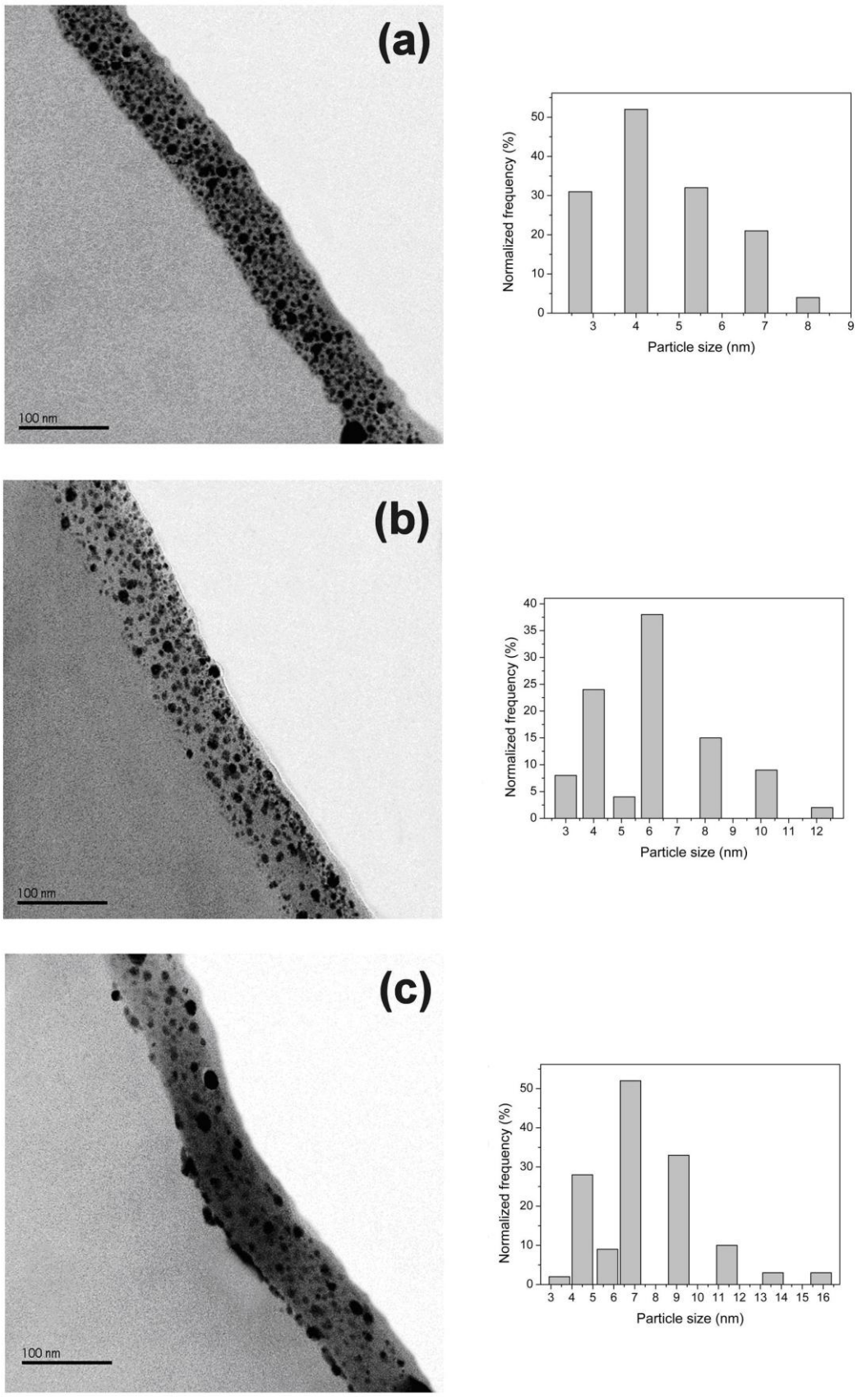

Figure 23. *Cross-sectional STEM–BF images of Ag nanoparticles synthesized in-situ in PEMs of (PAH/PAA)$_{7.5}$ assembled at pH values a) 2.5, b) 3.0 and c) 3.5 with one reaction cycle and corresponding particle size distribution.*

In the PEMs assembled at lower pH values a higher volume fraction of Ag is observed. The nanoparticles have average diameters ranging from 4.5 nm for multilayers assembled at pH 2.5 to 7.4 for those assembled at pH 3.5. Based on measured volume fractions and particle diameters, the concentrations of the Ag nanoparticles in PEMs assembled at different pH were calculated. While the average diameter of the Ag nanoparticles increases with the increasing pH value of the PEM assembly, multilayer films with lower concentrations of nanoparticles are obtained as the pH of the PEM assembly is increased. The concentration values are displayed in Table 1.

Table 1. *Ag/PEM composite properties (1 reaction cycle)*

pH value of the PEM assembly	Silver volume Fraction (%)	Average silver particle diameter (nm)	Silver particle concentrations (particles/cm^3)
2.5	33	4.5±1.5	$6.9 \cdot 10^{18}$
3.0	27	6.1±1.6	$5.2 \cdot 10^{18}$
3.5	22	7.4±2.5	$1.1 \cdot 10^{18}$

For the nanoreactor chemistry, extend of metal ion binding in organic multilayer film is controlled by the degree of ionization of carboxylic acid groups. It was shown previously that 70% of the PAA functional groups exist in the non-ionized carboxylic form in the PEM assembled at a pH value of 2.5, and that the degree of ionization of the carboxylic acid groups of the PAA increases with the increasing pH of the PEM assembly.[68] While in the polyelectrolyte multilayer assembly, ionized carboxyllic groups electrostatically bind with fully ionized groups of PAH in the multilayer assembly, uniform distribution of unprotonated acid groups of the PAA chain within the multilayer film is obtained. At lower pH values there are more carboxylic acid groups relative to carboxylate groups on the PAA chains and also more less-ionized PAA chains relative to the completely ionized PAH chains incorporated into the multilayers due to the polyion chain charge compensation.[92] As a result, at a lower pH of the PEM assembly, more free carboxyl acid groups are available to participate in the subsequent ion exchange with silver cations and hence, higher volume fractions of Ag in the PEMs were obtained. While the pH value of the PEM assembly is the main parameter for controlling the amount

of silver cations adsorbed into the multilayer film, it also influences the final size of the Ag nanoparticles, as observed from the TEM images in Figure 23.

Figure 24 shows an HRTEM image of Ag nanoparticle formed within the polyion multilayer film assembled at pH 2.5 with one reaction cycle in the beginning growth stage.

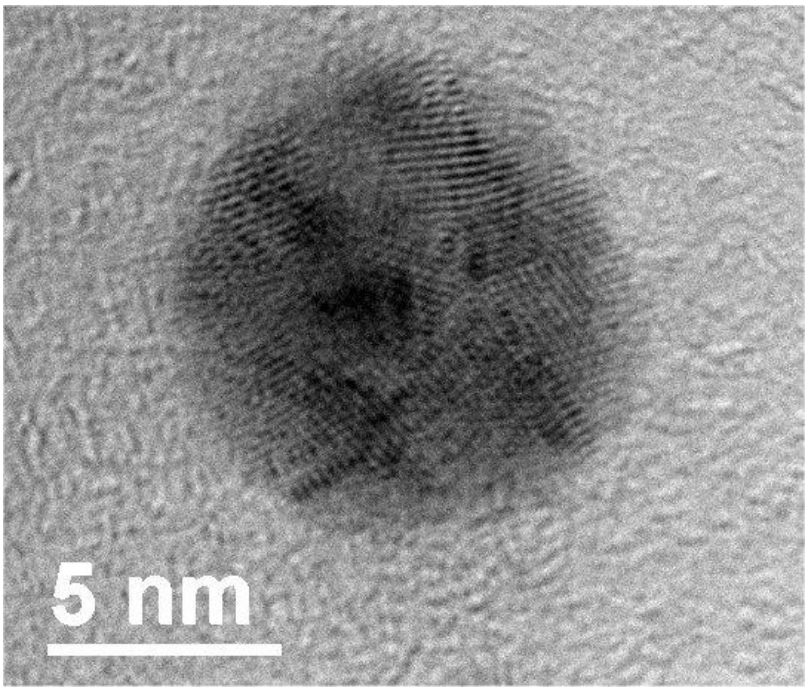

Figure 24. *Spherical aggregate of primary Ag nanoparticles formed within PEMs assembled at pH 2.5 after one reaction cycle.*

After the reduction with $NaBH_4$ of the incorporated silver ions within the multilayer film, the primary formed Ag particles of size between 2-3 nm collide and coalesce into spherical aggregates. Although aggregative based growth may be expected to result in dendritic morphologies with characteristic fractal dimensions, the morphology of agglomerate formed is determined by a competition between the collision rate and coalescence rate.[59] While higher collision rates normally result in fractal like structures, when coalescence rate is high, coalescence occurs almost on contact resulting larger spherical agglomerates formation.[93]

In the solution synthesis of nanoparticles the surrounding polymer limits the particle growth, while the final size of the particle can be controlled by varying the

polymer concentration.[94] Beside nucleation and growth of the inorganic nanoparticles, the aggregative growth of primary inorganic nanoparticles into larger particles has been observed with the in situ synthesis approach in block-copolymers domains.[95] Since the polyelectrolyte chains in dry PEMs are highly interpenetrated and hence the density of the multilayer film is relatively high, small Ag particles with a relatively narrow size distribution were synthesized in the PEMs. The increase in the average nanoparticle diameter with the increasing pH value of the PEMs' assembly could be explained by the changes in the conformational state of the multilayer film as the pH is increased from 2.5 to 3.5. The pH value of the polyelectrolyte assembly strongly influences the conformational arrangement of the weak polyelectrolyte chains. While with an increasing pH value of the PEM assembly more ionized PAA chains spread flat over the surface, a denser conformational arrangement comprised of loops, tails and trains is adopted at lower pH values.[88] Flatter macromolecular arrangements of polyion chains with their assembly induce larger voids within the multilayer film. Therefore, with the increasing pH value of the PEM assembly a more porous PEM structure is obtained. Larger voids within the multilayer assembly accelerate the aggregation of the Ag nanoparticles at higher pH values and hence larger particles with larger size dispersity in the multilayer film were obtained as the assembly pH is increased from 2.5 to 3.5.

Furthermore, at higher pH values the PAA is more ionized and thus a smaller number of PAA chains are adsorbed onto the completely ionized PAH layer due to their charge compensation. While the carboxylic acid groups have particle-stabilizing attributes,[84] a smaller number of carboxylic acid groups within the multilayer structure assembled at higher pH values could be the cause for more pronounced aggregation of Ag nanoparticle as the assembly pH is increased from 2.5 to 3.5. Consequently, since the volume fraction of Ag in the composite film increases with decreasing pH, a higher concentration of smaller Ag nanoparticles in the PEM at low pH values is obtained.

An opposite trend in Ag nanoparticle size with the increasing assembly pH was observed was observed as the in situ reaction was performed with a dry chemical method by reduction in H_2 gas atmosphere at elevated temperature.[84-85] As the assembly pH was increased from 2.5 to 4.5, the average Ag particle size decreased from 3.8 nm to 2.1 nm. According to the diffusion limited aggregative growth model (see introduction) of nanoparticles in polymers higher diffusion time of the primary particles result in smaller nanoparticle formation. The only parameter that could affect the diffusion time of the Ag nanoparticles in PEMs,

comparing the wet and dry synthesis conditions, is the effective viscosity of the polymer matrix. Since polyion chains are water soluble, chemical reduction in the aqueous solution due lower viscosity of the multilayer polyion film cause larger diffusivity of the primary particles in the film which result in larger extent of nanoparticle aggregation and thus larger particle size. The increase in Ag particle size formed by a wet chemical reduction with the increasing assembly pH is ascribed to larger voids formed within the PEM assembled at higher pH values. On the other hand, in the case of H_2 gas atmosphere reaction dry PEMs were used as templates for the Ag nanoparticles synthesis. Since the dry PEM films are highly viscous and stiff the migration of the primary particles within the film is low. The decrease in nanoparticle average diameter with the increasing assembly pH can thus be assigned to larger primary interparticle distances at higher pH which even further increase the particle diffusion time. After reaction is completed (1 hour in $NaBH_4$ solution) a single crystalline cubic Ag nanoparticles were formed within the PEM multilayer film.

In Figure 25 HRTEM of the single crystalline cubic Ag nanoparticle formed within the PEM assembled at the pH 2.5 after one reaction cycle is shown.

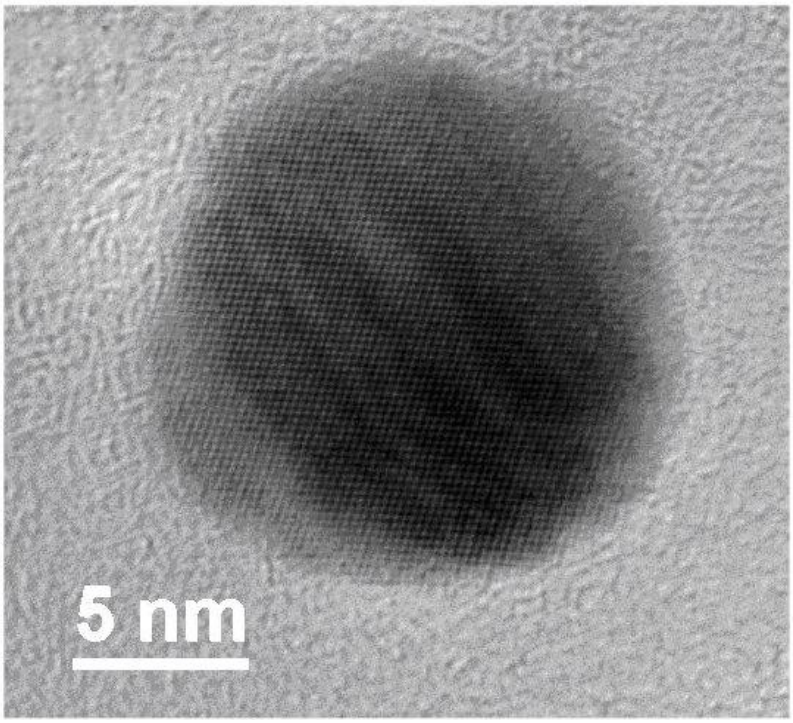

Figure 25. *HRTEM of single crystalline Ag nanoparticle formed within the PEM assembled at pH 2.5 after reaction is completed.*

Metallic nanostructure formation in a solution typically involves the fast nucleation of primary particles and the subsequent growth by two mechanisms: aggregation and Ostwald ripening, where dissolution –precipitation based growth is generally believed to be a dominant path for crystal growth.

The reduction of Ag ions by $NaBH_4$ is an extremely rapid process due to the strong reducing ability of $NaBH_4$, which results in the formation of very small primary single crystalline silver nanoparticles within the PEMs. Since the in-situ synthesis of Ag nanoparticles in PEMs is performed in $NaBH_4$ aqoues solution Brownian motion-driven particle collisions between primary particles may occur.[112-114] These collisions are especially effective if the particles make contact in a parallel lattice orientation, which leads to the reduction of total energy as a result of the elimination of the solid-liquid interface and an increase in entropy. When the particles with the parallel crystallographic orientation are approaching each other, there will be a driving force to form chemical bonds between atoms of opposing surfaces so as to achieve the full coordination. As a result single crystalline Ag nanoparticles are formed in PEMs. The simultaneous dissolution-precipitation growth of the Ag nanoparticles, where the smaller primary particles dissolve on the expense of larger ones is also possible. However, an imperfect oriented attachment and fast diffusion rates may lead to the formation of dislocations between the neighboring particles.

In PEM assembled at pH 2.5 synthesized with one reaction cycle structural faults are observed in cubic Ag nanoparticles as shown in Figure 26.

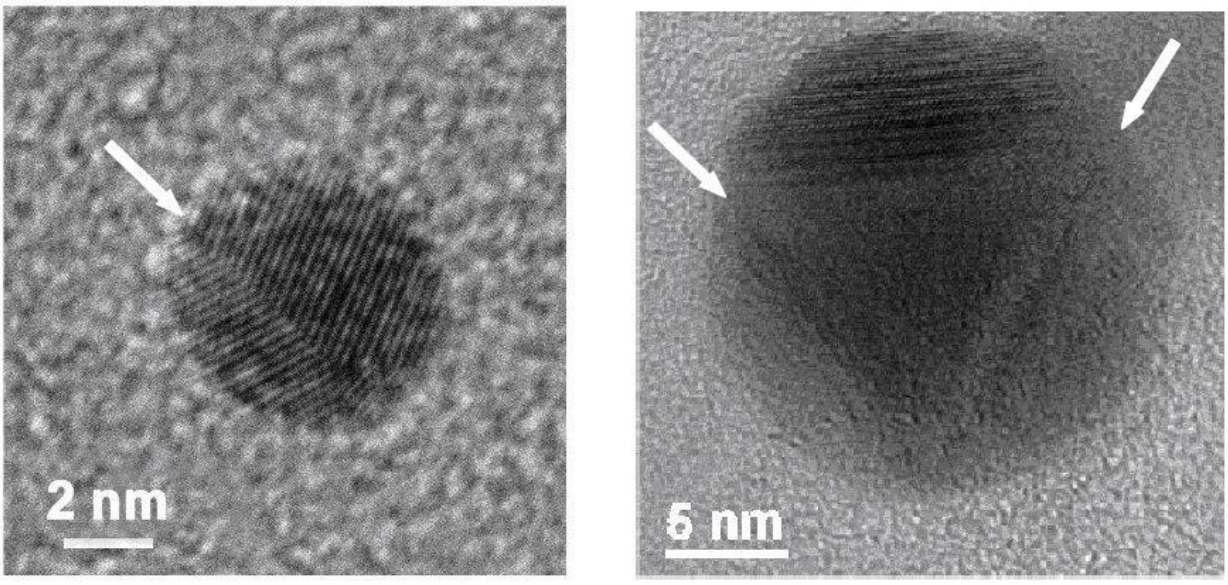

Figure 26: *Twinning structures in Ag nanoparticles formed within the PEMs assembled at pH 2.5 after one reaction cycles.*

Twinning structures have been assigned as a result of aggregative growth of primary particles.[96] The appearance of stacking faults is considered as a consequence of oriented attachment growth of the particles, suggesting the occurrence of the initial particle-particle bonding.

4.2.2 Controlling metal (Ag) concentration and nanoparticle size by varying the number of the reaction cycles (n)

The increase in the volume fraction of the Ag in organic/inorganic composite films can be obtained by repeatedly cycling the synthesis methodology. The reduction of the silver cations incorporated in the PEM by the first absorption process regenerates the carboxylic acid groups, which enables further silver-ion binding in the multilayer film.[63] Figure 27 shows TEM images of the silver nanoparticles in the $(PAH/PAA)_{7.5}$ multilayer film assembled at pH=2.5, synthesized with a) one (n=1) and b) three (n=3), respectively.

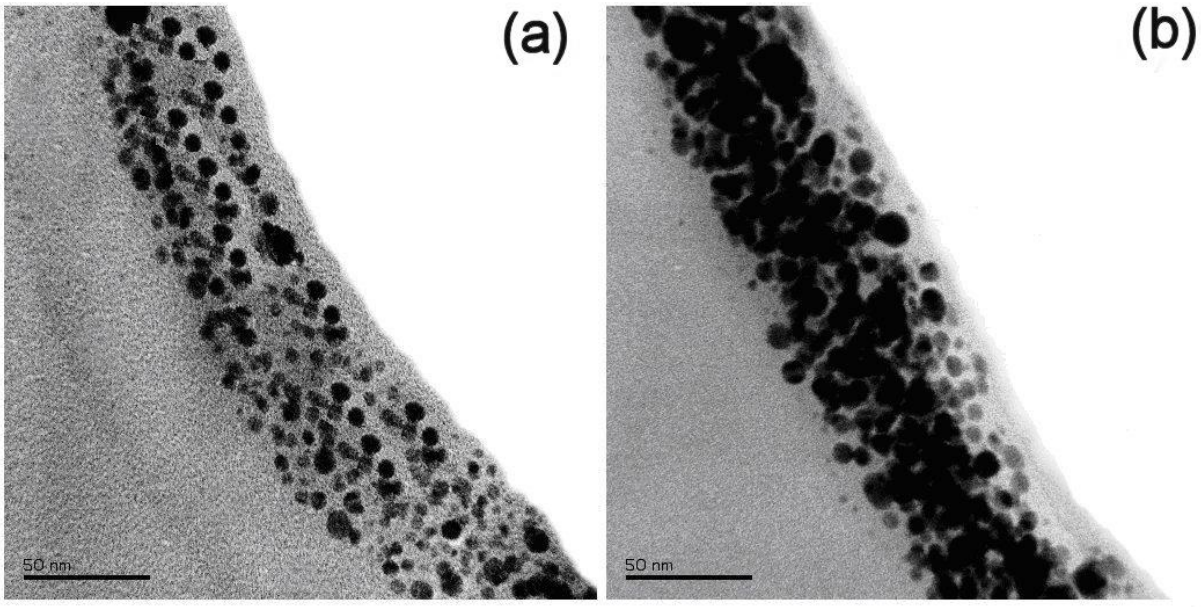

Figure 27. *Cross-sectional STEM BF images of Ag nanoparticles synthesized in-situ in PEMs assembled at a pH value of 2.5 a) bright-field image n=1, b) bright-field image n=3.*

With an increasing number of reaction cycles (n), Ag nanoparticles continue to be homogeneously distributed throughout the PEM film, though a significant increase in the Ag particle size in the films with n=3 is observed, compared to the films with

n=1. As the reaction cycle is repeated three times, the volume fraction of the Ag nanoparticles in the PEMs assembled at a pH 2.5 is increased from 33% to 65%.

Table 2. *Ag/PEM composite properties (3 reaction cycles)*

NUMBER OF THE REACTION CYCLE (n)	Silver VOLUME FRACTION (%)	AVERAGE Silver PARTICLE DIAMETER (nm)	Silver PARTICLE CONCENTRATIONS (particles/cm^3)
1	33	4.5±1.5	$6.9 \cdot 10^{18}$
3	65	6.7±2.6	$4.1 \cdot 10^{18}$

The average Ag particle diameters in the films assembled at a pH 2.5 increased from 4.5 nm to 6.7 nm after three reaction cycles. The Ag particle size distribution in PEMs after three reaction cycles is shown in Figure 28.

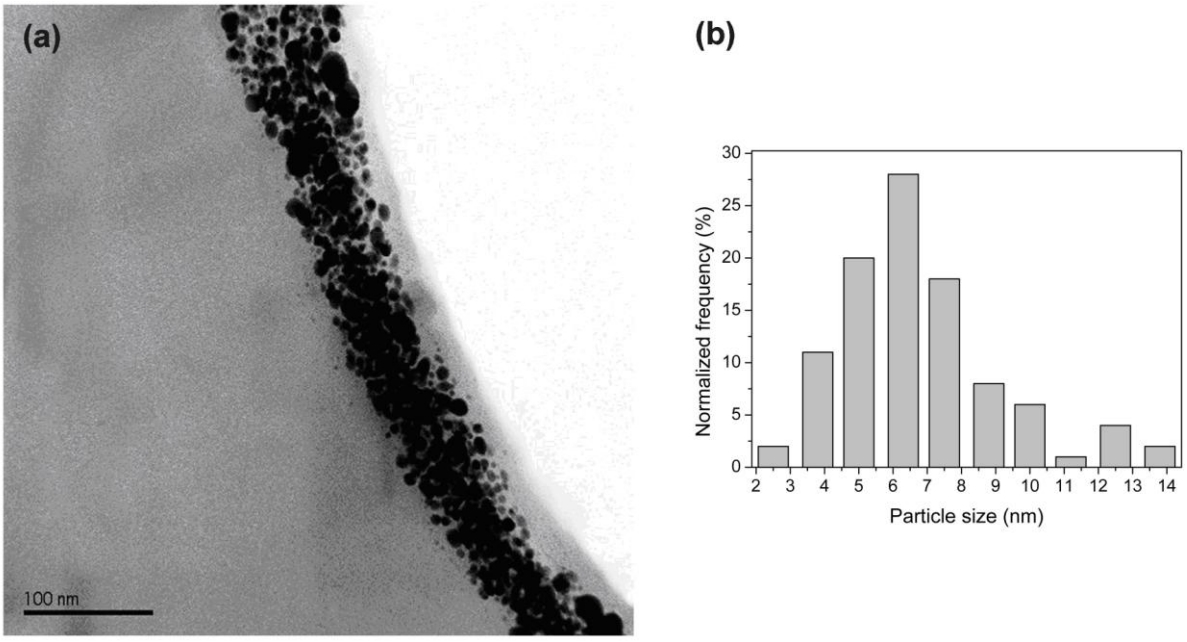

Figure 28. *a) Cross-sectional STEM BF images of Ag nanoparticles synthesized in-situ in PEMs assembled at a pH value of 2.5 after three reaction cycles b) histograms of Ag nanoparticle size distribution.*

If the nanoparticle concentration is assumed to remain constant, after three reaction cycles, this would mean that all newly introduced silver is incorporated into existing particles. Based on this assumption and on the increase in the volume fraction of silver in the multilayer film from 33% to 65% the nanoparticle size after three reaction cycles should be 5.7 nm in contrast to the observed 6.7 nm.

The concentration of the Ag nanoparticles, calculated on a basis of the volume fraction and average particle size in the films (Table 2) decreased from $6.9 \cdot 10^{18}$ to $4.1 \cdot 10^{18}$ particles/cm^3 after three reaction cycles. A simultaneous increase in the particle size and a decrease in the particle concentration suggest that with increasing the number of reaction cycles (n) the nanoparticle growth in the PEM involves the diffusion based growth of the larger particles due to the dissolution of smaller ones.

Ag nanoparticles synthesized in PEMs assembled at a pH value of 2.5 with one reaction cycle were stabilized by the surrounding polyelectrolyte film and hence practically no aggregation of the particles was observed after the reaction. Although the PEM structure assembled at a pH 2.5 is relatively dense, further binding of Ag cations to the re-generated carboxylic acid groups by repeating the reaction cycle causes a closer proximity of the incorporated cations to the previously formed nanoparticles in the PEM film and hence after reduction of the Ag ions diffusion based growth of the nanoparticles may occur. Therefore, besides varying the pH value of the PEM film's fabrication, control over the concentration and size of the in-situ synthesized Ag nanoparticles in multilayer films is also obtained by repeatedly cycling the synthesis process.

With the increasing pH, simultaneous increase in the average particle diameter and decrease in the concentration of the particles was observed, whereas larger average particle diameter at lower assembly pH was ascribed to the higher loading and closer proximity of the metal ions in the multilayer film. As the nanoparticle synthesis methodology is repeatedly cycled due to the increase the ion content, the increase of both nanoparticle concentration and size was obtained.

4.2.3 Optical properties of Ag nanoparticle- PEMs composite films

UV-vis transmission measurements were used to follow the changes in the size and in the concentration of the in-situ synthesized Ag nanoparticles as the pH value of the PEM assembly was varied. The optical spectra of the Ag nanoparticles embedded in the PEM film are shown in Figure 29.

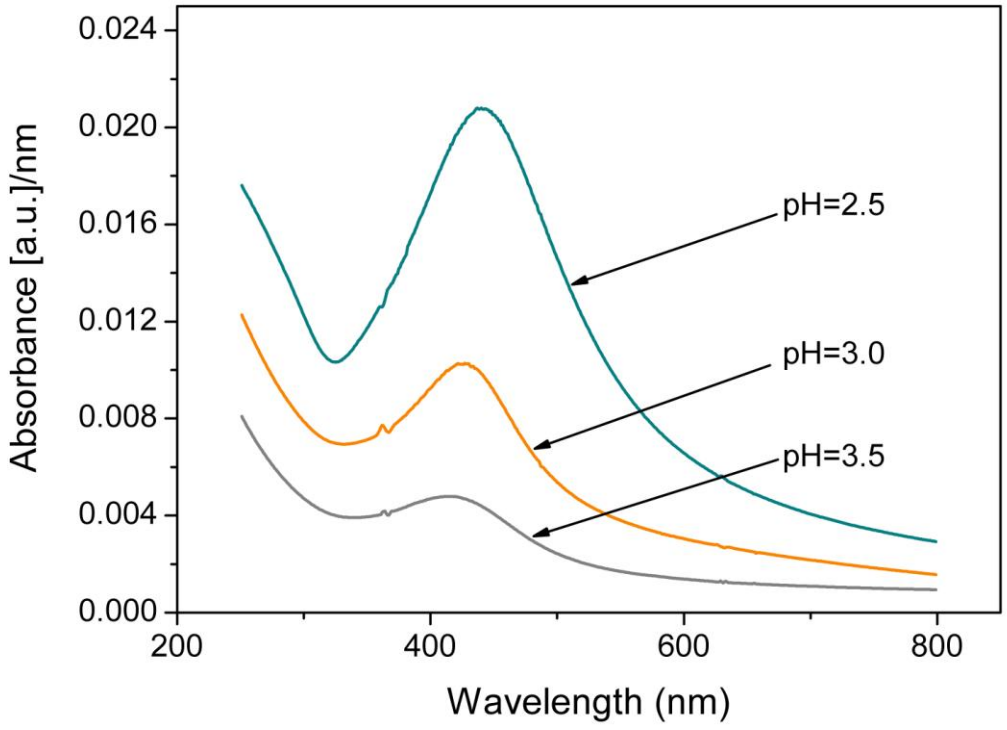

Figure 29. *The UV-vis absorption spectra normalized to the film thickness of the Ag nanoparticles synthesized by one reaction cycle in (PAH/PAA)$_{7.5}$ assembled at pH 2.5, 3.0 and 3.5.*

From the spectra it is clear that the characteristic surface-plasmon resonance (SPR) of the Ag nanoparticles dominates the visible wavelengths with a maximum centered at 440 nm. The existence of a single absorption peak in the visible region confirms the observations from the TEM images, that the silver nanoparticles in the PEMs are essentially spherical.[97]

The bandwidthh, the intensity and the position of the surface-plasmon resonance wavelength of the nanocomposite materials are influenced by the volume fraction, the shape and the size of the metal cluster in the film, as well as by the interparticle separation and the dielectric properties of the surrounding medium.[98-99] The SPR maximum normalized to the film thickness increases with the

decreasing pH value of the PEMs' assembly. Furthermore, the red shift of the SPR frequency is also observed as the pH value of the multilayer film is decreased. Since the synthesized Ag nanoparticles are nearly spherical in all samples, the particle shape is expected to have a negligible effect on the shift of the SPR's peak position.

Table 3. *Ag/PEM composite optical properties*

pH of the PEM assembly	SPR wavelength $\lambda_{R,max}$ (nm)	FWHM (nm)
2.5	440	110
3.0	427	97
3.5	414	90

For the mean particle diameters that are much smaller than the incident wavelength, the classical theory developed by Mie[4,100] predicts that the SPR's wavelength should be independent of the particle size. Therefore, it appears that the red shift of the SPR wavelength with the decreasing pH of the PEM assembly could be mainly caused by a variation in the volume fraction of Ag nanoparticles among the samples. Moreover, the simultaneous increase in the volume fraction of the Ag and the decrease in the interparticle spacing lead to a change in the dielectric constant of the composite film due to electro-dynamic interactions between neighboring particles, which is thought to be responsible for the red shift of the SPR's peak position.[98,101]

Additionally, we can see that the plasmon bandwidthh (i.e., the full width at half maximum – FWHM) in Figure 29 of the SPR increases with a decreasing nanoparticle size. The experimental results are in agreement with the theory, since in the intrinsic-size region, where the particle diameters are much smaller than the wavelength of the exciting light, classical[102] and quantum-mechanical[103] theories predict a 1/R dependence of the plasmon bandwidth.

Figure 30 shows the UV-vis absorption spectra of Ag nanoparticles in PEMs fabricated at a constant pH value as the number of reaction cycles (n) is increased from 1 to 3.

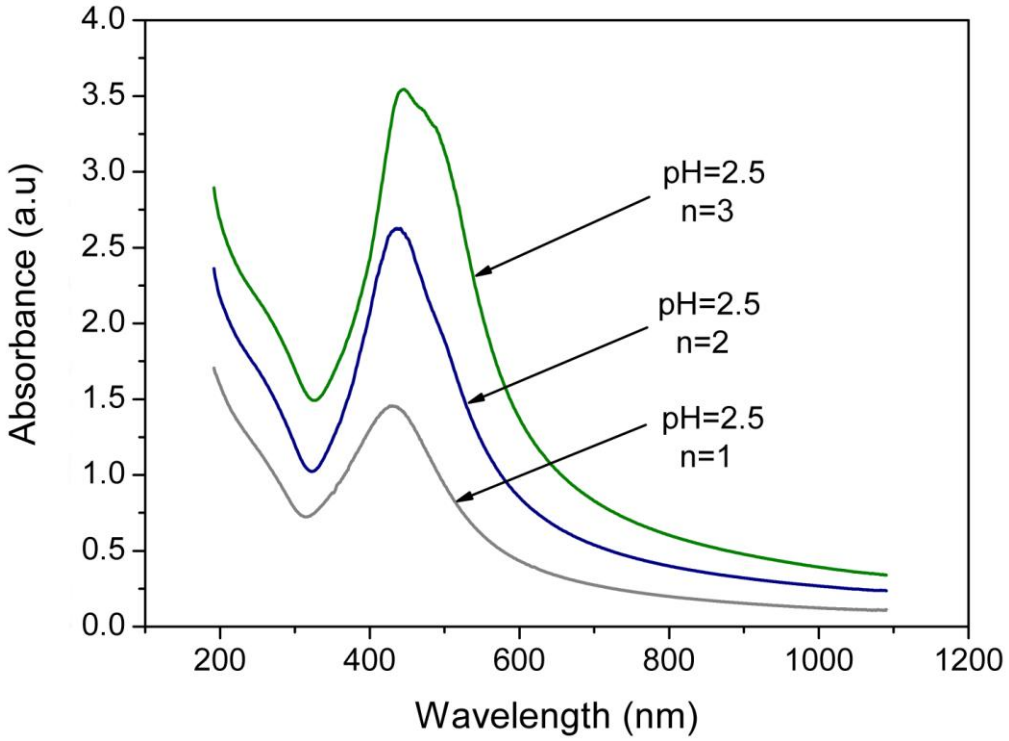

Figure 30. *The UV-vis absorption spectra of Ag nanoparticles synthesized in (PAH/PAA)$_{7.5}$ assembled at a pH 2.5 with)n=1,n=2 and n=3.*

By repeating the synthesis process an increase in the volume fraction of Ag in the PEM film is obtained, accompanied by an increasing particle size and decreasing inter-particle gaps. The optical spectra of these films show broadening of the plasmon band and a red shift of the SPR peak position as n increases from 1 to 3. It was previously reported that the particles begin to interact with one another at an inter-particle distance of approximately one particle diameter.[104] This phenomenon is more pronounced for volume fractions above 40% because of particle coalescence and the formation of a network structure.[105]

An average measured interparticle spacing in PEMs is defined as the shortest distance between the surfaces of neighboring particles and normalized to the particle diameter. After one reaction cycle for pH 2.5 assembled films with 4.5 nm average diameter particles at volume fraction of 33% the interparticle spacing is about 1.4 diameters (6 nm). Based on the measurements the interparticle

interaction should be minimum after one reaction cycle which is consistent with a single absorption peak observed. By repeating the synthesis process of Ag nanoparticles in a PEM assembled at a pH value of 2.5 for three times, close proximity of the Ag nanoparticles was achieved, as observed in Figure 27. In addition due to higher proximity of the particles, agglomeration of the Ag nanoparticles is more pronounced and thus slight deviation in the nanoparticle shape occurs. After three reaction cycles the particle films with 6.7 nm diameter particles at a volume fraction of 65%, the interparticle spacing is about 0.4 diameters (2.7 nm) at which interparticle interactions become significant. The changes in the shape of the particles and volume fractions as n increases from 1 to 3 reflect in broadening and eventually splitting of the absorption curve[84] due to appearance of the longitudinal plasmon resonance mode as observed from the SPR curves in Figure 30. Therefore, the evolution of the shape of the SPR is consistent with increasing interparticle interactions and the changes in the shape of the Ag nanoparticles as the interparticle distance in the multilayer film is decreased.

4.3 In-situ synthesis of semiconducting (ZnS) nanoparticles in PEMs

The zinc sulfide (ZnS) nanoparticles were synthesized in situ in 7.5 bilayered PEM matrixes. To obtain the control over the volume fraction and over the size of the ZnS particles in the composite film, the matrix was assembled at the pH value of 2.5 and 3.0, respectively. The reaction cycle comprised of the zinc ion binding to the ionized groups of the polycation (PAA) followed by subsequent sulfidation of the ions incorporated in the matrix was varied from n=1 to n=3.

4.3.1 *Growth characteristics of ZnS nanoparticles in PEMs assembled at different pH values*

The cross-sectional TEM images of the ZnS/PEM composite films fabricated during the PEM assembly at pH values of 2.5 and 3.0 (Figure 31) indicate that the size of the in-situ synthesized ZnS particles is in the range of a few nanometers. The ZnS nanoparticles in the PEM are spherical and evenly distributed within the polyion multilayer films.

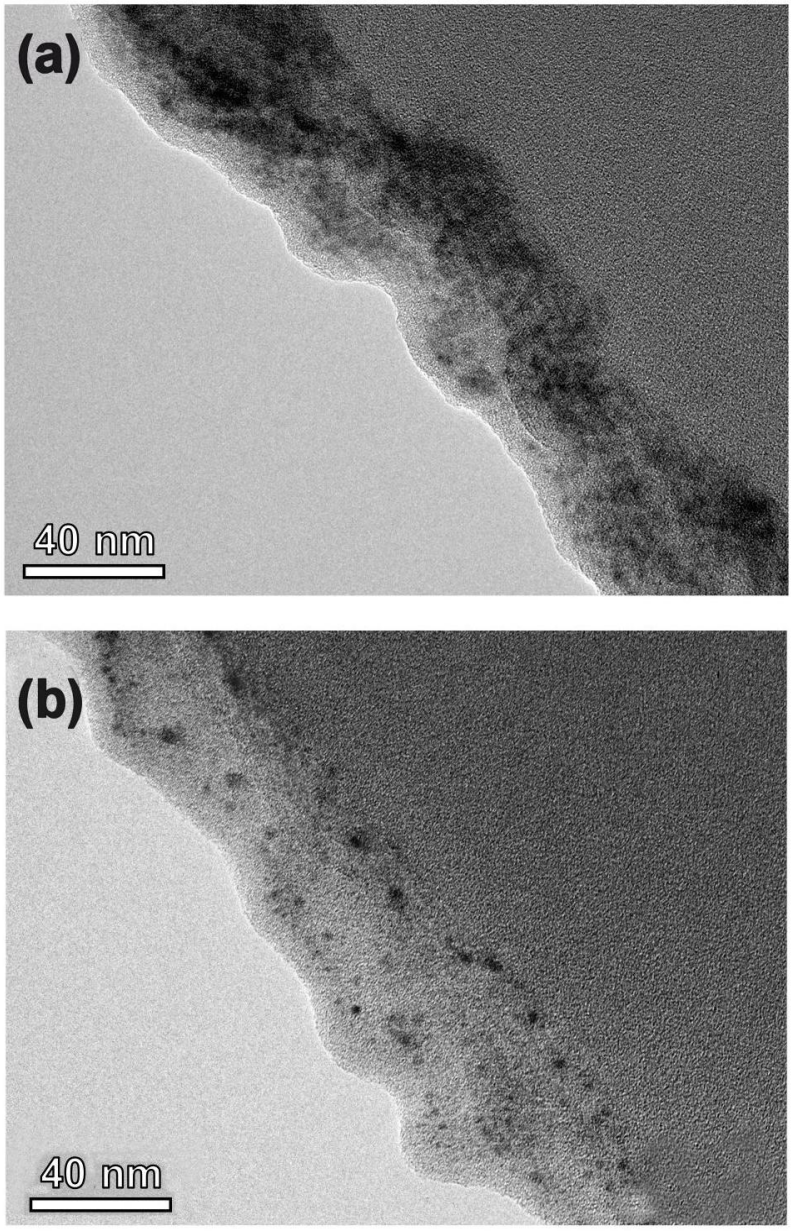

Figure 31. *Cross-sectional bright-field TEM images of ZnS nanoparticles synthesized in-situ in PEMs assembled at a) pH=2.5 and b) pH=3.*

By increasing the pH value of the PEM assembly from 2.5 to 3.0 a lower volume density of ZnS nanoparticles within the multilayer film is observed, together with a reduced thickness of the pristine matrix assembled at the lower pH. After the ZnS nanoparticle precipitation, from the increase in the film thickness, calculated volume fractions of ZnS of 30% and 16% were obtained in the polyion matrixes assembled at pH values of 2.5 and 3.0, respectively. The explanation for different volume fraction of ZnS nanoparticles in PEM is the same as in the case of the in-situ synthesized Ag nanoparticles in PEMs assembled at different pH values. The PEM template assembled at the lower pH value allows more Zn ions to coordinate along the PAA chains, as the template is exposed to the Zn-ion solution at the pH value of 5.5, at which point the PAA chains become fully ionized. As a result, after sulfidation of the adsorbed Zn ions, a higher volume density of the ZnS nanoparticles in the polyionic film assembled at the pH value of 2.5, compared to that at pH=3.0, was obtained, as is clear from Figure 31.

Due to the coordination of the Zn ions with the carboxylate groups of the PAA chains, after the sulfidation reaction, their growth is restricted within specific regions of the matrix by the surrounding polyion chains. Moreover, the electrostatic forces within the matrix hinder the particle aggregation and thus enable the ZnS particles to be well dispersed within the PEM film. Figure 32 shows the ZnS nanoparticle size distribution in polyion matrix formed at the assembly pH 2.5 and 3.0 after one reaction cycle. The average ZnS particle diameters were 3.2±0.2 nm and 3.6±0.4 nm in the polyion matrixes assembled at pH values of 2.5 and 3.0, respectively.

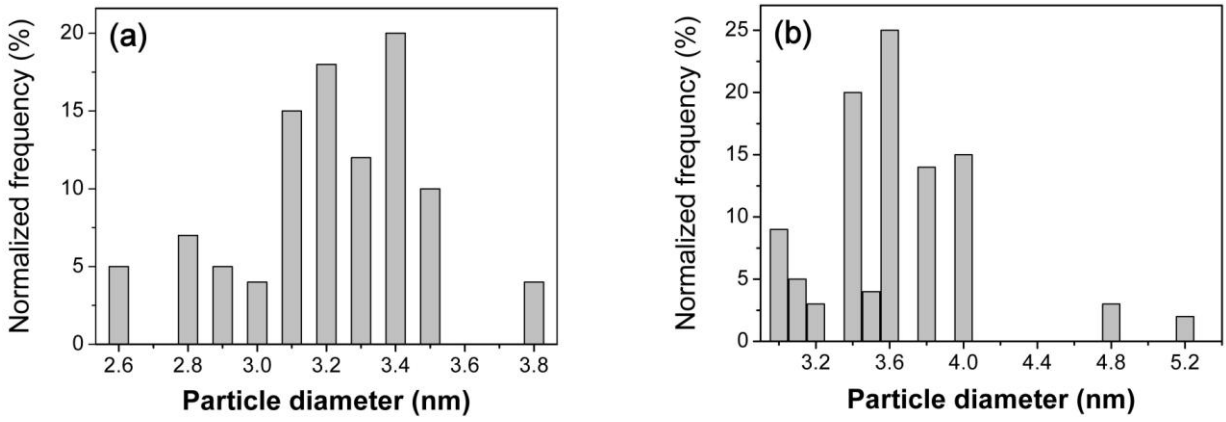

Figure 32. *Histograms of ZnS nanoparticle size distribution in PEMs assembled at pH (a) 2.5 and (b) 3.0.*

In the weak PEM assembly, a high interpenetration of the oppositely charged PE chains yielded a dense polyion matrix within which small cavities can exist.[85] Consequently, small ZnS nanoparticles were formed within the multilayer matrix. The ZnS nanoparticles nucleated within the polymer cavities continued to grow until steric stabilization of the nanoparticles was obtained. Since the cavity walls physically restrict the particle growth, the morphology and the size of the ZnS crystallites can be attributed to the morphology of the void spaces induced by the pH-value-determined molecular organization of the polyion chains in the PEM assembly. Regardless of the pH of the multilayer assembly, the shape of the synthesized ZnS crystallites was spherical, which may indicate the formation of spherical voids within the polymer network fabricated by the LbL self-assembly of the weak polyions.

Figure 33 shows the ZnS nanoparticles formed in the matrixes assembled at pH values of 2.5 and 3.0.

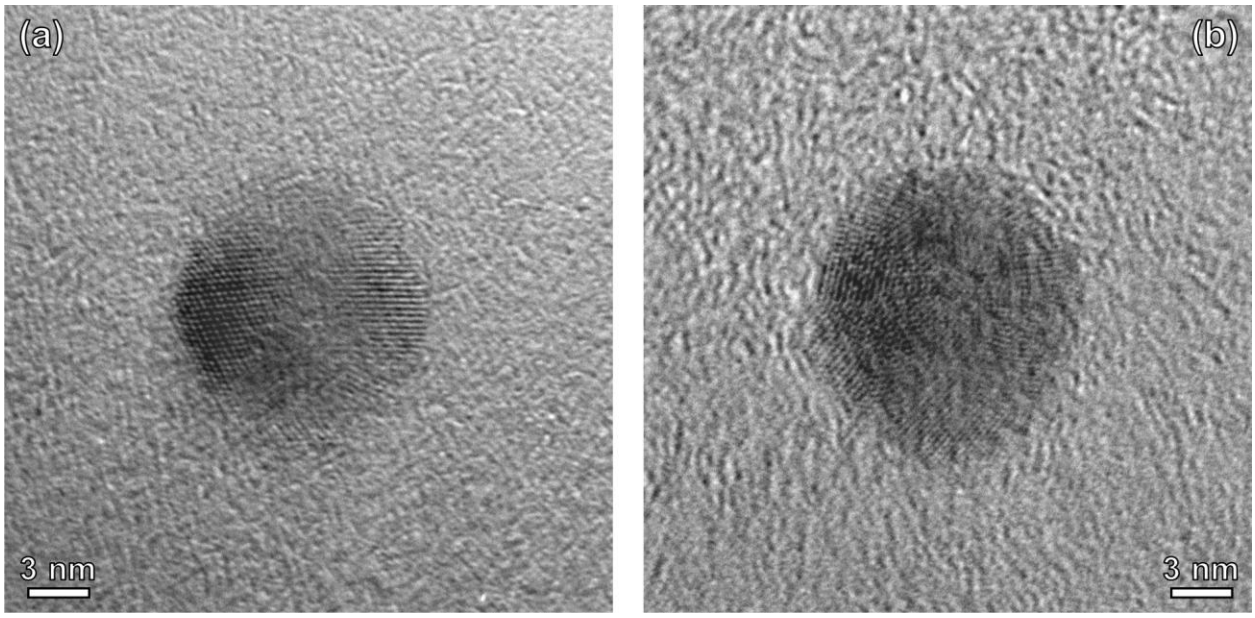

Figure 33. *Lattice images of nanosized ZnS crystal clusters formed in polyion matrix assembled at the a) pH=2.5 and b) pH=3.0.*

The morphology of the ZnS nanoparticles suggests that the as-formed ZnS clusters are constructed of more primary building particles of different orientations. In order to reduce the high surface energy the primary particles, which are 2–3 nm

in diameter, tend to assemble into larger clusters by a random-aggregation mechanism.

The aggregation of the nanoparticles is even more likely to occur at a pH value close to the iso-electric point of the ZnS crystal surfaces, as the net charge of the particle double layer is decreased. Since precipitation of the ZnS crystallites within the polyion matrix was performed in a Na_2S solution at a pH value of 5.5, which is in the range of the average iso-electric point of a ZnS nanoparticle, the Brownian-motion-driven particle collisions can effectively overcome the surface-repulsive forces resulting in the agglomeration of the primary ZnS crystallites.[107] Furthermore, as the pH value of the PEM assembly was increased from 2.5 to 3.0, some larger clusters of primary ZnS particles were formed in the PEM.

In Figure 34, (a) the ZnS cluster formed of many primary ZnS particle and (b) single-crystalline ZnS nanoparticle after, synthesized in PEM at the assembly pH 3.0 are shown.

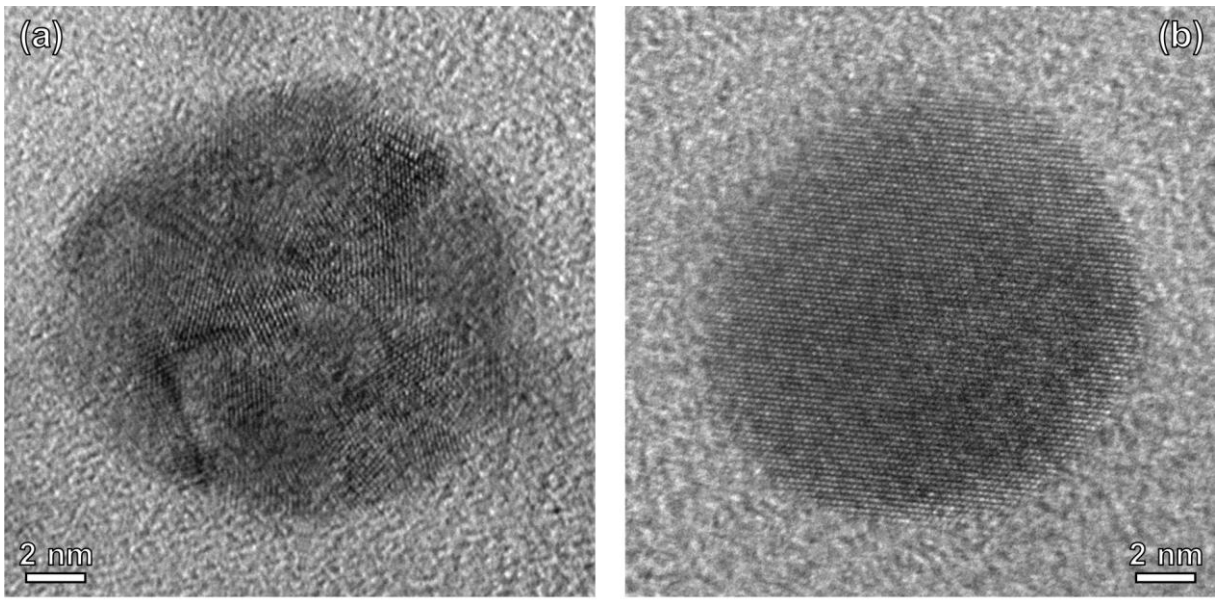

Figure 34. *HRTEM images of the ZnS nanocrystallites formed in PEM assembled at pH=3.0 a) polycrystalline ZnS particle, (b) single-crystalline ZnS particle.*

As the PE assembly pH is increased, the ZnS clusters within the polyion matrix were formed by aggregation of more primary ZnS particles. Since the voids in the polyion matrix assembled at higher pH values of the polyion assembly contained

more free carboxylic groups, which exhibited a particle-stabilizing effect,[84] the aggregation of the primary ZnS particles in the polyion matrix is more pronounced as the pH value of the polyion assembly was increased to a value of 3.0 (Figure 33). Furthermore, with the increase in the assembly pH the flatter conformational arrangement of the polyion chains in the multilayer matrix induces larger void spaces within the polymer network, thus the agglomeration of the primary particles is less suppressed as the pH value of the polyion matrix was increased.

Within the clusters, primary ZnS particles aggregated in a random manner underwent a subsequent recrystallization process, resulting in single-crystalline particles, as shown in Figures 35a and 35b.The electron micro-diffraction patterns, shown in Figures 35(c) and 35(d), indicate that the ZnS particles possess the cubic type sphalerite crystal structure.

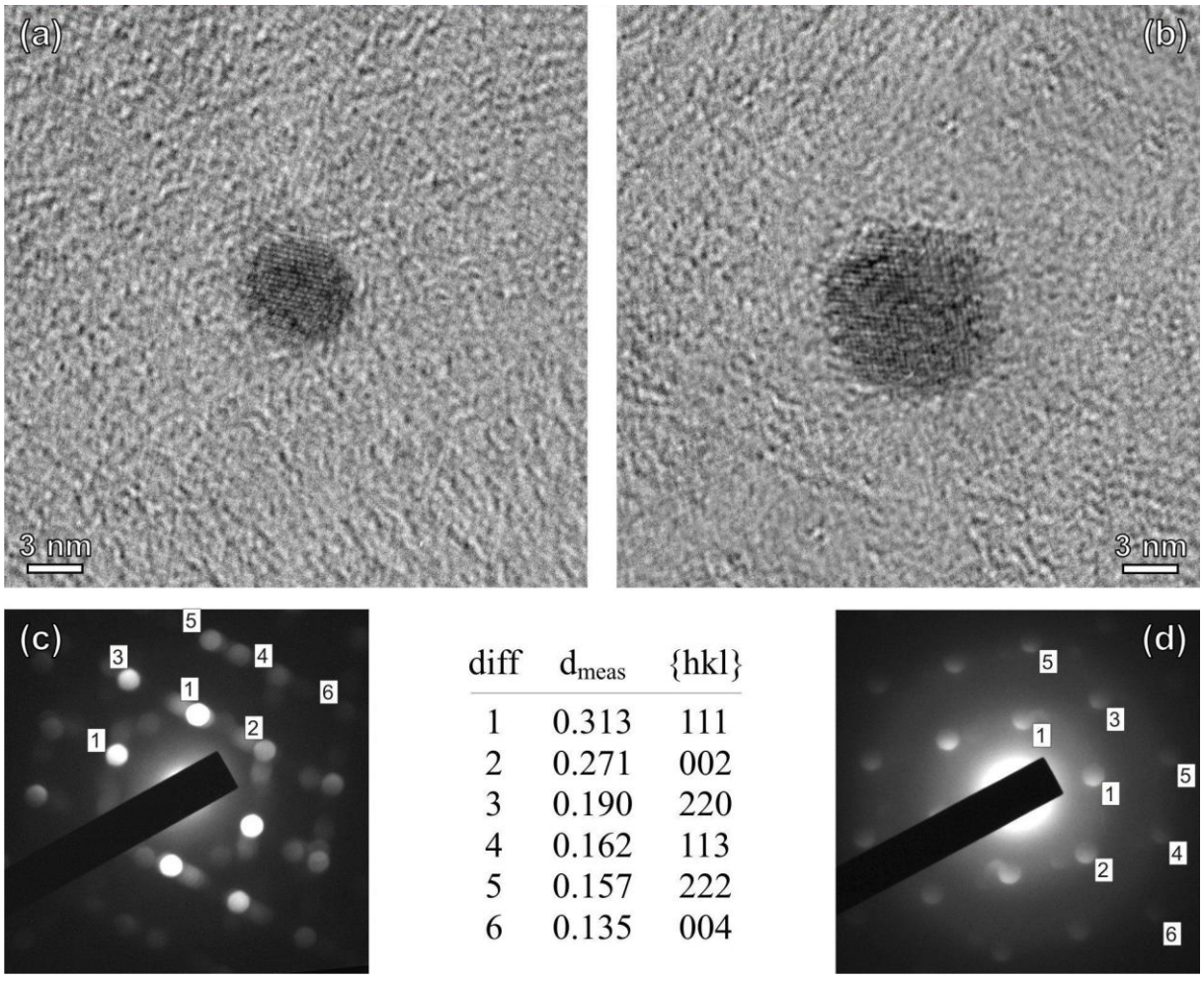

diff	d_{meas}	{hkl}
1	0.313	111
2	0.271	002
3	0.190	220
4	0.162	113
5	0.157	222
6	0.135	004

***Figure 35**. HRTEM images of the ZnS nanocrystallites formed in PEM assembled at a) pH=2.5 and b) pH=3.0 with the corresponding micro-diffraction patterns along the zone-axes c) [112] and d) [110], respectively.*

A high proximity of very small crystallites within the ZnS aggregates can induce the crystal growth via an oriented-attachment (OA) mechanism.[108] With the cluster formation, primary nanoparticles combine with their high energy interfaces, thereby releasing their free surface energy. According to the OA-based coarsening mechanism, small distances between the particles caused by a random aggregation can ensure jiggling of the nanoparticles as a result of the Brownian motion and induce adjacent surfaces short-range interaction that make possible the reorientation of the adjacent particle in order to adopt the lowest energy conformation represented by the coherent particle-particle interface. In addition to ZnS, an OA-based coarsening mechanism was also reported for TiO_2, FeOOH and CoOOH nanocrystallites,[109-110] whereas the formation of a coherent interface with ZnS nanoparticles is even more likely to occur due to the high symmetry of the sphalerite crystal structure.[108,112-113] While the oriented attachment of individual particles normally results in the formation of irregularly-shaped crystallites with abrupt edges, the formation of rounded ZnS crystallites could be attributed to simultaneous diffusion via surface reorganization, which may eliminate the indents at the particle contacts.[109]

The sphalerite structure has been reported as the more stable ZnS polymorph for the crystallites with an average diameter below 7 nm at 300K due to the effect of water molecules adsorption on the surface of the ZnS particles.[108] Although the dissolution-precipitation-based growth of the sphalerite particles in a pure aqueous solution at room temperature is kinetically stabilized due to the extremely low solubility, the increasing ionic strength of the reaction medium by the addition of the excess S^{2-} ions triggers an unsatisfied surface coordination, thereby increasing the surface energy of the particles.[114] As a result, due to the elevation of the chemical potential of the surface atoms, a diffusion-based coarsening of the larger ZnS particles due to the surface precipitation of the solvated ions (Zn^{2+} and S^{2-}) at the expense (dissolution) of the smaller ZnS crystallites within the ZnS clusters is also possible.

4.3.2 *Growth characteristics of ZnS nanoparticles in PEMs induced by variation in the number of reaction cycles*

By cycling the synthesis process, ZnS nanoparticles retain their spherical shape and continue to be homogeneously distributed within the composite film as shown

in Figure 36. The volume density and the size of the ZnS nanoparticles in the PEM are increased by repeating the ion-loading-precipitation reaction cycle. After the first precipitation cycle the carboxylic groups are regenerated which enable further Zn ion binding within the polyion matrix. As a result, in PEM assembled at pH-value of 2.5 after three reaction cycles, an increase in the volume fraction to 60% is observed.

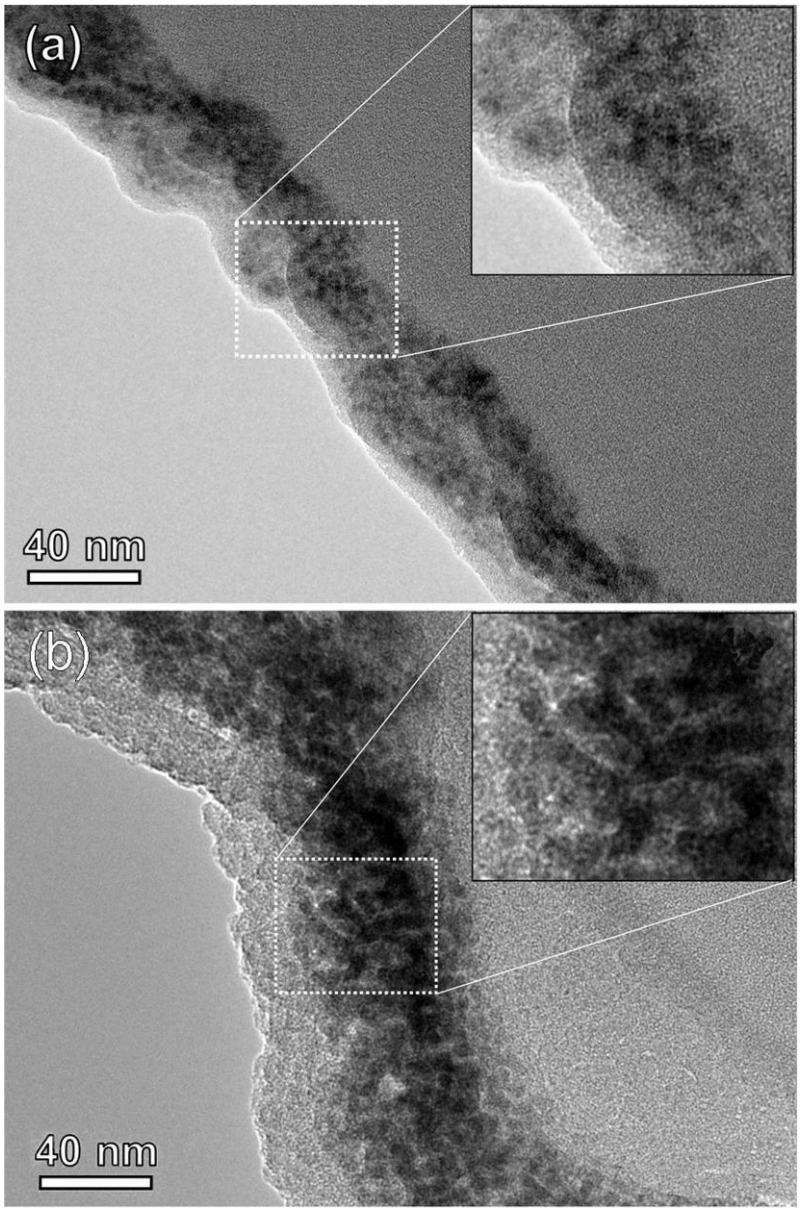

Figure 36. *Cross-sectional TEM images of ZnS nanoparticles synthesized in-situ in PEMs assembled at pH values of 2.5 after a) n=1 and b) n=3 reaction cycles.*

The size distribution of ZnS nanoparticles in PEM assembled at pH 2.5 after three reaction cycles is shown in Figure 37.

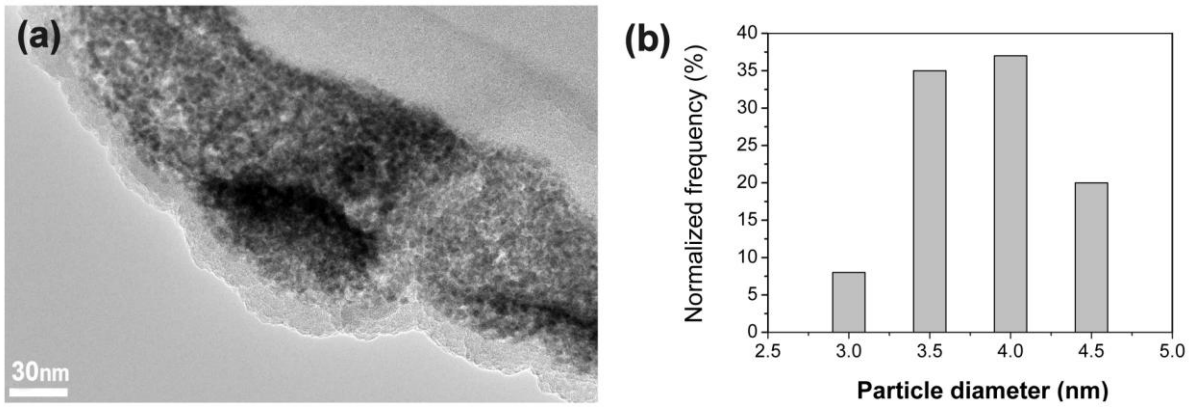

Figure 37. *(a) Cross-sectional TEM image of ZnS nanoparticles in PEM assembled at pH 2.5 after three reaction cycles, (b) histogram of the ZnS nanoparticle size distribution.*

The average ZnS particle diameter was increased from 3.2±0.2 nm to 3.9±0.3 nm after three reaction cycles in the PEM assembled at a pH 2.5. Although the ZnS nanoparticles synthesized in the PEM were sterically stabilized by the surrounding polymer network, any further metal-cation binding in close proximity to the existing particle after the sulfidation reaction of the Zn ions favors further particle growth via the Ostwald-ripening mechanism. With the close particle contact, a diffusion-precipitation-based growth takes place and the larger primary particles increase in size, consuming the freshly available constituent material.

For the ZnS nanoparticles, synthesized in PEMs after three reaction cycles, the SAED pattern (Figure 38b) recorded over the area of isolated ZnS nanocrystallites (Figure 38a) indicates the cubic crystal structure of ZnS. The lattice parameter *a*, calculated from the measured *d*-spacings, is 5.4Å, which corresponds to the cubic sphalerite (β-ZnS) structure.

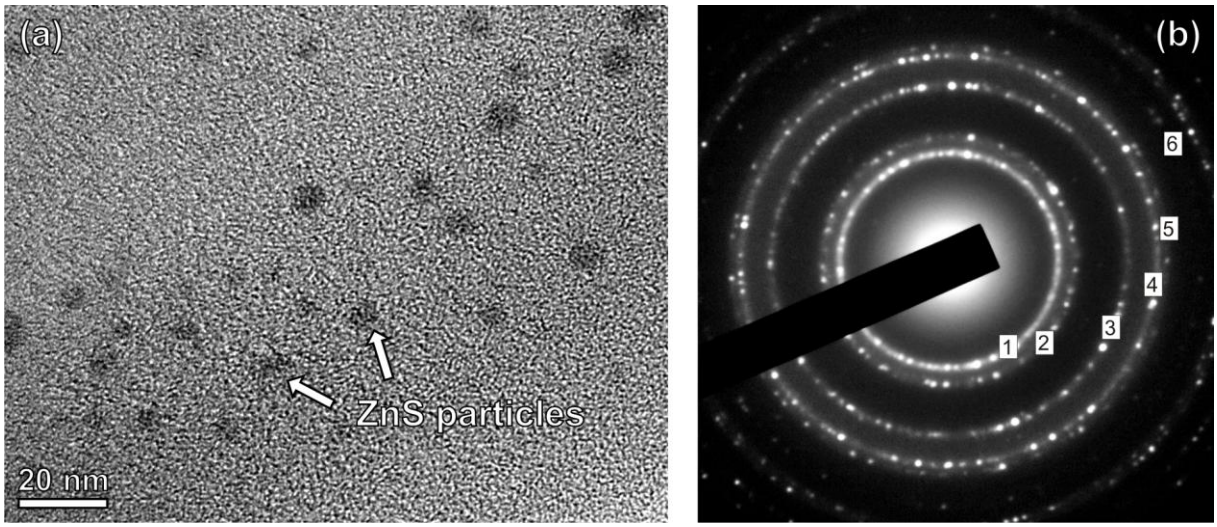

Figure 38. *(a) TEM image of the ZnS nanoparticles after 3 reaction cycles with the (b) corresponding selected area diffraction (SAED) pattern. The numbers on the experimental ring-SAED pattern indicate the {hkl}-planes of β-ZnS listed in Figure 35.*

By cycling the synthesis process the {111} twin boundaries in the ZnS crystals started to form. Figure 39 shows the (111) twin-boundary ZnS crystal grown after three reaction cycles. The formation of twins and stacking faults in the {111} planes is not unusual in sphalerite because of the narrow transition-energy difference between the cubic (*ccp*) and hexagonal (*hcp*) stacking of the close-packed {111} Zn and S atomic planes.[46,114] The origin of the twin-boundary formation is faulted stacking, where instead of the regular *ccp* stacking one of the close-packed layers starts depositing in the *hcp* stacking, while the rest of the subsequent material is again deposited in the *ccp* sequence. The crystallographic relationship between the two domains can be described by a 180° rotation about the [111] axis. The twin boundaries in ZnS are typical growth defects [115-116] and as such, they support the proposed diffusion-precipitation growth mechanism with the increasing number of the reaction cycles.

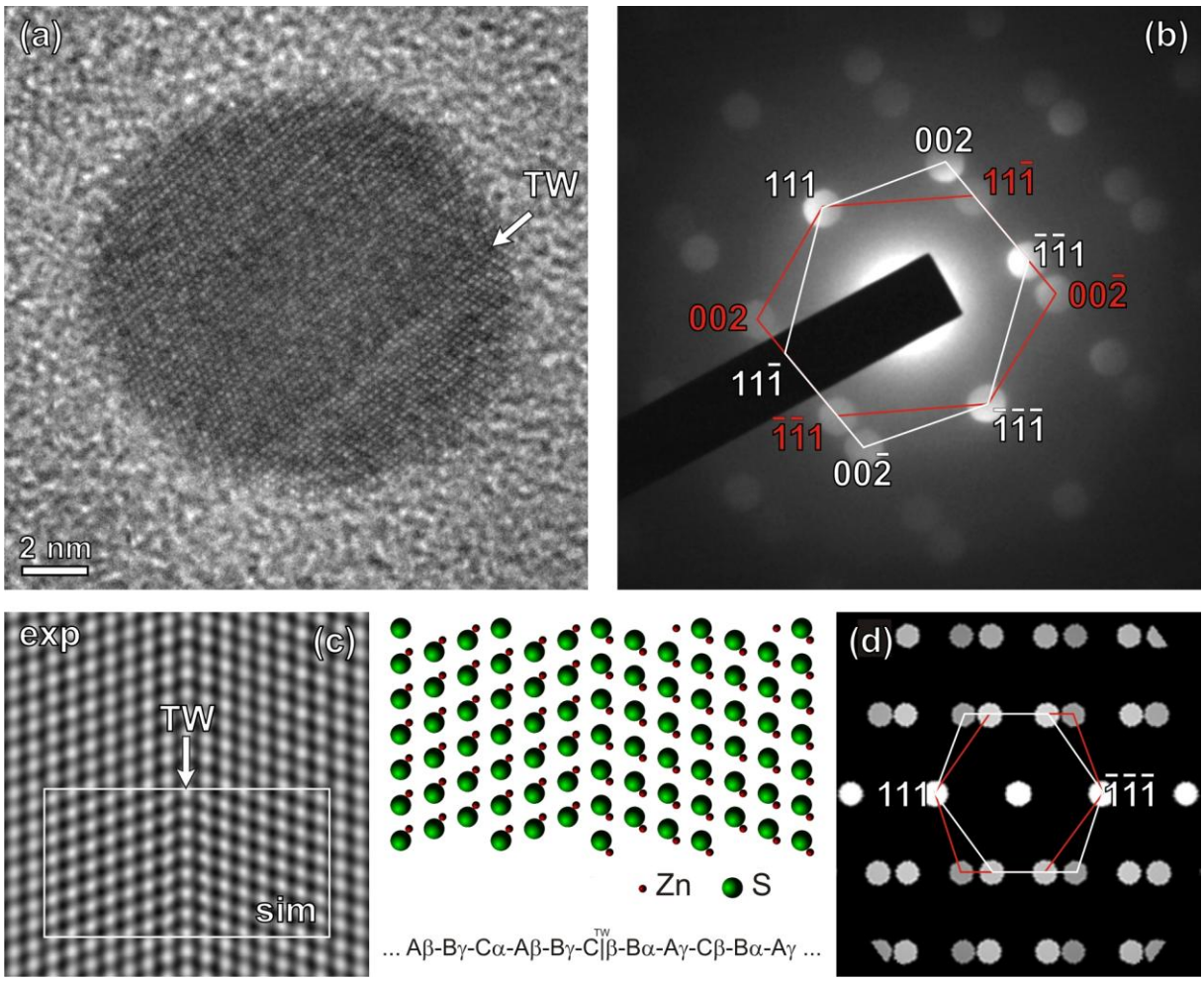

Figure 39. *(a) (111) twin boundary in the spherical sphalerite nanocrystal is a result of faulted local hcp stacking in the otherwise perfect ccp crystal lattice. (b) experimental electron microdiffraction pattern showing that the two sphalerite crystal domains are in the (111) twinning orientation. (c) A close-up of the processed HRTEM image with a simulated inset based on the (111)-twin model for sphalerite (middle). (d) Simulated microdiffraction pattern for a 10-nm thick ZnS crystal.*

However, our observations differ significantly from those made for inorganic nanocrystals synthesized within a strong polyion matrix. For the PbS[106] and FeOOH[89] crystallites synthesised in a strong polyion multilayer of polydiallyldimethylammonium chloride and polystyrenesulfonate (PDDA/PSS) the large aggregation in the initial stage was attributed to the wide distribution of the void spaces within the polymer matrix. Since strong polyions are completely ionized throughout the entire pH range in their multilayer assemblies, charged groups are fully partnered, thereby leaving no available active sites for the metal-ion binding.

This suggests that the incorporation of the metal ions into the network structure is induced by the adsorption of ions within certain domains of the rigid polymer network, leading to the non-spatially selective precipitation of the inorganic species. By repeating the reaction cycle rapid preferential crystal growth along its long axis appeared, which suggests the formation of channel-like cavities within the strong polyion multilayer matrix that physically restrict the growth of the crystallites in other directions. Due to a broad size distribution of the cavities formed within the matrix assembled of strong polyions, the aggregation and growth of the crystallites were more pronounced and consequently, large feathery crystallites with a wide crystal size distribution were formed within the matrix. In contrast to these observations, we have shown that the control over the ion binding sites within the weak polyion template induced by the pH value of the polyelectrolyte assembly yielded a spatially selective precipitation of the inorganic species where control over the morphology, size and volume density of the in-situ precipitated crystallites is possible.

4.3.3 The surface morphology of ZnS/PEMs nanocomposite films

In Figure 40, the evolution of the composite film surface morphology and roughness with the repeatedly cycled in-situ reaction process of ZnS crystallites formation in polyion matrix assembled at pH-value of 2.5 (a, b,c) and 3.0 (d,e,f) is shown, respectively.

The changes in size of the in-situ synthesized ZnS nanocrystals induced by the variation of the polyion multilayer assembly pH-value and particle growth by repeating the reaction cycle are reflected in the morphology of as fabricated ZnS/PEM composite films.

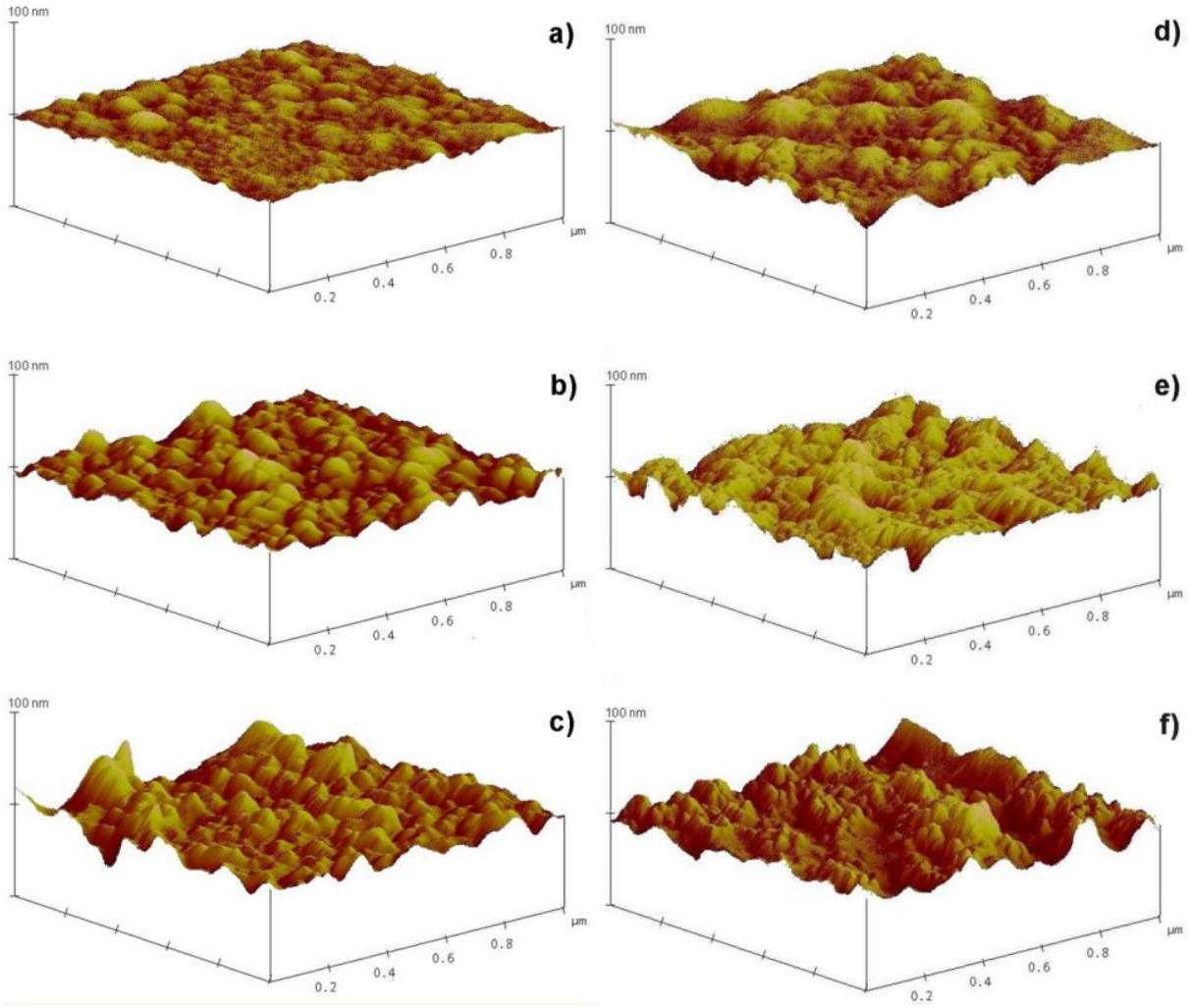

Figure 40. *AFM images of the PEM film assembled a) pH=2.5 and b) pH=3.0 and ZnS/PEM composite films assembled at pH value of 2.5 b) with one reaction cycle c) with three reaction cycles and at pH value of 3.0 e) with one reaction cycle f) with three reaction cycles.*

Prior to the in-situ precipitation of the ZnS nanoparticles, the root-mean-square roughness (RMS) taken over an area of 1µm×1µm was measured to be 1.0 nm for the polyion multilayer assembled at a pH value of 2.5, and 1.9 nm for the assembly pH value of 3.0.

A rather flat surface was obtained for the pristine polyion matrixes (Figure 40 a) and d)), regardless of the pH value of the multilayer assembly, whereas the difference in the morphology and the surface roughness is attributed to the different conformational state of the polyion chains with the variations in the pH value of the multilayer assembly.

As a consequence of the ZnS nanoparticle formation within the PEMs simultaneous morphology changes and an increase in the surface roughness is obtained. The surface roughness of the composite ZnS/polymer film was increased

to 6.5 nm and 8.5 nm after three reaction cycles for the polyion matrix assembled at pH values of 2.5 and 3.0, respectively. As more pronounced aggregation of the primary ZnS nanoparticles yields the formation of larger ZnS crystallites in the polymer matrix, with the increasing assembly pH, higher roughness of the ZnS/PEM composite film is obtained.

4.3.4 Optical properties of ZnS/PEMs nanocomposite films

4.3.4.1 Optical absorption studies

To study the particle size-dependent optical properties, UV-vis absorption measurements of ZnS nanoparticle/PEM composites were performed. From the optical absorption spectra shown in Figure 41 prominent absorption peak at wavelength of 260 nm is obtained for the composite film of ZnS nanoparticles in polyion matrix assembled at the pH value of 2.5.

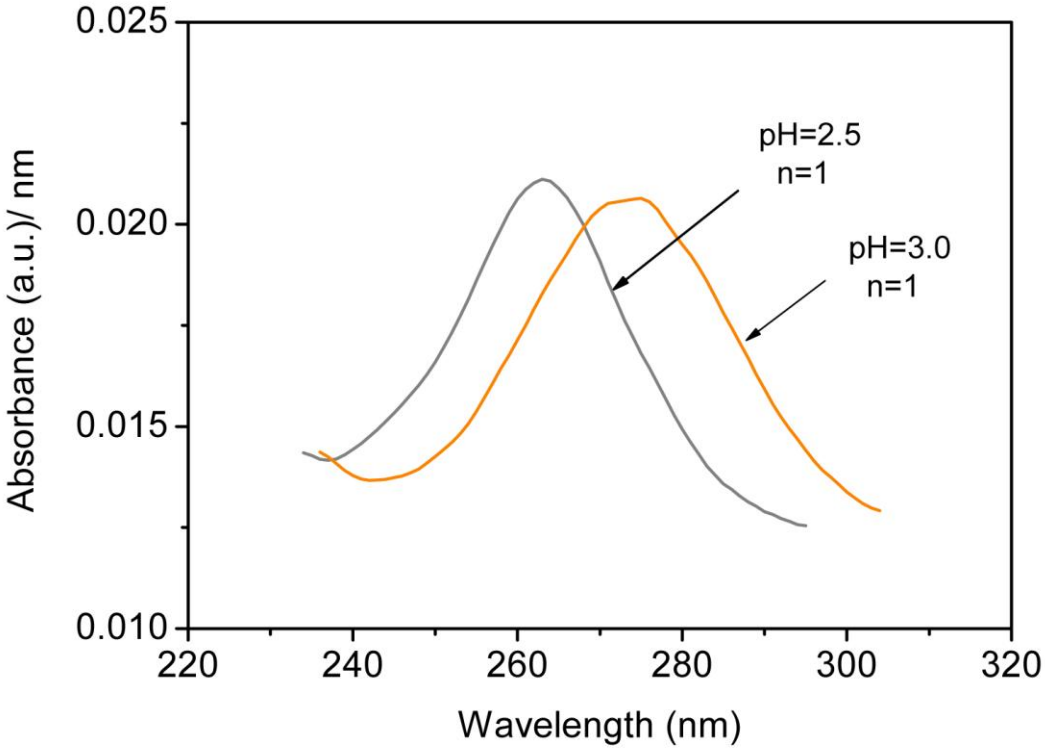

Figure 41. *UV-vis absorption spectra for the ZnS nanoparticle/PEM composite films; the pH value of the polyion matrix assembly is increased from 2.5 to 3.0.*

In Figure 42 the red-shift of the absorption maxima position after three reaction cycles is shown. The red-shift of the absorption maxima peak position as the pH-value of the polyion matrix assembly is increased from 2.5 to 3.0 (Figure 41) as also after three reaction cycles (Figure 42) indicates to the formation of larger ZnS crystallites within the polyion matrix which confirms the observation from the TEM images.

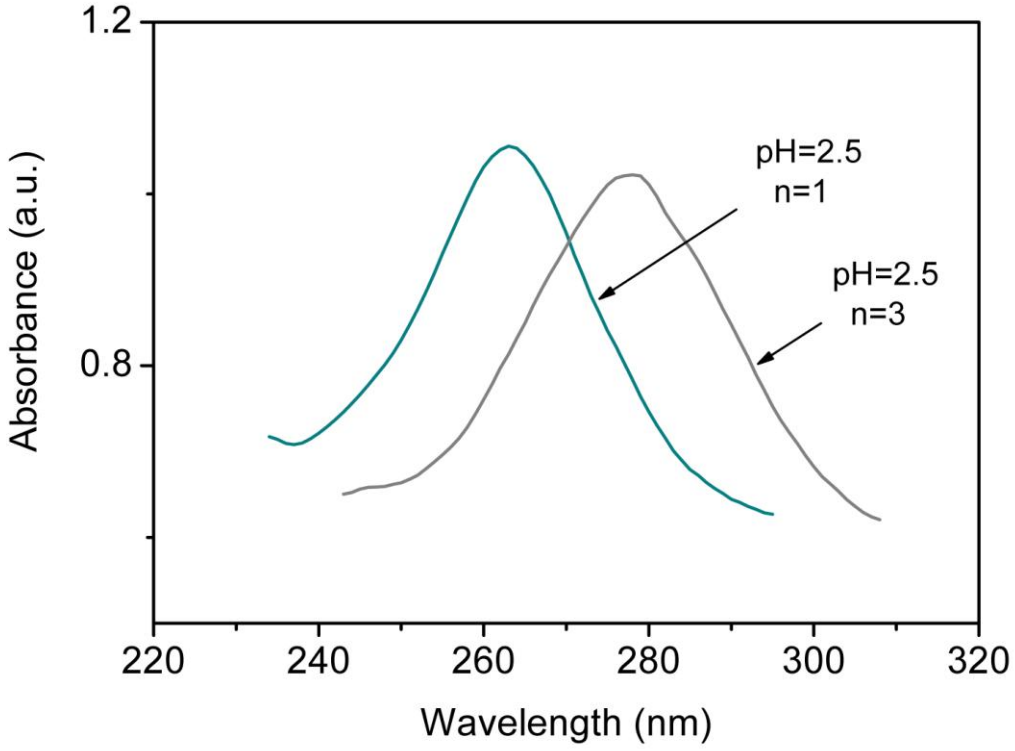

Figure 42. *UV-vis absorption spectra for the ZnS nanoparticle/PEM composite films; the number of the reaction cycles (n) is varied from n=1 to n=3.*

The absorption coefficient (α) is connected to the band-gap energy (E_g) by the relation

$$\alpha = \frac{B(h\upsilon - E_g)^{1/2}}{h\upsilon} \qquad \text{(Eq. 14)}$$

where B is the absorption constant for the allowed direct transition, h is Planck's constant and υ is the photon frequency.[118] By plotting $(\alpha h\nu)^2$ vs. hν and

extrapolating the linear portion of the curve to α=0, the corresponding band-gap energy (E_g) is obtained, as shown in Figure 43.

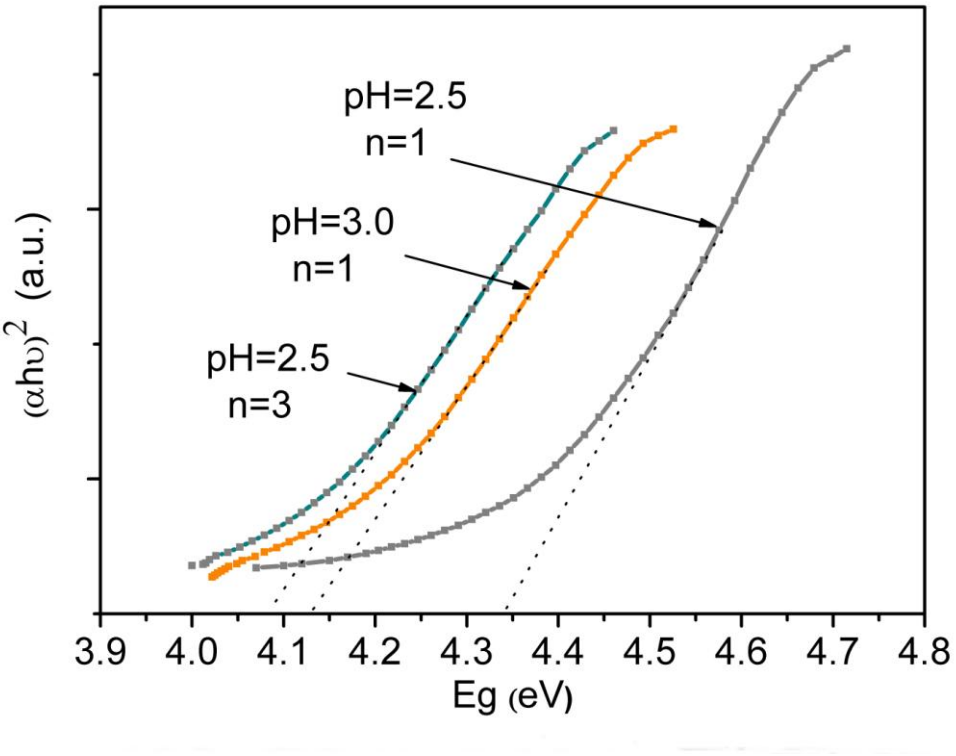

Figure 43. *Plot of $(\alpha h\upsilon)^2$ vs. $h\upsilon$ for the ZnS nanocomposite films; in PEM assembled at pH 2.5 after 3 reaction cycles, in PEM assembled at pH 3.0 with one reaction cycle and in PEM assembled at pH 3.0 with one reaction cycle.*

Based on the effective mass approximation,[119] from the obtained band-gap values the mean particle diameters are estimated according to the equation.

$$\Delta E = E_{g(nano)} - E_{g(bulk)} = \frac{h^2}{8r}\left(\frac{1}{m_e^*} + \frac{1}{m_h^*}\right) - \frac{1.8e^2}{4\pi\varepsilon\varepsilon_0 r} \qquad \text{(Eq.15)}$$

The band-gap values and the corresponding values of the average particle diameters are shown in Table 4.

Table 4: *Band gap energies (Eg) and corresponding average ZnS particle diameter values (nm)*

pH of PEM assembly/number of the reaction cycles (n)	Band gap energy (Eg) [eV]	Calculated mean ZnS particle diameter (nm)
2.5 / n=1	4.33	2.8
2.5 / n=3	4.14	3.3
3.0 / n=1	4.09	3.5

The increase in the band gap energy values with respect to the bulk ZnS (E_g =3.66 eV) are consistent with the observations from the TEM images that the size of the ZnS nanoparticles formed within the polyion matrix is in the nanometer scale, whereas gradual decrease in the band gap energy with the increasing pH-value of the polyion assembly from 2.5 to 3.0 show to the formation of larger ZnS particles in polyion matrix. Furthermore, lower band gap energy of the ZnS crystallites after three reaction cycles reflects the increase in size of the nanoparticles attributed to the dissolution-precipitation growth process. Therefore, by varying the pH-value of the polyion matrix assembly as also by repeating the absorption-precipitation cycle the control over the size and optical properties of the in-situ synthesized ZnS nanoparticles in weak polyion matrix is obtained.

4.3.4.2 Photoluminescence studies

Figure 44 shows the photoluminescence excitation spectra (PLE) of ZnS/PEMs composite films. The PLE peak maximum for the composite films is consistent with the band-edge energy estimated from the absorption spectra.

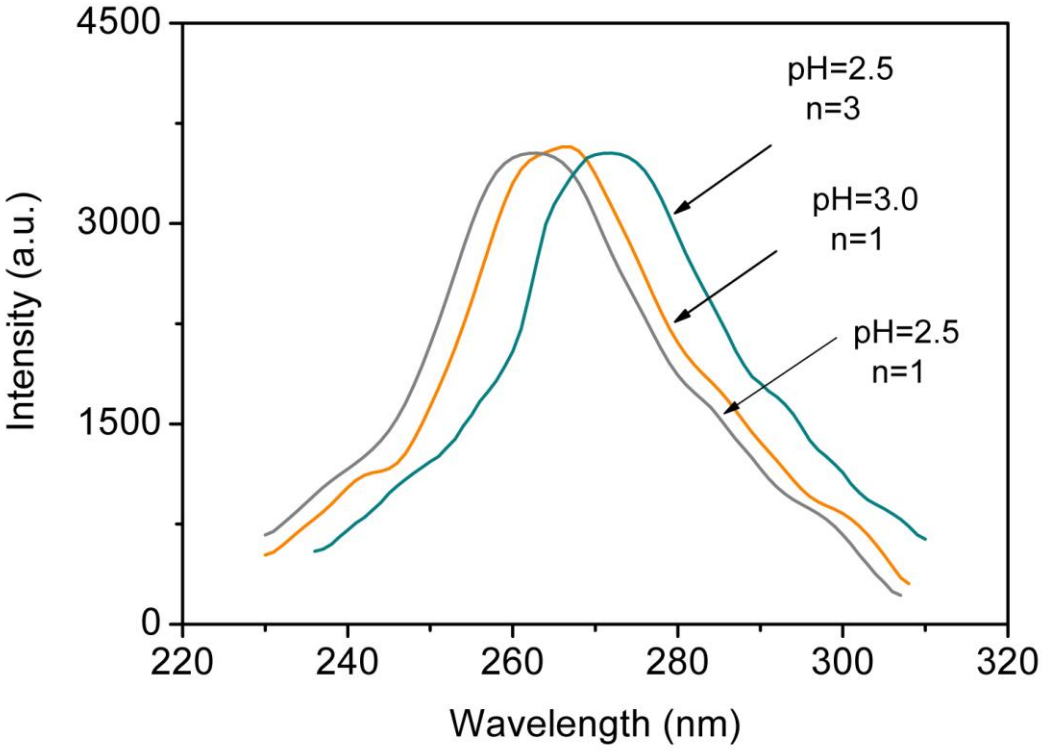

Figure 44. *PLE spectra of the ZnS nanoparticle in polyion matrix of the ZnS nanoparticle in polyion matrix assembled at the pH-value of 2.5 n=1, 3.0 n=1 and 2.5 n=3.*

After excitation, the photoluminescence (PL) spectra of the ZnS nanocomposite films exhibit an intense UV-peak located at wavelength around 300 nm along with the blue emission peak located at 420 nm as shown in Figure 45.

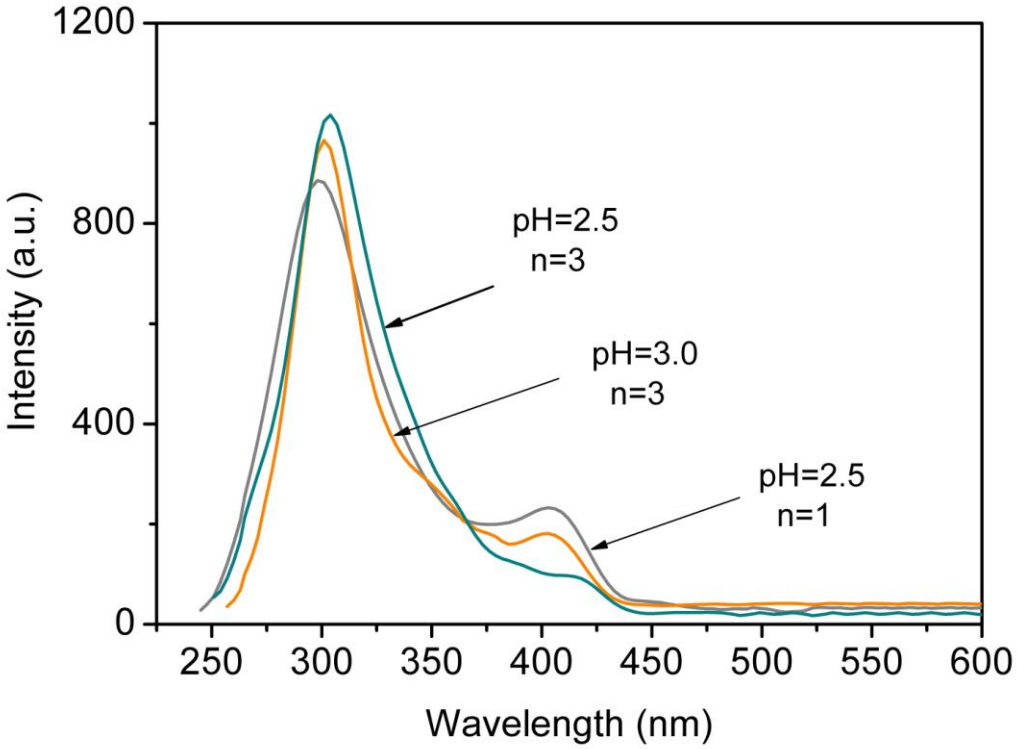

***Figure 45**.PL spectra of the ZnS nanoparticle in polyion matrix of the ZnS nanoparticle in polyion matrix assembled at the pH-value of 2.5 n=1, 3.0 n=1 and 2.5 n=3.*

Regarding the nature of the exciton transitions in the ZnS nanoparticles, the peak located in the UV region is attributed to the excitonic emission while the blue emission is induced by the trapped states due to the presence of localized surface defects of the ZnS nanocrystallites.

Due to the electron-phonon coupling[61] a slight red-shift of the band gap emission compared to the absorption maxima wavelength is observed. From the spectra, it is clear that well defined excitonic emission prevails over the surface state related emission located at 410 nm which may be attributed to the reduction of surface defects of the ZnS nanoparticles as a result of their surface passivation by polyion matrix.

Due to the quantum size effect, the variation in size of the nanoparticles is reflected in the energy value of the band gap. As a result, with the decreasing particle size the blue-shift of the band-edge emission peak wavelength is expected.[120] Therefore, the red-shift of the radiative emission peak with the increase in the pH-value of the polyion assembly and number of the reaction cycles may be attributed to the increase in the size of the ZnS nanocrystallites in polyion matrix.

However, with the decreasing particle size of the ZnS particles in polyion matrix, due to large surface-to-volume ratio the increase in the surface state density promotes the non-radiative recombination, which reflects in the emission at energy lower than the band gap of the material. Consequently, the increase in the blue emission intensity is obtained, whereas the band-to-band emission intensity is reduced as observed from the PL spectra in Figure 45. In solids, there is a tendency for a certain type of defect to arise due to different energy of their formation. For the ZnS nanoparticles the emission wavelength below 430 nm has been reported for the transitions involving interstitial states.[121] Since excess of sulfur ions were present for the ZnS formation within polyion matrix, the emission at 410 nm may be assigned to the transitions arising from the interstitial states of sulfur atoms. Furthermore, the blue-shift of the surface state emission wavelength can be explained by the simultaneous increase in the energy separation of the charge carriers within the band gap caused by reduction in the average size of the nanoparticles.[122]

4.3.4.3 Mn-doping

By doping the ZnS with Mn, the host cations are randomly substituted by Mn-ions yielding in the formation of diluted magnetic semiconductor nanoparticles.[123] In Figure 46, the characteristic emission of Mn-ions in ZnS, located at wavelength of 592 nm,[124] is observed.

On doping, the Mn-ions d-electron states act as efficient luminescence centers while interacting strongly with s-p electronic states of the host ZnS nanocrystal to which excitation is directed.[125] Thereby, an electron that undergoes photo-excitation process in the host ZnS lattice of the nanocrystallites is exposed to the subsequent decay via non-radiative transition to the manganese localized sites yielding a strong orange emission attributed to the radiative transitions between $^4T_1$-$^6A_1$[125] levels which dominate the PL spectrum.

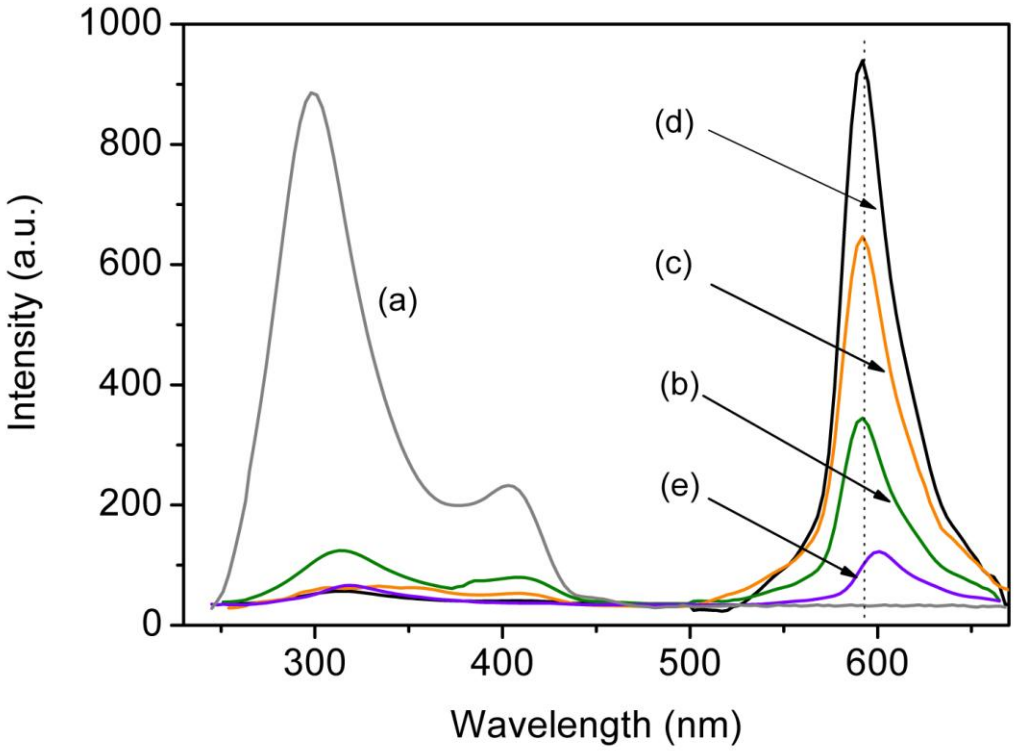

Figure 46. *PL spectra of undoped and Mn-doped ZnS nanoparticles in polyion matrix assembled at the pH-value of a 2.5 n=1 exposed to the increasing concentrations of Mn solution (a)0M, (b) 0.001M, (c) 0.0015M, (d)0.002M and (e)0.003M, excited at 270 nm.*

The increase in the intensity of the $^4T_1$-$^6A_1$ emission with the increasing molar concentration of Mn-ions is observed. Simultaneous increase in the Mn emission intensity and reduction of the UV emission can be explained by the increasing concentration of the Mn-ions incorporated into the host ZnS nanocrystals.

However, by increasing the molar concentration of the Mn-ion solution above 0.002M, the quenching of the luminescence intensity is observed (Figure 46). By exceeding the limit of solubility of Mn^{2+} in ZnS lattice the increase in the concentration of the Mn-ions leads to inhomogeneous distribution of the Mn-ions within the host ZnS nanocrystals yielding formation of local Mn^{2+}- Mn^{2+} pairs that under excitation lead to the non-radiative relaxations.[125] As a result simultaneous red-shift in manganese emission peak position and decrease in luminescence efficiency is observed. Beside the high intensity of the manganese emission the exhibition of an almost defect free Mn-ions transition suggests that high quality manganese doped ZnS nanoparticles were synthesized within the polyion matrix.

4.4 Crystalline TiO_2 film synthesis with the In-situ sol gel reaction in PEM_S

4.4.1 Film thicknesses

The in-situ sol gel reaction of Ti-isopropoxide anhydrous precursor was initiated within the PEM template assembled of 7, 12 and 17 PE bilayers (see experimental). After the infiltration of the precursor in the PEM template a linear increase in the PEM-TiO_2 hybrid film thickness is observed with increasing the number of the adsorbed PE bilayers in PEM as shown in Figure 47.

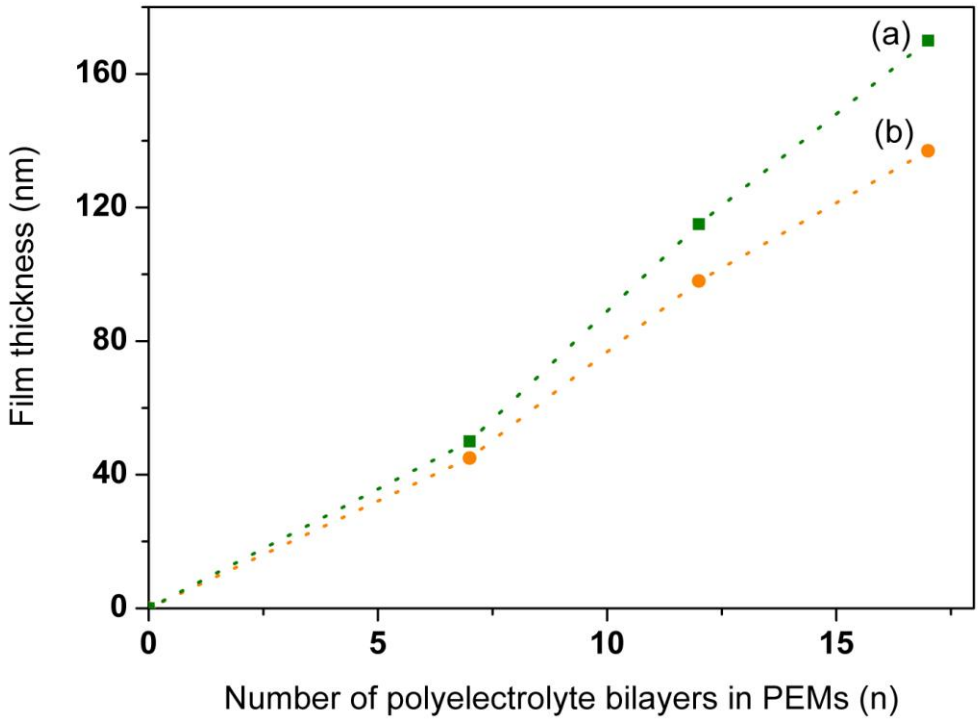

Figure 47. *A plot of (a) the thickness of the TiO_2/organic hybrid film and (b) the thickness of the crystalline TiO_2 film versus the number of PE bilayers in the PEM template.*

The profilometry thickness measurements of the PEM multilayer, TiO_2/PEM hybrid and nano-crystalline TiO_2 films are shown in Table 5.

***Table 5**. Thickness values of PEM multilayer, TiO_2/PEM hybrid and nanocrystalline TiO_2 films.*

Number of PE bilayers in the PEM template	PEM template thickness (nm)	TiO_2/PEM hybrid film thickness (nm)	Crystalline TiO_2 film thickness (nm)	Shrinkage in the film thickness after calcinations (%)
7	50	52	45	13
12	113	115	98	15
17	168	170	140	19

The average incremental thickness of 10 nm per PE layer, calculated from 5 PE bilayers up, in the multilayer template is observed for PEM assembled at pH-value of 3.0.

By exposing the PEM to the titanium iso-propoxide precursor, the precursor infiltrates the PEM template. When compared to the PEM template thickness, there is hardly any difference observed in the thickness of the TiO_2/PEM film, which shows to the uniform dispersion of the precursor within the PEM matrix. Due to incorporated carboxylic groups within the PEM template, the primary interaction expected is the metal-carboxylate formation.[126-127] The metal-oxo carboxylates have the capability of forming covalent bonds between the inorganic and organic phases. Thereby, within the PEM multilayers homogeneous inorganic-organic network is formed, whereas the thickness of the hybrid film is defined by the PEM template thickness. During the annealing process the organic component of the TiO_2 hybrid coating is gradually removed from the inorganic/organic hybrid film, causing the formation of a dense and compact film composed of the TiO_2 crystallites. As a result, the shrinkage in the film thickness is obtained, as shown in Figure 47. The film thicknesses before and after the annealing are displayed in Table 5.

Furthermore, the measured thicknesses of the crystalline TiO_2 films indicate that each PE bilayer contributes an average thickness of between 6 nm and 8 nm to the final thickness of the TiO_2 films. Thus, the in-situ sol-gel process for the formation of the TiO_2 film makes possible control over the TiO_2 film thickness on the nanometer scale by varying the number of PE layers in the organic template.

4.4.2 Surface morphology of the TiO_2 films

In Figure 48 the surface microstructures (a, b, c) of the TiO_2 films fabricated in the PEM templates of 7, 12 and 17 PE bilayers, and a cross-sectional microstructure (d) of the TiO_2 film fabricated within a 17-bilayer PEM template are shown.

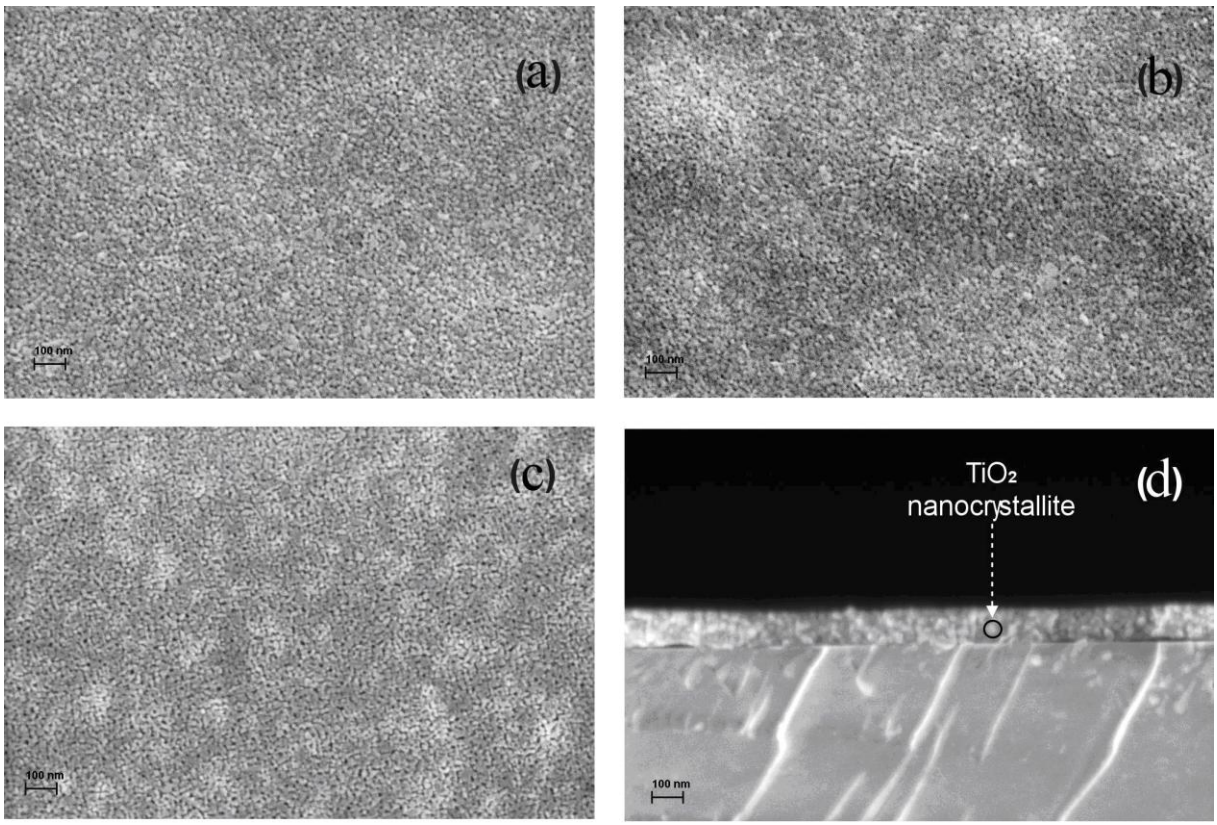

Figure 48. *FE-SEM images of TiO_2 film surfaces fabricated in a PEM template formed of a) 7, b) 12 and c) 17 PE bilayers and d) a cross-section of a TiO_2 film fabricated within a PEM composed of 17 PE bilayers.*

Regardless of the thickness of the PEM template, after annealing, nano-crystalline TiO_2 films with uniform and relatively dense structures were obtained. The films are formed of monodispersed TiO_2 crystallites, whereas the average TiO_2 crystallite size below 15 nm is obtained. Due to the extreme sensitivity of titanium iso-propoxide to water, high reaction rates of hydrolysis and condensation in the sol-gel process normally results in large, polydispersed particles yielding high surface roughness of the TiO_2 film.[128]

Within the PEMs matrix titanium iso-propoxide reacts with organic carboxylic acid forming metal acylates with a release of alcohol, whereas

carboxylate groups may coordinate to the titanium atom in three possible structures.[129] The carboxylate can bind either to one Ti^{IV} center resulting in a bidentate or monodentate mode or it can bind with each of its oxygen atoms to two Ti^{IV} centers yielding the bridging bidendate mode. By this, carboxylate ligands slow down the rates of hydrolysis and condensation reactions of the precursor with water absorbed in PEM yielding TiO_2 cluster formation that are sterically stabilized by the surrounding organic ligands which prevents aggregation and further growth of the TiO_2 particles formed within the PEM template.

Furthermore, by heating up to 350°C, amidization reaction occur between the electrostatically binded carboxylate groups of PAA and the ammonium groups of PAH in the PEM which leads to the formation of nylon-like cross-links within the multilayer film.[130] Thereby, during the annealing process the rigid polymer matrix limits the particle growth and thus enables the formation of uniform, nano-crystalline TiO_2 films.

Figure 49 shows the X-ray diffraction pattern of the TiO_2 films formed in the PEM template and sintered at 500°C for 1hour. According to the X-ray diffraction, the thus-prepared TiO_2 films had a pure anatase crystal structure.

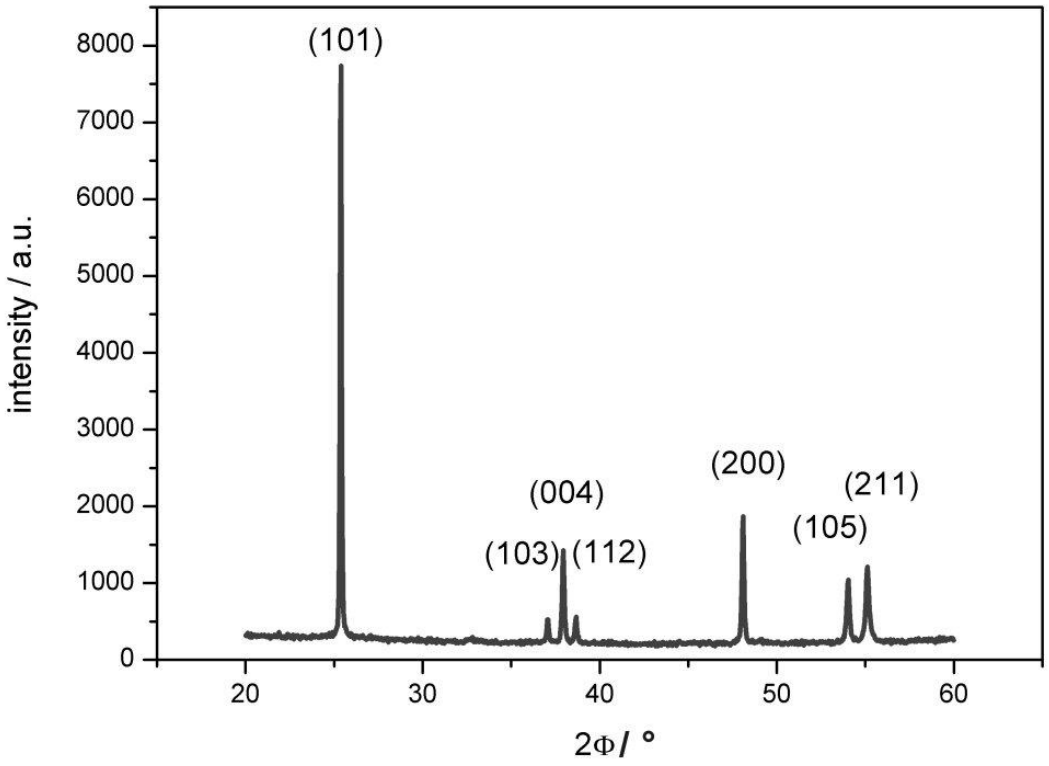

Figure 49. *X-ray diffraction pattern of the TiO_2 films indexed according to the anatase structure.*

4.4.3 Surface roughness of the TiO_2 films

The TiO_2 film roughness evaluated using an atomic force microscope (AFM) is shown in Figure 50. The root mean square (RMS) surface roughness of the TiO_2 films was measured over an area of 10 x 10μm^2. The RMS values of the TiO_2 film fabricated within the templates composed of 7, 12 and 17 PE bilayers were 3.2 nm, 7.3 nm and 9.2 nm, respectively.

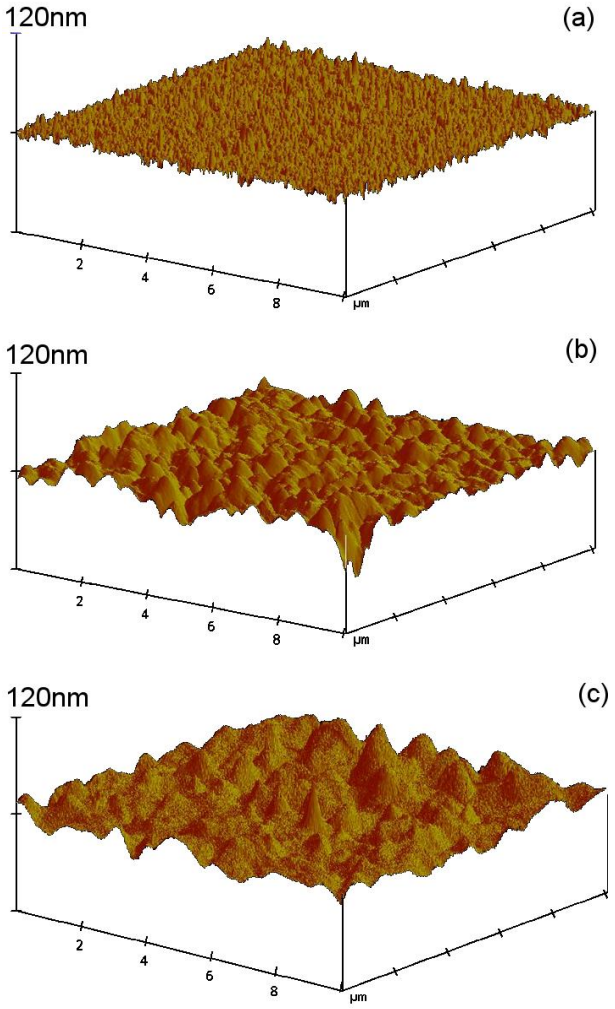

Figure 50. *AFM images of TiO_2 films fabricated in a PEM template formed of a) 7, b) 12 and c) 17 PE bilayers.*

The very low roughness of the films confirms the uniform and homogeneous surface of the TiO_2 films fabricated with the in-situ sol-gel reaction within the PEM template. It is attributed to the formation of fine TiO_2 particles due to controlled sol-gel reaction rates and stabilization of the TiO_2 particles by the surrounding polymer

template. However, an increase in the surface roughness of the TiO_2 film is observed as the number of PE bilayers is increased from 7 to 17. As the thickness of the multilayer template is increased, more of the precursor solution is infiltrated in the PEM which leads to reduce steric stabilization of the TiO_2 clusters by the surrounding polymer chains. Consequently, more extended aggregation of the TiO_2 clusters in the hybrid film results in the increase in particle size.

4.4.4 Optical properties of TiO_2 films

UV-vis spectroscopy was used to characterize the optical properties of the TiO_2 films fabricated within the organic template composed of 7, 12 and 17 PE bilayers. From the absorption spectra in Figure 51, a blue-shift of 40 nm, compared to the λ_{max} of the bulk anatase TiO_2, is observed.

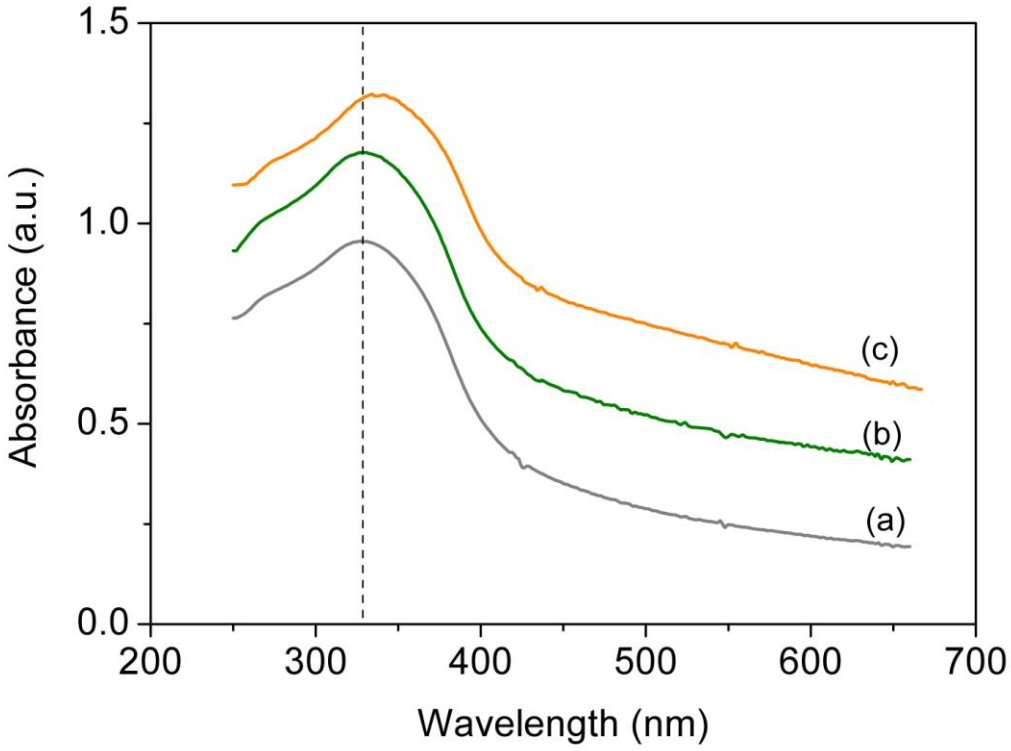

***Figure 51**. UV-vis absorption spectra of TiO_2 films fabricated within (a) 7, (b) 12 and (c) 17 PE bilayered templates.*

TiO_2 is a wide-band-gap oxide semiconductor with an optical band gap of 385 nm (3.2 eV) for the anatase crystal structure. While a blue-shift in the absorption wavelength of 85 nm corresponds to a crystallite diameter of 3 to 5 nm,[131] the blue-shift of 40 nm in the absorption maxima of the TiO_2 films from the absorption

spectra in Figure 51 backs up the observations from the FE-SEM images that the TiO_2 crystallite size is about 10 nm.

By increasing the number of PE bilayers of the template from 7 to 17, the TiO_2 film thicknesses increased from 45 to 130 nm. With the increasing thickness of the film, larger TiO_2 crystallites were observed in the film, and hence the TiO_2 film had a greater roughness, whereas the absorption edge is red shifted. Therefore, as reported previously, an increase in the crystallite diameter, the thickness increment and the higher roughness of the TiO_2 films could be responsible for the red shift of the absorption-maxima peak position as the number of PE bilayers in the organic template is increased from 7 to 17.[132-133]

A general expression in semiconductor physics that relates the absorption coefficient to the energy band gap is $(\alpha h\nu)=A_i\ (h\nu-E_g)^m$, where m is the integer or semi-integer, h is the Planck constant, hν is the energy of the electromagnetic radiation and E_g is the energy of the involved quantum levels in the semiconductor. When m=2 the transitions of the electrons from the valence to the conduction band are indirectly allowed, while when m = ½ a direct band-gap in semiconductors can be considered, where under electromagnetic excitation electron transitions are directly allowed.[134-135] To determine the type of band-to-band transition in the TiO_2 nano-crystallites in the films, the absorption data were fitted to equations of indirect and direct band-gap transitions.

In Figure 52 a plot of $(\alpha h\nu)^{1/2}$ versus $h\nu$ is shown, which is used to calculate the energy band-gap, considering the indirectly allowed transitions of TiO_2 films.

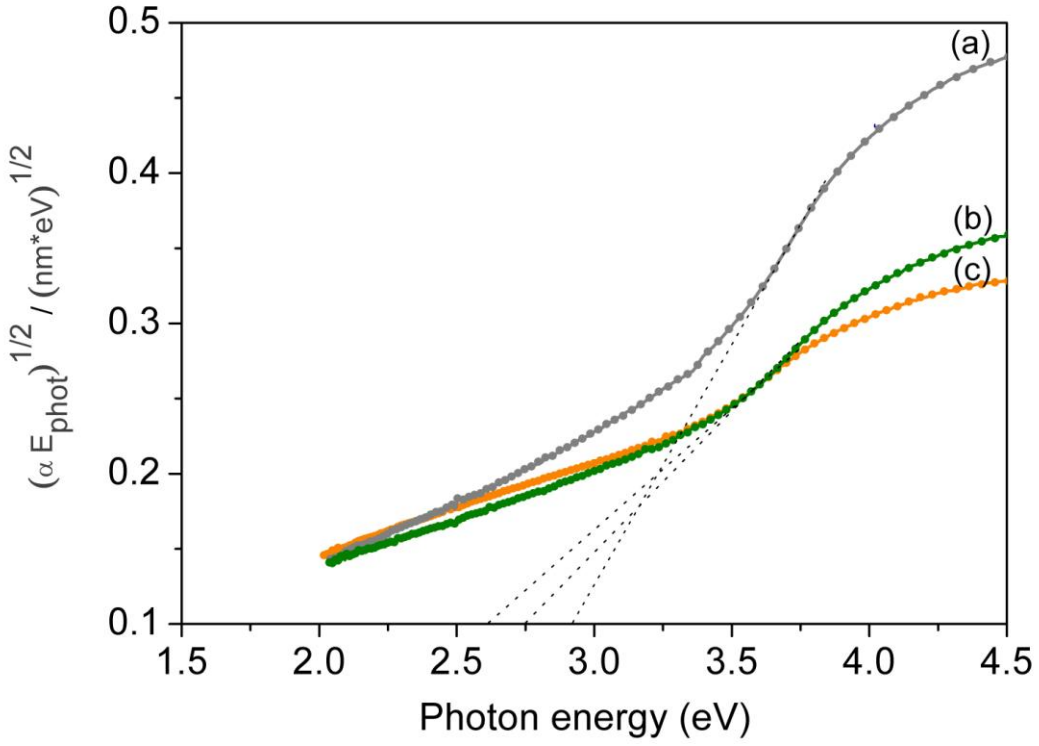

Figure 51. *A plot of a ½ versus E_{phot} for an indirect transition Bandgap energies (E_g) are obtained by extrapolation to a = 0;* TiO_2 *formed within the (a) 7, (b) 12 and (c) 17 bilayered PEM template.*

For a quantitative evaluation of the band-gap energy an extrapolation of the absorption edge to α=0 is required.[136] The calculated values of the band-gap energies for the TiO_2 films formed in templates fabricated from 7, 12 and 17 PE bilayers are 2.95 eV, 2.75 eV and 2.62 eV, respectively. The extrapolated values of the band-gap energies from the plots of the indirect transition are lower than the band-gap energy of the bulk anatase TiO_2, which contradicts the quantum-confinement effect known for TiO_2 crystallite diameters of less than 15 nm, due to which the band-gap energy should be higher than 3.2 eV.[137] Therefore, the data were fitted to the direct-band-gap relation.

In Figure 52 a plot of $(\alpha h\nu)^2$ versus $h\nu$ for the directly allowed transitions is shown.

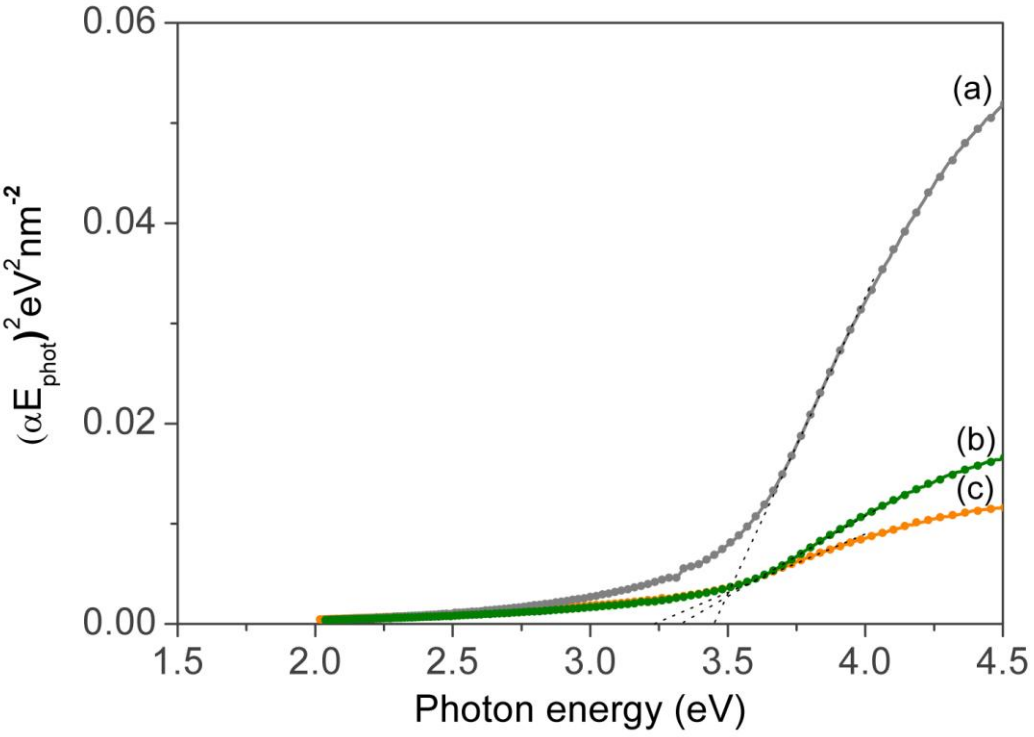

Figure 52. *A plot of $(aE_{phot})^2$ versus E_{phot} for direct transition. Bandgap energies (E_g) are obtained by extrapolation to a = 0.* TiO_2 *formed within the (a) 7, (b) 12 and (c)17 bilayered PEM template.*

The values of the band-gap energies estimated from an α = 0 extrapolation for the samples formed in the 7, 12 and 17 PE bilayered templates are 3.47 eV, 3.3 eV and 3.25 eV, respectively. The obtained values of the energy gap are in good agreement with previous results for direct-band-gap of anatase TiO_2 nanoparticles.[131] The extrapolated values of the band-gap energies in Figure 52 also show a decrease in the band-gap energy for the directly allowed transitions from 3.47eV to 3.25 eV as the TiO_2 film thickness is increased from 45 to 130 nm. Since a similar trend of decreasing the band-gap energy with increasing the PEM template thickness is observed in the case of direct and indirect transitions, due to the quantum-confinement effect the blue-shift of the band-gap energy indicates an increase in the TiO_2 crystallite size with the increasing TiO_2 film thickness.[132] Since the average crystallite diameter about 10 nm in the TiO_2 film formed in the template of 17 PE bilayers is observed, the increase in the band-gap energy with decreasing the film thickness indicates to a decrease in crystallite size below 10 nm as the TiO_2 films

are formed in templates composed of lower number of PE bilayers. Although in bulk TiO_2 only indirect electron transitions are allowed, it is possible that direct electron transitions in crystallites of TiO_2 films are more favorable due to the reduced size and surface effects of the TiO_2 nanocrystallites as the size of the particles approaches the quantum confinement regime. The electronic transitions for direct semiconductors are electrical-dipole assisted, while for indirect semiconductors the electron transition from the valence to the conduction band is phonon assisted, and since they involve a change in momentum their absorption and emission are weaker compared to those of direct-band-gap semiconductors.[138] Therefore, due to favorable direct electron transitions, TiO_2 films fabricated with the in-situ sol-gel reaction within the PEM template exhibit more efficient energy absorption.

In Figure 53 the transmission of visible light TiO_2 films synthesized in the template formed of 7, 12 and 17 PE bilayers is shown.

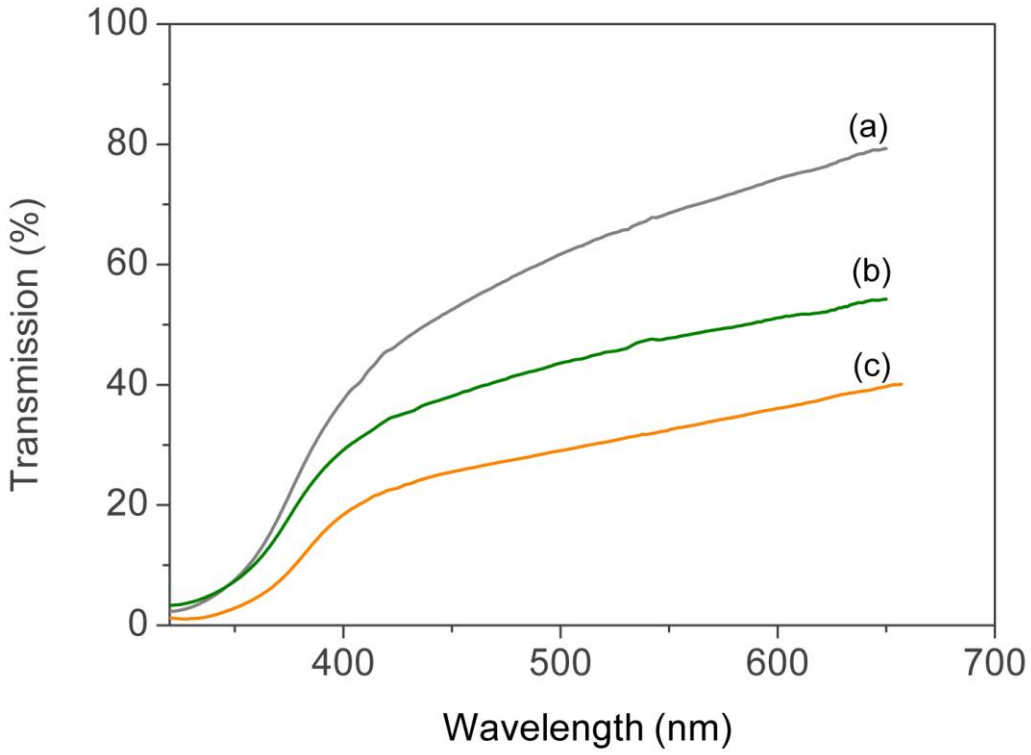

Figure 53. *Transmission spectra of TiO_2 films fabricated within the multilayer template composed of a) 7, b) 12 and c) 17 PE bilayers.*

TiO_2 films fabricated in the template formed of 7, 12 and 17 PE bilayers are highly transparent in the visible region of the electromagnetic spectrum (Figure 53). The highest visible-light transparency of 80% was observed for the TiO_2 film fabricated in the multilayer template composed of 7 PE bilayers; with a larger number of PE bilayers in the organic template, a reduced transmission of crystalline TiO_2 film was obtained.

The increase in the TiO_2 film thickness and surface roughness yield lower transmission of visible light.[137] Since an increase in the template thickness lead to simultaneous increase in the crystalline TiO_2 film thickness and film roughness, these factors could be the reason for reduced transmission of visible light of the TiO_2 films as the number of the PE bilayers in the template is increased from 7 to 17.

5 Conclusions

This thesis has shown that weak polyelectrolyte multilayers present versatile thin film assemblies for the synthesis of various inorganic species. The physical structure and chemical architecture of the weak polyion multilayer films are tunable by means of assembly solution conditions (i.e pH). Moreover, the film thickness is controlled by the number of assembled polyion layers at certain assembly pH value in the nanometer scale.

The weak polyion films formed by the layer-by-layer self assembly technique are chemically rich matrices in which metal ions and complexes from the external solution can access, sample and interact with the multilayer interior. The inorganic nanoparticle precipitation by post binding wet chemical reaction of the ion exchanged metal cations within the multilayer can be applicable for a range of metals and semiconductors synthesis.

Homogeneous inorganic-organic nanostructured composite films were formed by the in-situ synthesis of Ag and ZnS nanoparticles in weak polyion assemblies. We have demonstrated that spatially selective nucleation and growth of spherical ZnS nanocrystals within the weak polyion matrix is obtained by complexation of the metal ions to the carboxylic groups of the weak polyacid chains in the multilayer, followed by a subsequent precipitation by wet chemical reaction. It appears that the conformational state of the multilayer film and the number of carboxylic acid groups incorporated in the PEMs are the key parameters that affect the size and concentration of the Ag nanoparticles in a multilayer film as the pH value of the PEM assembly is varied. The as formed inorganic nanoparticles were homogeneously distributed within the multilayer films, which can be attributed to the uniform distribution of the carboxylic acid groups that result from the high interpenetration of the self-assembled polyelectrolyte chains in the multilayer film.
The pH-controlled supramolecular organization of the weak polyions induces the formation of voids, wherein the aggregative growth mechanism of the primary nanoparticles yields the formation of spherical metallic and semiconducting nanoparticles. The difference in the size and the volume density of the Ag and ZnS nanocrystals in the PEM, induced by the variation in the pH value of the polyion assembly, indicates that the conformational arrangement of the polyion chains and the concentration of the carboxylic groups in the multilayer film are the key parameters influencing the growth mechanism of the inorganic nanocrystals in a

weak polyion matrix. The increase in the size and the volume fraction of the metallic and semiconducting nanocrystallites in the PEM is also obtained by cycling the absorption-precipititation reaction process, where Ostwald ripening might be the dominant growth mechanism. Additionally, by repeating the reaction cycle at a specific pH value the large aggregation of inorganic particles in the PEMs is observed. Furthermore, we have shown that this method can be extended to the synthesis of mixed metallic nanoparticles as the template is exposed to the mixed metal ion solution.

With the ability of the in-situ nanoreactor process to vary the size and the concentration of the inorganic nanoparticles synthesized in a polymer matrix, control over the optical properties of the as fabricated inorganic-organic composite films can be obtained. For the metallic Ag /PEM composite films the intensity and peak position of the SPR in the visible region are controlled by the variations in the size and volume fraction of the Ag nanoparticles in PEMs induced by the assembly pH and number of the reaction cycles. Furthermore, since the surrounding polyion matrix also controls the density of surface states due to the surface passivation of the nanoparticles in the case of semiconducting (ZnS) nanoparticles tunability of the optical absorption and emission properties of the ZnS/PEM nanostructured composite films is obtained. In addition, in-situ synthesized, doped $Zn_{1-x}Mn_xS$ nanoparticles in PEM exhibit a visible fluorescence emission, while the intensity of the emission is controlled by the concentration of Mn ions in the host ZnS.

Nano-crystalline anatase TiO_2 films with controlled thicknesses were fabricated using a modified sol-gel method, within a PEM template fabricated with a layer-by-layer (LbL) self-assembly of appositively charged polyelectrolytes. Since with the in-situ sol-gel process the hydrolysis and condensation reactions take place within the multilayer template, the thickness of the TiO_2 film is determined by the template thickness, which can be controlled on the nanometer scale by varying the number of PE bilayers. Furthermore, by controlling the thickness of the PEM template we were able to control the surface morphology of the TiO_2 films and the size of the TiO_2 crystallites. In compare to other sol-gel thin film fabrication methods, PEM template assisted in-situ sol gel reaction results in very low surface roughness of TiO_2 films. As the number of PE bilayers in the organic template was increased, due to the larger aggregation of the TiO_2 particles an increased surface roughness of the TiO_2 films was observed. We have shown that with the in-situ sol-gel method in a PEM template the control over the TiO_2 particle size, the thickness and the surface morphology of the TiO_2 films also enables tailoring of the optical

properties of the TiO_2 films. Due to the quantum-confinement effect in the TiO_2 particles with nano-dimensions, the blue shift in the absorption maxima is observed for a TiO_2 particle size of about 10 nm. Moreover, the as-fabricated large surface area of the nano-structured TiO_2 films shows strong absorption in the UV region and high transparency in the visible region of the electromagnetic spectra, which could in turn enable their use for optical and photo-catalytic applications.

6 Acknowledgements

First of all I would like to thank my Ph.D supervisor Prof. Dr. Danilo Suvorov for his guidance, support and encouragement during my Ph.D study.

I would especially like to thank my co-supervisor Dr. Boštjan Jančar for the expert guidance, valuable discussions about my work as well as useful remarks and sugestions.

I also thank the members of my thesis committee, Prof. Dr. Paolo Nanni, Assist. Prof. Dr. Miran Čeh and Assist. Prof. Dr. Aleksander Rečnik for their insightful comments and remarks.

Thanks to all my collegues in the Advanced materials department for all the support and nice moments that we had spent together over the last five years.

Finally, I would like to thank my family for their moral support and encouragement.

7 References

1. *Kreibeg, U.; Vollmer,M.; Optical Properties of Metal Clusters (Springer-Verlag, Berlin 1995)*

2. *Link, S.; El-Sayed, M.A. Spectral properties and relaxation dynamics of surface plasmon electronic oscillations in gold and silver nanodots and nanorods. J.Phys.Chem.B* ***103****, 4212 (1999)*

3. *Link, S; El-Sayed, M.A. Shape and size dependence of radiative, nonradiative, and photothermal properties of gold nanocrystals. Int.rev.Phys.Chem.****19****, 409 (2000)*

4. *Bohren, C. F.; Huffman, D. R. Absorption and scattering of light by small particles (John Wiley & Sons, New York 1983)*

5. *Doremus, R.H. Glass science (John Wiley & Sons, New York, 1994)*

6. *Doremus, R.H. Optical properties of small gold particles. J.Chem. Phys.****40****, 2389 (1964)*

7. *Wiley, B. J.; Im, S.H.; Li, Z.-Y.; McLellan, J.; Siekkinen, A.; Xia, Y. Maneuvering the surface plasmon resonance of silver nanostructures through shape-controlled synthesis. J. Phys. Chem. B,* ***110****, 15666 (2006)*

8. *Chen, C.C.; Herhold, A.B.; Johnson, C.S.; Alivisatos, A.P. Structural transformations and metastability in semiconductor nanocrystals. Science,* ***276****,398 (1997)*

9. *Empedocles, S.A.; Bawendi, M.G. Quantum-confined stark effect in single CdSe nanocrystallite quantum dots****.*** *Science,* ***278****, 2114 (1997)*

10. *Nirmal, M.; Brus, L. Luminescence photophysics in semiconductor nanocrystals. ACC: Chem.Res.****32****, 407 (1999)*

11. *Gaponenko, S. Optical properties of semiconductor nanocrystals (Cambridge university press, New York, 1998)*

12. *Bruss, L. Chemical approaches to semiconductor nanocrystals. J. Phys.Chem. Solids,* ***59****, 459 (1998)*

13. *Dabbousi, B. O.;Rodriguez-Viejo, J. ; Mikulec, F. V.;. Heine, J. R ;Mattoussi, H.; Ober, R.; Jensen, K. F.; Bawendi, M. G. (CdSe)ZnS core-shell quantum dots: synthesis and characterization of a size series of highly luminescent nanocrystallites. J. Phys. Chem. B,* ***101****, 9463 (1997)*

14. *Castro, C.L.; Mitchell, B.S. Nanoparticles from mechanical attrition (American Scientific Publishers, Stevenson ranch, 2002)*

15. *Erven, J.; Moerman, R.; Marijinissen, J.C.M. Platinum nanoparticle production by EDHA. Aerosol Science Technology,* ***39****, 941 (2005)*

16. *Mileham, J. R.; Pearton, S. J.; Abernathy, C. R.; MacKenzie, J. D.; Shu, R. J.; Kilcoyne, S. P. Wet chemical etching of AlN. Appl. Phys. Lett.* ***67****, 1119 (1995)*

17. *Singh, R. K.; Narayan, R. Pulsed-laser evaporation technique for deposition of thin films: Physics and theoretical model. Phys. Rev. B* ***41****, 8843 - 8859 (1990)*

18. *Whitesides, G.M.; Mathias, J.P.; Seto, C.T. Molecular self-assembly and nanochemistry: a chemical strategy for the synthesis of nanostructures. Science****, 254****, 1312 (1991)*

19. *Nagarajan, R.; Hatton, T. A. Nanoparticles synthesis, stabillization, passivation and functionalization (Oxford university press, Oxford, 2004)*

20. *Dutta, H.; Rao, T. Introduction to nanoscience (CrC press, Florida, 1998)*

21. *Abraham, F. F. Homogeneous nucleation theory (Academic Press, New York, 1974)*

22. *Ham, F. S. Diffusion-limited growth of precipitate particles. J. Appl. Phys.* ***30****, 1518 (1959)*

23. *Haratuta, M.; Delmon, B. Statistical mechanics of supercoiling-induced B-to-Z transitions in a closed circular DNA: One-dimensional model system with a double quadratic displacement potential and long range interactions. J. Chem. Phys.* ***83****, 859 (1986)*

24. *Nielsen, A.E. Kinetic of precipitation (Macmillan, New York, 1964)*

25. *La Mer, V.K. Nucleation in phase transitions. Ind. Eng. Chem. Res.* ***44****, 1270 (1952)*

26 *Duff, D. G.; Edwards, P.P.; Johnson, B.F.G. Formation of a polymer-protected platinum sol: a new understanding of the parameters controlling morphology. J. Phys. Chem.* ***99****, 15934 (1995)*

27. *Wang, Y. Nonlinear optical properties of nanometer-sized semiconductor clusters. ACC. Chem. RES.* ***24****, 133 (1991)*

28. *Murray, C. B.;Norris, D. J.; Bawendi, M.G.;Synthesis and characterization of nearly monodisperse CdE (E = sulfur, selenium, tellurium) semiconductor nanocrystallites. J. Am. Chem. Soc.* ***115****, 8706 (1993)*

29. *Selvan, S.T.; Bullen, C.; Ashokkuma, M. R.; Mulvaney,P. Photocalcination of mesoporous silica films using vacuum ultraviolet light. Adv. Mater.* ***13****, 985 (2000)*

30. *Reisfeld, R.; Brusilovsky, D.; Eyal, M.; Miron, M.; Burshein, Z.; Ivri, J. A new solid-state tunable laser in the visible. Chem. Phys. Lett.* ***160****, 43 (1989)*

31. *Shea, K.; Loy, D.A.; Webster, O. Arylsilsesquioxane gels and related materials. New hybrids of organic and inorganic networks. J.Am. Chem. Soc.* ***114****, 6700 (1992)*

32. *Petrella, A.; Agostiano, A. Optical properties of hybrid composites based on highly luminescent CdS nanocrystals in polymer. Nanotechnology, 15****,*** *S240 (2004)*

33. *Selvan, S. T.; Spatz, J. P.; Klok, H. A.; Moller, M. Gold-polypyrrole core-shell particles in diblock copolymer micelles****.*** *Adv. Mater.,* ***10,*** *132 (1998)*

34. *Cohen, R. E. Block copolymers as templates for functional materials. Curr.Opin.Solid State Mater. Sci.* ***4,*** *587 (1999)*

35. *Wang, X. S.; Dykstra, T. E.; Salvador, M. R.; Manners, I.; Scholes, G. D.; Winnik, .A. Surface passivation of luminescent colloidal quantum dots with Poly(Dimethylaminoethyl methacrylate) through a ligand exchange process. J. Am.Chem.Soc.,* ***126,*** *7784 (2004)*

36. *Pileni, M. P.; Motte, L.; Petit, C. Synthesis of cadmium sulfide in situ in reverse micelles: influence of the preparation modes on size, polydispersity, and photochemical reactions. Chem. Mater.* ***4****, 338 (1992)*

37. *Watzke, H. J.; Fendler, J. H. Quantum size effects of in situ generated colloidal cadmium sulfide particles in dioctadecyldimethylammonium chloride surfactant vesicles. J. Phys. Chem.,* ***91****, 854 (1987)*

38. *Wang Y.; Herron, N. Optical properties of cadmium sulfide and lead(II) sulfide clusters encapsulated in zeolites. J. Phys. Chem.* ***91****, 257(1987)*

39. *Cummins, C. C.; Schrock, R. R.; Cohen, R. E. Synthesis of silver and gold nanoclusters within microphase-separated diblock copolymers. Chem. Mater.* ***4****, 27(1992)*

40. *Cummins, C. C.; Schrock, R. R.; Cohen, R. E. Synthesis of zinc sulfide and cadmium s ulfide within ROMP block copolymer microdomains. Chem. Mater.,* ***4****, 27 (1992)*

41. *Yue, J.; Sankaran, V.; Cohen, R. E.; Schrock, R. R. Interconversion of ZnF_2 and ZnS nanoclusters within spherical microdomains in block copolymer films. J. Am. Chem. Soc.,* ***115,*** *4409 (1993)*

42. *Sankaran, V.; Yue, J.; Cohen, R. E.; Schrock, R. R.; Silbey, R. J. Synthesis of zinc sulfide clusters and zinc particles within microphase-separated domains of organometallic block copolymers. Chem. Mater.* ***5****, 1133 (1993)*

43. *Sankaran, V.; Cummins, C. C.; Schrock, R. R.; Cohen, R. E.; Silbey, R. J. Small lead sulfide (PbS) clusters prepared via ROMP block copolymer technology. J. Am. Chem. Soc.* ***112****, 6858 (1990)*

44. *Tassoni, R.; Schrock, R. R.; Synthesis of PbS Nanoclusters within Microphase-Separated Diblock Copolymer Films. Chem. Mater.* ***6****,744 (1994)*

45. *Yue, J.; Cohen, R. E.; Nanoreactors for inorganic cluster synthesis. Supramol. Sci.* ***1****, 117 (1994)*

46. *Kane, R. S.; Cohen, R. E.; Silbey, R. J. Synthesis of PbS Nanoclusters within Block Copolymer Nanoreactors. Chem. Mater.* ***8****, 1919 (1996)*

47. *Moffitt, M.; Eisenberg, A. Size control of nanoparticles in semiconductor-polymer composites. 1. Control via multiplet aggregation numbers in styrene-based random ionomers. Chem. Mater.* ***7****, 1178 (1995)*

48. *Spatz, J. P.; Mobmer, S.; Moller, M. Mineralization of Gold Nanoparticles in a Block Copolymer Microemulsion. Chemistry* ***2****, 1552 (1996)*

49. *Cheong, N.; Chan, Y.; Schrock, R. R.; Cohen, R. E., Synthesis of single silver nanoclusters within spherical microdomains in block copolymer films. J. Am. Chem.Soc.* ***114****, 7295 (1992)*

50. *Antonietti, M.; Forster, S.; Hartmann, J.; Oestreich, S. Novel amphiphilic block copolymers by polymer reactions and their use for solubilization of metal salts and metal colloids. Macromolecules* ***29****, 3800 (1996)*

51. *Schneider, T.; Haase, M.; Kornowski, A.; Naused, S.; Weller H.;Forster, S.; Antonietti, M.. Synthesis and characterization of PbS nanoparticles in block copolymer micelles. Phys. Chem.* ***101****, 1654 (1997)*

52. *Lehtinen, K. E. J.; Windeler, R. S.; Friedlander, S. K. Production of nanometer-sized metal oxide particles by gas phase reaction in a free jet. J. Aerosol Sci.* ***26****, S895 (1995)*

53. *Lehtinen, K. E. J.; Windeler R. S.; Friedlander S. K. Prediction of nanoparticle size and the onset of dendrite formation using the method of characteristic times. J. Aerosol Sci.* ***27*** *, 883 (1996)*

54. *Deppe, D. D.; Miller, R. D.; Torkelson, J.M. Small molecule diffusion in a rubbery polymer near Tg: Effects of probe size, shape, and flexibility. J. Polym. Sci., Part B: Polym. Phys.* ***34****, 2987 (1996)*

55. *Hall, D. B.; Miller, R. D.; Torkelson, J. M. Molecular probe techniques for studying diffusion and relaxation in thin and ultrathin polymer films. J. Polym. Sci., Part B: Polym. Phys.* ***35****, 2795 (1997)*

56. *Cao, X.; Bansil, R.; Gantz, D.; Moore, E. W.; Niu, N.; Afdhal, N.H. Diffusion behavior of lipid vesicles in entangled polymer solutions. Biophys. J.* ***73,*** *1932 (1997)*

57. *Shenoy, V.; Rosenblatt, J. Diffusion of Macromolecules in Collagen and Hyaluronic Acid, Rigid-Rod-Flexible Polymer, Composite Matrixes****.*** *Macromolecules* ***28****, 8751 (1995)*

58. *Schneider, T.; Haase, M.; Kornowski, A.; Naused, S.; Weller, H.; Forster, S.; Antonietti, M. Synthesis and characterization of PbS nanoparticles in block copolymer micelles. Phys. Chem.* ***101****, 1654 (1997)*

60. *Shenhar, R.; Norsten, T. B.; Rotello, V. M.; Polymer-mediated nanoparticle assembly: Structural control and applications****.*** *Adv. Mat.****17,*** *657 (2005)*

61. *Kane, R. S.; Cohen, R. E.; Silbey, R. Hydrogen-induced deformations of metals followed by in situ scanning tunneling microscopy: Palladium electrolytic hydrogen charging and discharging in alkaline solution****.*** *Langmuir* ***15,*** *1 (1999)*

62. *Bhargava, R. Properties of Wide Bandgap II-VI Semiconductors (INSPEC, London, 1997)*

63. *Rotello, V. M. Nanoparticles: Building blocks for nanotechnology (USA: Springer Science+Bussiness Media, Inc.,2002)*

64. *Decher, G.; Hong, J. D.; Schmitt, J. Build up of ultrathin multilayer films by a self-assembly process: III. Consecutively alternating adsorption of anionic and cationic polyelectrolytes on charged surfaces. Thin solid films* ***210 / 211,*** *831 (1992)*

65. *Voigt, U. ; Jaeger, W.; Findenegg, G. H. ; Klitzing, R. V. Charge effects on the formation of multilayers containing strong polyelectrolytes. J. Phys. Chem. B* ***107****, 5273 (2003)*

66. *Lvov, Y.; Decher, G.; Mohvald, H. Assembly, structural characterization, and thermal behavior of layer-by-layer deposited ultrathin films of poly(vinyl sulfate) and poly(allylamine). Langmuir* ***9****, 481 (1993)*

67. *Decher, G. Fuzzy Nanoassemblies: Toward Layered Polymeric Multicomposites****.*** *Science* ***277****, 1232 (1997)*

68. *Yoo, D.; Shiratori, S. S.; Rubner, M. F. Controlling bilayer composition and surface wettability of sequentially adsorbed multilayers of weak polyelectrolytes. Macromolecules* ***31,*** *4309 (1998)*

69. *Shiratori, S. S.; Rubner, M. F. pH-dependent thickness behavior of sequentially adsorbed layers of weak polyelectrolytes****.*** *Macromolecules* ***33,*** *4213 (2000)*

70. *Kovtyukhova, N.I.; Olliver, P.J.; Martin, B.R.; Mallouk, T.E.; Chizhik, S.A.; Buzaneva, E.V.; Gorchinsky, A.D. Layer-by-layer assembly of ultrathin composite films from micron-sized graphite oxide sheets and polycations. Chem. Mater.,* ***11****, 771 (1999)*

71. *Javey,A.; Nam,S.W.; Friedman,R.S.; Yan,H. Lieber, C.M. Layer-by-Layer Assembly of Nanowires for Three-Dimensional, Multifunctional Electronics. Nano Lett.* ***7****, 773 (2007)*

72. *Hao, E.; Yang, B.; Ren, H.; Qian, X.; Xie, T.; Shen, J.; Li, D.; Fabrication of composite films comprising TiO_2/CdS and polyelectrolytes based on ionic attraction. Mat. Sci. Eng. C* ***10****, 119 (1999)*

73. *Lvov, Yu.; Ariga, K.; Onda, M.; Ichinose, I.; Kunitake, T.; Alternate assembly of ordered multilayers of SiO_2 and other nanoparticles and polyions. Langmuir* ***13****, 6195 (1997)*

74. *Kovtyukhova, N.; Ollivier, P. J.; Chizhik, S.; Dubravin, A.; Buzaneva, E.; Gorchinskiy A.; Marchenko A.; Smirnova, N. Self-assembly of ultrathin composite TiO_2 /polymer films. Thin Solid Films,* ***337****, 166 (1999)*

75. *Sun, Y.; Hao, E.; Zhang, X.; Yang, B.; Li, F.; Shen, J. Monolayer of TiO_2/PbS coupled semiconductror nanoparticle. J. Chem. Soc., Chem. Commun.* ***10****, 2381 (1996)*

76. *Gao, M.; Zhang, X.; Yang, B.; Li, F.; Shen, J. Assembly of modified CdS particles/cationic polymer based on electrostatic interactions. Thin Solid Films* ***284/285****, 242 (1996)*

77. *Cliffel, D.E.; Zamborini, F.P.; Gross, S.M.; Murray, R.W. Mercaptoammonium-monolayer-protected, water-soluble gold, silver, and palladium clusters. Langmuir* ***16****, 9699 (2000)*

78. *Dutta, A. K.; Ho, T.; Zhang, L.; Stroeve, P.; Nucleation and growth of lead sulfide nano- and microcrystallites in supramolecular polymer assemblies. Chem. Mater.* ***12*** *1042 (2000)*

79. *Dante, S.; Hou, Z.; Risbud, S.; Stroeve, P.; Nucleation of iron oxy-hydroxide nanoparticles by layer-by-layer polyionic assemblies****.*** *Langmuir* ***15,*** *2176 (1999)*

80. *Dutta, A. K.; Jarero, G.; Zhang, L.; Stroeve, P. In-Situ nucleation and growth of γ-FeOOH nanocrystallites in polymeric supramolecular assemblies****.*** *Chem. Mat.* ***12,*** *176 (2000)*

81. *Joly, S.; Kane, R.; Radzilowski, L.; Wang, T. C.; Wu, A.; Cohen, R. E.; Thomas, E. L.; Rubner, M. F. Multilayer nanoreactors for metallic and semiconducting particles****.*** *Langmuir* ***16,*** *1354 (2000)*

82. *Dutta, A. K.; Ho, T.; Zhang, L.; Stroeve, P. Nucleation and growth of lead sulfide nano- and microcrystallites in supramolecular polymer assemblies****.*** *Chem. Mat.* ***12,*** *1042 (2000)*

83. *Zhang, L.; Dutta, A.K.; Jarero, G.; Stroeve, P. Nucleation and growth of cobalt hydroxide crystallites in organized polymeric multilayers****.*** *Langmuir* ***16****, 7095 (2000)*

84. *Wang, T. C.; Rubner, M. F.; Cohen, R. E. Polyelectrolyte multilayer nanoreactors for preparing silver nanoparticle composites: Controlling metal concentration and nanoparticle size****.*** *Langmuir* ***18,*** *3370 (2002)*

85. *Joly, S.; Kane, R.; Radzilowski, L.; Wang, T.; Wu, A.; Cohen, R. E.; Thomas, E. L.; Rubner M. F. Multilayer nanoreactors for metallic and semiconducting Particles. Langmuir* ***16,*** *1354 (2000)*

86. *Khaled, S. M.; Sui, R.; Charpentier, P.A.; Rizkalla, A.S. Synthesis of TiO_2–PMMA nanocomposite: Using methacrylic acid as a coupling agent****.*** *Langmuir,* ***23****, 3988 (2007)*

87. *Wang, D. W.; Caruso, F. Polyelectrolyte-coated colloid spheres as templates for sol–gel reactions****.*** *Chem. Mater.,* ***14****, 1909 (2002)*

88. *Shiratori, S. S.; Rubner, M. F. pH-dependent thickness behavior of sequentially adsorbed layers of weak polyelectrolytes. Macromolecules* ***33,*** *4213 (2000)*

89. *Joly, S.; Kane, R.; Radzilowski, L.; Wang, T.; Wu, A.; Cohen, R. E.; Thomas, E. L.; Rubner, M. F. Multilayer Nanoreactors for Metallic and Semiconducting Particles. Langmuir* ***16,*** *1354 (2000)*

90. *Chinn, R. E. Ceramography: Preparation and analysis of ceramic microstructures (ASM International, Ohio, 2002)*

91. *Kane, R S.; Cohen, R. C. Synthesis of doped ZnS nanoclusters within block copolymer nanoreactors. Chem. Mater.* ***11,*** *90 (1999)*

92. *Yoo, D.; Shiratori, S. S.; Rubner, M. F. Controlling bilayer composition and surface wettability of sequentially adsorbed multilayers of weak polyelectrolytes. Macromolecules 31,* ***4309*** *(1998)*

93. *Lehtinen, K. E. J.; Windeler, R. S.; Friedlander, S. K. Production of nanometer-sized metal oxide particles by gas phase reaction in a free jet. J. Aerosol Sci.* ***26****, S851(1995)*

94. *Schmid G. Clusters and Colloids: From Theory to Applications (VCH: Weinheim, 1994)*

95. *Uyeda, N.; Nishino, M.; Suito, E. Nucleus interaction and fine structures of colloidal gold particles. J. Colloid Interface Sci.* ***42****, 264 (1973)*

96. *Leite, M. S.; Rodrigues, V.; Zanchet, D. Structural effects on Au and Ag colloidal nanoparticles. Prog. Coloid Polym.sci.* ***128****, 131(2004)*

97. *Kreibig, U.; Vollmer, M.; Optical properties of metal clusters (Springer-Verlag, Berlin 1995)*

98. *Lance, K. K.; Coronado, E.; Zhao, L. L.; Schatz, G. C. The optical properties of metal nanoparticles: The influence of size, shape, and dielectric environment. J.Phys.Chem. B* ***107****,668 (2003)*

99. *Beecroft, L. L.; Ober, C. K. Nanocomposite materials for optical applications. Chem. Mater.* ***9,*** *1302 (1997)*

100. *Lim, S. K.; Chung, K.J.; Kim, C. K.; Shin, D. W.; Kim, Y. H.; Yoon, C. S. Surface-plasmon resonance of Ag nanoparticles in polyimide. J. Appl. Phys.* ***98****, 243 (2005)*

101. *Hazra, S.; Gibaud, A.; Sella, C. Tunable absorption of Au–Al_2O_3 nanocermet thin films and its morphology. Appl.Phys.Lett.* ***85,*** *395 (2004)*

102. *Kreibig, U.; Fragstein, C. The limitation of electron mean free path in small silver particles. Z. Phys.* ***224,*** *307 (1969)*

103. *Kawabata A.; Kubo R. Electronic properties of fine metallic particles. II. Plasma resonance absorption. J. Phys. Soc. Jpn.* ***21,*** *1765 (1966)*

104. *Jensen, T. R.; Schatz, G. C.; Van Duyne, R. P. Nanosphere Lithography: Surface plasmon resonance spectrum of a periodic array of silver nanoparticles by ultraviolet−visible extinction spectroscopy and electrodynamic modeling. J. Phys. Chem. B* ***103,*** *2394 (1999)*

105. *Takele, H.; Greve, H.; Pochstein, C.; Zaporojtchenko, V.; Faupel, F. Plasmonic properties of Ag nanoclusters in various polymer matrices. Nanotechnology* ***17,*** *3499 (2006)*

106. *Dutta, A. K.; Ho, T.; Zhang, L.; Stroeve, P. Nucleation and growth of lead sulfide nano- and microcrystallites in supramolecular polymer assemblies. Chem. Mat.* ***12,*** *1042 (2000)*

107. *Vacassy, R.; Scholz, S. M.; Dutta, J.; Plummer, C. J. G.; Houriet, R.; Hofmann, H. Synthesis of controlled spherical zinc sulfide particles by precipitation from homogeneous solutions. J. Am. Cheram.Soc.* ***81,*** *2699 (1988)*

108. *Manzoor K.; Adotyaq V.; Vadera S. R.; Kumar N.; Kutty T. R. N. Spontaneous organisation of ZnS nanoparticles into monocrystalline nanorods with highly enhanced dopant-related emission. J.Phys.Chem.Solids* ***66,*** *1164 (2005)*

109. *Penn R. L.; Banfield J. F. Imperfect oriented attachment: a mechanism for dislocation generation in defect-free nanocrystals. Science* ***281,*** *969 (1998)*

110. *Penn, R. L.; Oskam, G.; Sterathmann, G. J.; Searson, P. C.; Ston,e A. T.; Veblen, D. R.; Epitaxial Assembly in Aged Colloids***.** *J. Phys.Chem. B 105***,** *2177 (2001)*

111. *Penn, R. L.; Stone, A. T.; Veblen, D. R.; Defects and disorder: Probing the surface chemistry of heterogenite (CoOOH) by dissolution using hydroquinone and iminodiacetic acid. J. Phys. Chem. B* ***105,*** *4690 (2001)*

112. *Huang, F.; Hengzhong, Z.; Banfield, J. F. Two-stage crystal-growth kinetics observed during hydrothermal coarsening of nanocrystalline ZnS***.** *Nano Lett.****3,*** *373 (2003)*

113. *Banfield, J. F.; Welch, S. A.; Zhang, H.; Ebert, T. T.; Penn, R. L. Aggregation-based crystal growth and microstructure development in natural iron oxyhydroxide biomineralization products***.** *Science* ***289,*** *751 (2000)*

114. *Gilbert, B.; Zhang, H.; Huang, F.; Finnegan, M. P.; Waychunas, G. A.; Banfield, J. F.;, Special phase transformation and crystal growth pathways observed in nanoparticles. Geochem. Trans.* ***4,*** *20 (2003)*

115. *Engel, G. E.; Needs, R. J. Total energy calculations on zinc sulphide polytypes. Journal of Physics, Condensed Matter* ***2,*** *367 (1990)*

116. *Srot, V.; Recnik, A.; Scheu, C.; Sturm, S.; Mirtic, B. Stacking faults and twin boundaries in sphalerite crystals from the Trepča mines in Kosovo. American Mineralogist* ***88,*** *1809 (2003)*

117. *Borah, J.P.; Barman, J.; Sarma, K .C. Structural and optical properties of ZnS nanoparticles. Chalcogenide Lett.* ***5,*** *201 (2008)*

118. *Dutta, K.; Manna, S.; De, S.K.; Optical and electrical characterizations of ZnS nanoparticles embedded in conducting polymer. Synth. Met.* ***159****, 315 (2009)*

119. *Wang, Y.; Herron, N. Nanometer-sized semiconductor clusters: materials synthesis, quantum size effects, and photophysical properties***.** *J. Phys. Chem.,* ***95,*** *525 (1991)*

120. *Kumbhojkar, N.; Nikesh, V. V.; Kshirsagar, A. Photophysical properties of ZnS nanoclusters. J. App. Phys.,* ***88****, 6260 (2000)*

121. *Denzler, D.; Olschewski, M.; Sattler, K. Luminescence studies of localized gap states in colloidal ZnS nanocrystals. J. App. Phys.* ***84,*** *2841 (1998)*

122. *Bhattacharjee, B.; Ganduli, D.; Chaudhuri, S. Growth Behavior of CdS Nanoparticles Embedded in Polymer and Sol-Gel Silica Matrices: Relationship with Surface-State Related Luminescence. J. of Fluorescence* ***12,*** *369 (2002)*

123. *Brus, L. E. Zero-dimensional "excitons" in semiconductor clusters***.** *J. Quantum Electron.* ***22,*** *1909 (1986)*

124. *Suyver, J.F. Synthesis and photoluminescence of nanocrystalline ZnS:Mn^{2+}. Nanoletters,* ***1,*** *429 (2001)*

125. *Yu, I.; Senna, M. Effects of Mn^{2+} distribution in Cu-modified ZnS on the concentration quenching of electroluminescence brightness***.** *Appl. Phys. Lett.* ***66****, 23 (1995)*

126. *Khaled, S. M.; Sui, R.; Charpentier, P.A.; Rizkalla, A.S. Synthesis of TiO_2–PMMA Nanocomposite: Using Methacrylic Acid as a Coupling Agent. Langmuir* ***23****, 3988 (2007)*

127. *Wold, C. R.; Ni, H.; Soucek, M. D. Model reaction study on the interaction between the inorganic and organic phases in drying oil based ceramer coatings. Chem. Mater.,* ***13****, 3032 (2001)*

128. *Barringer, E. A.; Bowen, H. K. High-purity, monodisperse TiO_2 powders by hydrolysis of titanium tetraethoxide. 1. Synthesis and physical properties. Langmuir,* ***1****, 414 (1985)*

129. *Rotzinger, F. P.; Kessekman-Truttmann, J. M.; Hug, S. J.; Shklover, V. J.; Graetzel, M. Structure and vibrational spectrum of formate and acetate adsorbed from aqueous solution onto the TiO_2 rutile (110) surface. Phys. Chem.B,* ***108****, 5004 (2004)*

130. *Mendelsohn, J. D.; Barrett, C. J.; Chan, V. V; Pal, A. J.; Mayes, A. M.; Rubner, M. F. Fabrication of microporous thin films from polyelectrolyte multilayers***.** *Langmuir* ***16****, 5017 (2000)*

131. *Monticone, S.; Tufeu, R.; Kanaev, A.; Scolan, E.; Sanchez, C. Influence of deposition conditions on the structural characteristics of sublimated CdTe thin films. App. Surf. Sci.,* ***162/163****, 565 (2000)*

117. *Reddy, K. M.; Manorama, S. V.; Reddy, A. R. Bandgap studies on anatase titanium dioxide nanoparticles. Mater. Chem. Phys.,* ***78****, 239 (2002)*

132. *Kim, J.; Fujita, S.; Shiratori, S. Fabrication and characterization of TiO_2 thin film prepared by a layer-by-layer self-assembly method. Thin solid films,* ***499****, 83 (2006)*

133. *Dittrich, T. Porous $Ti0_2$: Electron transport and application to dye sensitized injection solar cells***.** *Phys. Stat. sol. (a),* ***182****, 447 (2000)*

134. *Gonzalez, A. E. J.; Santiago, S. G. Structural and optoelectronic characterization of TiO_2 films prepared using the sol–gel technique***.** *Semicond. Sci. technology,* ***22****, 709 (2007)*

121. *Bernardi, M. I. B.; Lee, E. J. H.; Lisboa-Filho, P. N.; Leite, E. R.; Longo, E.; Varela, J. A. TiO_2 Thin Film Growth Using the MOCVD Method. Mat. Res.,* ***4****, 223 (2001)*

135. *Madelung, O.; Taylor, B.C. Introduction to Solid State theory (Springer-Verlag, Berlin, 1978)*

136. *Smith, R. A. Semiconductors (Cambridge University press, Cambridge, 1978)*

137. *Ge, L.; Xu, M.; Sun, M.; Fang, H. Influence of calcination ambient and film thickness on the optical and structural properties of sol-gel TiO_2 thin films. Mat. Res. Bull.* ***41****, 1596 (2006)*

138. *Khanna, P. K.; Singh, N.; Charan, S. Synthesis of nano-particles of anatase-TiO_2 and preparation of its optically transparent film in PVA***.** *Materials letters,* ***61****, 4725 (2007)*

Index of Figures

Index of Tables

Index of Algorithms

Appendix

Publications

Original scientific articles

1. *LOGAR, Manca, JANČAR, Boštjan, SUVOROV, Danilo, KOSTANJŠEK, Rok. In situ synthesis of Ag nanoparticles in polyelectrolyte multilayers. Nanotechnology (Bristol), 2007, vol. 18, pp 325601-1-32506-7.*
2. *VALANT, Matjaž, PODOBNIK, Boštjan, KOVAČIČ, Drago, LOGAR, Manca. Direct-laser writing of striplines on AgCl single crystals. Mater. chem. phys.. [Print ed.], 2008, vol. 110, no. 2/3, pp 280-284.*
3. *LOGAR, Manca, JANČAR, Boštjan, REČNIK, Aleksander, SUVOROV, Danilo. Controlled synthesis of pure and doped ZnS nanoparticles in weak polyion assemblies : growth characteristics and fluorescence properties. Nanotechnology (Bristol), 2009, vol. 20, no. 27, pp 275601.*

Published scientific conference contribution abstracts

4. *VALANT, Matjaž, PODOBNIK, Branko, KOVAČIČ, Drago, LOGAR, Manca. Direct laser writing of LTCC microstrip lines. [X] Electroceramics, Toled06, Toledo, Spain 18-22 June, 2006. Book of abstracts. ECERS, 2006, pp 294.*
5. *LOGAR, Manca, SUVOROV, Danilo. Self-assembled polyelectrolyte multilayers as nanostructured templates for inorganic synthesis. JENKO, Monika (ed.). 14th Conference on Materials and Technology, 16-18 October, 2006, Portorož, Slovenia. Programme and book of abstracts. Ljubljana: Inštitut za kovinske materiale in tehnologije, 2006, pp 66.*
6. *LOGAR, Manca, JANČAR, Boštjan, SUVOROV, Danilo. In-situ synthesis of Ag nanoparticles in self-assemled polyelectrolyte multilayers (PEMs). Nano & hybrid coatings 'Developing of the minute' : Bedford, Brussels, 7-8 March, 2007 : final programme, list of participants, speakers' biographies, 2007.*
7. *LOGAR, Manca, JANČAR, Boštjan, SUVOROV, Danilo. Synthesis of metallic Ag and semiconducting ZnS nanoparticles in self-assembled polyelectrolyte templates. Nanochina 2007 : 4-8 June 2007, Beijing, China.*

8. *LOGAR, Manca, JANČAR, Boštjan, SUVOROV, Danilo. In-situ inorganic nanoparticle formation in self-assemled polyelectrolyte multilayer films. USKOKOVIĆ, Dragan (ur.). Ninth Annual Conference of the Yugoslav Materials Research Society YUCOMAT 2007, Herceg Novi, September 10-14, 2007. Programme and the book of abstracts. Belgrade: Institute of Technical Sciences of SASA, 2007.*
9. *LOGAR, Manca, JANČAR, Boštjan, SUVOROV, Danilo. Synthesis and optical properties of ZnS nanoparticles in polyelecterolyte multilayer (PEM) hybrid films. NANO - 2008, 9th International Conference on Nanostructured Materials, 01-06 June 2008, Rio de Janeiro, Brazil. Abstracts., 2008, pp 137.*
10. *LOGAR, Manca, JANČAR, Boštjan, SUVOROV, Danilo. Karakterizacija nano-kompozitnih (Ag, ZnS/polimer) in keramičnih (TiO_2) tankih plasti pripravljenih z in-situ sintezo anorganske komponente v večplastni polielektrolitni matrici. V: ISKRA, Jernej (ed), MILOŠEV, Ingrid (ed.). Dan mladih raziskovalcev 2009. Ljubljana: Institut "Jožef Stefan", 2009, pp 1.*